UNIVERSITÀ DEGLI STUDI DELL'AQUILA
DIPARTIMENTO DI SCIENZE FISICHE E CHIMICHE

Dottorato di Ricerca in Scienze Fisiche e Chimiche
XXIX CICLO

PULSE SHAPE ANALYSIS OF CUORE-0 BOLOMETERS FOR A BETTER COMPREHENSION OF DETECTOR RESPONSE

Ph.D Candidate:
Daria Santone

School Coordinator:
Prof. Antonio Mecozzi

Advisor:
Dr. Carlo Bucci

Tutor:
Prof. Luigi Pilo

Academic year 2015-2016

Contents

Introduction

In the last years many very important results have been obtained in the study of the neutrino and its properties. Oscillation experiments provided a clearer picture of the neutrino mixing matrix, while cosmological studies set the most stringent limit on the sum of masses of the three neutrino species. Nevertheless some questions about neutrino are still unsolved, as for example the determination of neutrino absolute mass scale and its Dirac or Majorana nature. The neutrino is the only particle that could be described by a Majorana field, namely the neutrino could be its own antiparticle. In Chapter 1 an overview of neutrino properties, including the results obtained in the neutrino oscillations and cosmological studies, is reported.

A unique tool to determine the neutrino nature is the search for neutrinoless double beta decay ($0\nu\beta\beta$). This decay is a second order process, in which a nucleus changes its atomic number by two units without neutrino emission. This is possible if the neutrino has a non-zero mass and it is a Majorana particle. The $0\nu\beta\beta$ decay has never been observed, but its detection could prove that the lepton number is not conserved and could give information on the scale of neutrino mass.

A sensitive $0\nu\beta\beta$ experiment should be characterized by good energy resolution, low level of background, and high isotopic abundance of $\beta\beta$ candidate. The most promising isotope candidates are the ^{76}Ge, ^{130}Te and the ^{136}Xe. The best limit on the $0\nu\beta\beta$ half-life, obtained by the Kamland-Zen experiment on ^{136}Xe, is $T^{1/2} < 1.07 \times 10^{25}$ yr. In Chapter 2 $0\nu\beta\beta$ decay and possible strategies to detect it are described. The best limits on $0\nu\beta\beta$ half-life obtained are also reported.

CUORE is an upcoming 1-tonne $0\nu\beta\beta$ experiment. It searches the $0\nu\beta\beta$ decay on ^{130}Te using bolometric detectors. A bolometer is a low temperature detector in which the energy released into the crystal is converted in thermal phonons.

CUORE is an array of 988 TeO_2 crystals with a total mass of 750 kg, operating at a temperature of 10 mK at Laboratori Nazionali del Gran Sasso. The expected energy resolution of 5 keV and a background level of 10^{-2} $counts/(keV \cdot kg \cdot yr)$ will allow to reach a sensitivity of 9.5×10^{25} yr.

CUORE-0, the CUORE predecessor, was operated between 2013-2015 as CUORE prototype. The energy resolution of CUORE-0 bolometers was

measured to be 4.9 keV. It also tested the validity of the low background material cleaning and assembly procedures designed to reduce the degraded α background in the $0\nu\beta\beta$ decay region of interest. In Chapter 3 an overview of the CUORE experiment and of the CUORE-0 results is given.
The goal of this Ph.D.-thesis was the study of CUORE-0 detector response for a better comprehension of the CUORE bolometers in order to improve the experimental sensitivity. Despite the simple model that describes an ideal bolometer, the actual response is much more complex.
According to the Laplace analysis, the bolometer response is described by a sum of exponentials (at least one rise and one decay constant). Each time constant is related to the presence of an independent heat capacity C_i inside the detector and the corresponding discharge conductance G_i. A predictive thermal model, which includes the relevant contributions to the heat capacity and to the thermal conductances, should characterize the bolometer response and behavior. So far several many different thermal models have been developed. Unfortunately none of them completely describes the detector behavior and the range of different responses among the different bolometers. Moreover, the large number of free or unknown parameters of these models made very difficult putting constrains on them. In Chapters 4 and 5 a description of bolometric detectors working principle and of the CUORE bolometers is given.
In this Ph.D. work I developed a thermal model for the CUORE detectors using a reverse approach: identify different parameters that describe the CUORE bolometer response in order to define the effective heat capacities and thermal conductances. The first part of my analysis was devoted to defined a set of variables that properly describe the pulse shape. In chapter 6 the definition and the optimization of fit function model is described.
With this function, possible correlations between pulse shape parameters and physical parameters have been studied, identifying the most relevant contributions. This study provided, for the first time, the identification of the dominant thermal capacities of a CUORE bolometer. It was possible to isolate two main contributions: the expected heat capacity of the TeO_2 crystal, which is rather similar for all the crystal, and a second capacity related to the presence of platinum inclusions in the TeO_2 crystals. This second heat capacity, due to metallic small pieces of platinum, can assume values competing with the TeO_2, depending of the abundance. In Chapter 7 all the studies and tests on these parameters are reported.
These work opens the way to a full understanding of the CUORE bolometers and to a development of a real thermal model that properly represents the detector behavior. Future studies will allow to act on the relevant parameters to improve the TeO_2 bolometers performances.

Chapter 1

Neutrino Physics

1.1 Neutrinos

In 1930 Pauli introduced a new particle to resolve the statistic problem of the beta spectrum: *"I have come upon a desperate way out regarding the wrong statistic of the ^{14}N and ^{6}Li nuclei, as well as the continuous β spectrum, in order to save the alteration law statistic and the energy law. To wit, the possibility that there could exist in the nucleus electrically neutral particles, which I shall call neutrons...The continuous β spectrum would than become understandable from the assumption that in β decay a neutron is emitted with the electron..."* [1].
The Pauli's particle was renamed *neutrino* by Fermi after the discovery of what is currently called neutron [1]. In 1934 Fermi developed his weak theory to explain the *beta radioactivity*, in which neutrino is involved [2].
The first evidence of neutrino occurred in the inverse β decay in the Savanna River Nuclear Reactor by Reines and Cowan in 1956 [3], 25 years after the Pauli's hypothesis. In 1958 Goldhaber, Grodszin and Sybyran measured the neutrino helicity [4]: it is +1 for the neutrino and -1 for the antineutrino.
The neutrino exists in three different flavors: ν_e,ν_μ,ν_τ. The number of neutrino family, N_ν, was measured in the LEP experiment during the study of Z^0 resonance: $N_\nu = 2.9840 \pm 0.0082$ [5]. The neutrino ν_μ was discovered by Lederman, Steinberger, Shawarts in 1962 [6], while the neutrino ν_τ was discovered in the DONUT experiment in 2001 [7].
At the end of '60 an unexpected deficit in solar neutrino flux was observed by the Homestake experiment [8]. The measured solar neutrino rate was about 1/3 of that predicted by Standard Solar Model. This is the first evidence of *neutrino oscillation*, that significantly changed the Standard Model of particle physics: the neutrino is not a massless particle.
The experiments studying neutrino oscillations gave a clear picture about this phenomena, but they opened several questions about the neutrino mass:

[1] Adapted summary of an English translation to Pauli's letter dated December 4, 1930.

why is the neutrino mass so small?, is the neutrino a Dirac or a Majorana particle?,is the neutrino mass hierarchy direct or inverse?.

1.2 Neutrino mass in the Standard Model

The Standard Model of particle physics describes the strong, electromagnetic and weak interaction of particles in the framework of a quantum field theory. This theory is based on the local symmetry gauge group $\mathrm{SU(3)}_C \bigotimes \mathrm{SU(2)}_L \bigotimes \mathrm{U(1)}_Y$, where C denotes color, L left-handed chirality, Y the weak hypercharge [9].
The fermions are distinguished between quarks, that interact in all interaction, and leptons, that interact in electroweak interaction only.
Quarks and leptons exist in three families. The quark families are describe by three doublets:

$$\begin{pmatrix} u \\ d \end{pmatrix}, \begin{pmatrix} c \\ s \end{pmatrix}, \begin{pmatrix} b \\ t \end{pmatrix}.$$

Instead each neutrino flavor is related to a charged lepton by a doublet:

$$\begin{pmatrix} e \\ \nu_e \end{pmatrix}, \begin{pmatrix} \mu \\ \nu_\mu \end{pmatrix}, \begin{pmatrix} \tau \\ \nu_\tau \end{pmatrix}.$$

The fermion fields are described by *left-handed isospin doublets* (LH) and *right-handed singlets* (RH):

$$Q_{fL} = \begin{pmatrix} u_{fL} \\ d_{fL} \end{pmatrix}, \; u_{fR}, d_{fR}$$

$$L_{fL} = \begin{pmatrix} l_{fL} \\ \nu_{fL} \end{pmatrix}, l_{fR}.$$

The helicity measurement proves that the neutrino which takes part to the SM process is purely *left-handed*.
The quark and lepton masses are generated through a spontaneous symmetry breaking, called *"Higgs Mechanism"*. The fermion fields interact with the Higgs doublet:

$$\phi_H = \begin{pmatrix} \phi^+(x) \\ \phi^0(x) \end{pmatrix},$$

where $\phi^+(x)$ is the charged scalar field and $\phi^0(x)$ is the neutral scalar field. The fermion masses arise through the presence of Yukawa coupling between the fermion field and the Higgs doublet. This interaction is described by the Dirac mass term:

$$\frac{m_\alpha}{v}(\bar{f_L} f_R + f_L \bar{f_R}) H.$$

Since the mass term involves the coupling between the *left-handed* and *right-handed* components, in the Standard Model the neutrino is a massless particle and the neutrino flavors are mass eigenstates.

1.3 Neutrino beyond the SM

The *neutrino oscillation phenomena* were predicted by Pontecorvo in the 1959 and show that the flavors eigenstates are not mass eigenstates [10]. The flavors eigenstates ν_f ($f = e, \nu, \tau$) are related to mass eigenstates ν_k (k = 1,2,3) by the Pontecorvo-Maki-Nakagawa-Sakata (PMNS) neutrino matrix mixing [11]:

$$|\nu_\alpha\rangle = \sum_{i=1}^{3} U^*_{\alpha i}|\nu_i\rangle. \tag{1.1}$$

The PMNS matrix is represented by:

$$U = \begin{pmatrix} 1 & 0 & 0 \\ 0 & c_{23} & s_{23} \\ 0 & -s_{23} & s_{23} \end{pmatrix} \times \begin{pmatrix} c_{13} & 0 & s_{13}e^{-i\delta} \\ 0 & 1 & 0 \\ -s_{13}e^{-i\delta} & 0 & c_{13} \end{pmatrix} \times \begin{pmatrix} c_{12} & s_{12} & 0 \\ -s_{12} & c_{12} & 0 \\ 0 & 0 & 1 \end{pmatrix} \times \begin{pmatrix} e^{i\frac{\alpha_1}{2}} & 0 & 0 \\ 0 & e^{i\frac{\alpha_2}{2}} & 0 \\ 0 & 0 & 1 \end{pmatrix},$$

where $c_{ij} = cos\vartheta_{ij}$, $s_{ij} = sin\vartheta_{ij}$, δ is the Dirac phase, α_1 and α_2 are Majorana phases. While the first three matrices are always used (both for Dirac and Majorana neutrinos), the matrix with the Majorana phases is only present for Majorana neutrino.
The oscillation probability is given by:

$$P(\nu_\alpha \to \nu_\beta) = \sum U^*_{\alpha k} U_{\beta k} U_{\alpha j} U^*_{\beta j} exp(\frac{-i\Delta m^2_{kj} L}{2E}), \tag{1.2}$$

where $\Delta m^2 = m^2_i - m^2_j$ is the squared mass eigenstates difference, L is the traveled distance and E is neutrino energy.
While the three mixing angles $\theta_{12}, \theta_{13}, \theta_{23}$ are independent, the three squared mass differences ($\Delta m^2_{12}, \Delta m^2_{23}, \Delta m^2_{13}$) are related via the following relation:

$$\Delta m^2_{31} = \Delta m^2_{12} + \Delta m^2_{32}. \tag{1.3}$$

The oscillation experiments showed that the Δm^2_{12} is much smaller than Δm^2_{23} and it is similar to Δm^2_{13}:

$$\Delta m^2_{21} << \Delta m^2_{32} \simeq \Delta m^2_{13}. \tag{1.4}$$

This hierarchical ordering of the mass splittings implicates a small angle θ_{13}, as it was proved by experimental measurement.

The neutrino oscillation experiments have shown that there are three mass eigenstates. Since the absolute neutrino mass is still unknown, there is three possible mass orderings (see fig. 1.1):

- *normal hierarchy*: $m_3 > m_2 > m_1$, $\Delta m^2_{23} > 0$;
- *inverted hierarchy*: $m_3 < m_1 < m_2$, $\Delta m^2_{23} < 0$;
- *degenerate case*: the lightest neutrino mass is much bigger than Δm^2_{23}, so $m_3 \simeq m_2 \simeq m_1$.

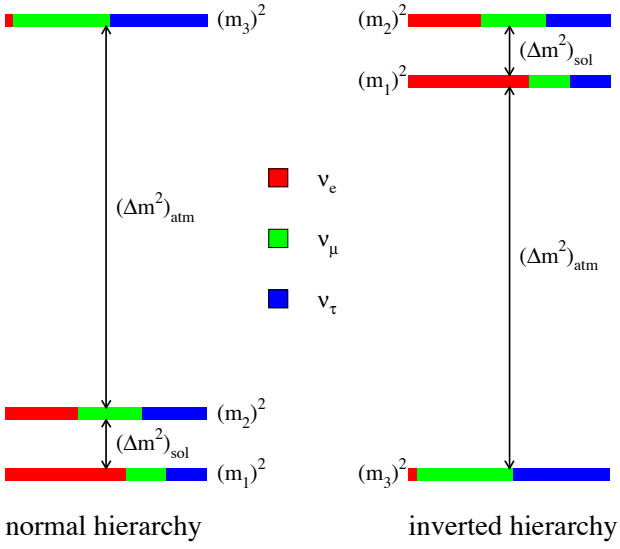

Figure 1.1: On the left normal hierarchy, on the right inverted hierarchy [12].

1.4 Neutrino nature: Dirac or Majorana?

The Dirac fermions are represented by a four components spinor ψ, which obeys the Dirac equation:

$$(i\gamma^\mu \partial_\mu - m)\psi = 0. \tag{1.5}$$

Given the *chirality* operator:

$$\begin{pmatrix} 0 & 1 \\ 1 & 0 \end{pmatrix},$$

the Dirac field can be described by two chirality eigenstates (*left-handed* and *right-handed* components):

$$\psi = \psi_L + \psi_R. \tag{1.6}$$

Only the *left-handed* component interacts in the weak interaction, so it is called *active* neutrino, while the *right-handed* component is the *sterile* neutrino.
In the Majorana theory the particle and his antiparticle are the same:

$$\psi = \psi^C, \tag{1.7}$$

where ψ^C is the charge-conjugated neutrino spinor. The Majorana condition implies that the *left-handed* and *right-handed* components are not independent, like in the Dirac case, because the *right-handed* component is the C-conjugate of *left-handed* components:

$$\psi_R = C\bar{\psi}_L^T = \psi_L^C, \tag{1.8}$$

where C is the charge-conjugated operator. The Majorana fermion [13] field is described by:

$$\psi = \psi_L + \psi_L^C. \tag{1.9}$$

Only neutrino fields can obey the Majorana condition because neutrino is a neutral particle. The charged particles interact by electromagnetic field, so ψ and ψ^C fields obey to different equations:

$$(i\gamma^\mu \partial_\mu - q\gamma^\mu A_\mu - m)\psi = 0 \tag{1.10}$$

$$(i\gamma^\mu \partial_\mu + q\gamma^\mu A_\mu - m)\psi^C = 0. \tag{1.11}$$

To better understand the difference between Dirac and Majorana particle the *helicity* operator is introduced. This is defined as the projection of the spin onto the direction of the momentum:

$$H = \frac{\overrightarrow{\sigma} \times \overrightarrow{p}}{|\overrightarrow{p}|}. \tag{1.12}$$

The Dirac *left-handed* ε_l component goes into *right-handed* ε_r component under Lorentz transformation and it goes into antiparticle *right-handed* $\bar{\varepsilon}_r$ component under CPT transformation. Instead the Majorana *left-handed* component ε_l goes into *right-handed* component ε_r under both transformations (see fig. 1.2).

The Lagrangian mass term ($L = m\bar{\psi}\psi$) for a Majorana neutrino can be written as:

$$L_M = \frac{1}{2} m(\bar{\nu}_L \nu_L^C + \bar{\nu}_L^C \nu_L). \tag{1.13}$$

If neutrino has both Dirac and Majorana mass, the Lagrangian mass term is a combination between two mass terms [11]:

$$L_{mass} = m_D(\bar{\nu}_L \nu_R + \bar{\nu}_R \nu_L) + \frac{m_L}{2}(\bar{\nu}_L \nu_L^C + \bar{\nu}_L^C \nu_L) + \frac{m_R}{2}(\bar{\nu}_R \nu_R^C + \bar{\nu}_R^C \nu_R), \tag{1.14}$$

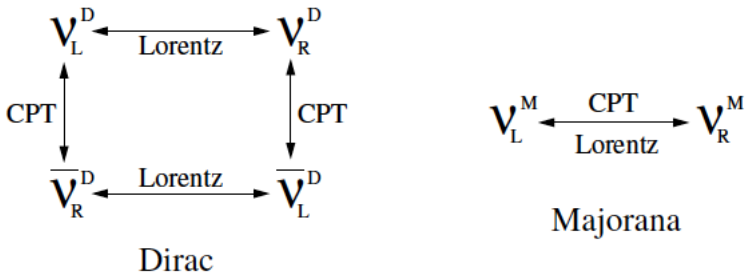

Figure 1.2: Dirac particle on the left, Majorana particle on the right.

where ν_L and ν_R are two independent fields, m_L, m_R are Majorana mass terms and m_D is the Dirac mass term.
The mass matrix can be written as:

$$U = \begin{pmatrix} 0 & m_D \\ m_D & m_R \end{pmatrix},$$

where the mass term m_L has been set to zero to preserve the $SU(2) \bigotimes U(1)$ symmetry.
The diagonal mass matrix form is given by:

$$U = \begin{pmatrix} m_1 & 0 \\ 0 & m_2 \end{pmatrix},$$

and the corresponding mass eigenstates are ν_1 and ν_2. They are related to ν_L, ν_R^C thought the mass matrix:

$$\nu_1 = cos\theta\nu_L + sin\theta\nu_R^C \tag{1.15}$$
$$\nu_2 = -sin\theta\nu_L^C + cos\theta\nu_R. \tag{1.16}$$

The neutrino Lagrangian mass term can be written as a combination of ν_1 and ν_2:

$$L_{mass} = \frac{1}{2}m_1(\bar{\nu}_1\nu_1^C + \bar{\nu}_1^C\nu_1) + \frac{1}{2}m_2(\bar{\nu}_2\nu_2^C + \bar{\nu}_2^C\nu_2). \tag{1.17}$$

This equation shows that the neutrino Lagrangian mass term is described only by the Majorana field even if the neutrino has both Dirac and Majorana mass. The Dirac mass m_D is expected to be of the same order of magnitude as the fermion mass because it is generated by Higgs mechanism. In addition there are no limitations for the Majorana mass m_R.
Considering the case in which the Majorana mass is much bigger than Dirac mass, $m_R >> m_D$:

$$\begin{cases} \nu_1 \simeq \nu_L, & m_1 \simeq \frac{m_D^2}{m_R} \\ \nu_2 \simeq \nu_R^C, & m_2 \simeq m_R \end{cases},$$

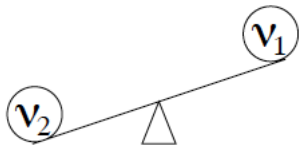

Figure 1.3: Illustration of the see-saw mechanism. The heavier the mass of ν_2 is, the lighter the mass of ν_1.

then the heavy mass of ν_2 is responsible of light mass of ν_1 (see figure 1.3). This phenomena, called *"see-saw mechanism"*, is very important because it can explain the smallness of the neutrino mass respect the lepton mass. The lightest neutrino, purely *left-handed* is the observed *active* neutrino. The heavy neutrino, purely *right-handed*, is still not observed *sterile* neutrino.

1.5 Constraints on neutrino mass

The great interest in investigating neutrino properties raises from a strong correlation between neutrino physics and other fields. A deeper understanding of the neutrino nature and the precise knowledge of its mass would provide important information about the dominance of matter over antimatter. In this sense the mass scale determination represents a way to better understand the basic theory of fundamental physics interaction.
Neutrino oscillation experiments gave a much clearer picture of neutrino physics, but they are not able to define the absolute value and hierarchy of neutrino mass. There are three different approaches to obtain constraints on neutrino mass:

- **single β decay experiments**: the neutrino mass is estimated from the endpoint of beta spectrum;
- **cosmological observation**: Large Scale Structure and the anisotropy in the Cosmic Microwave Background provide constraints on the sum of mass eigenstates;
- **neutrinoless double beta decay experiments**: $0\nu\beta\beta$ rare decay forbidden in the SM implicates the Majorana nature of neutrino. The neutrino mass can be estimated from decay rate.

1.5.1 Oscillation experiments

The most decisive measurements of solar neutrino oscillation come from SNO and KamLAND.
SNO (Solar Neutrino Observatory) [14] was a spherical Cerenkov detector

with 1000 t of pure heavy water D_20. It demonstrated the ν_e oscillation in other flavors by measuring charged and neutral scattering. All neutrino types interact by neutral current process (NC) $\upsilon + d \rightarrow n + p + \upsilon$ with the same cross section, instead only ν_e neutrinos interact by charge current process (CC) $\upsilon_e + d \rightarrow p + p + e^-$. The total flux of solar neutrinos measured by neutral current process was in agreement with Standard Solar Model prediction. On the contrary the ν_e flux measured by charge current proved the oscillation phenomenon.
KamLAND (Kamioka Liquid Scintillator AntiNeutrino Detector) [15] measured the oscillation parameters using antineutrinos produced by a nuclear reactor. It is constituted by a 1000 t of liquid scintillator in the old Kamioka mine. The $\bar{\nu}_e$ oscillation was measured by inverse beta decay: $\bar{\nu}_e + p \rightarrow e^- + n$. The value of Δm^2_{12} and θ_{12} have been measured by combining SNO and KamLAND data (see fig. 1.4): $\Delta m^2_{12} = (7.53 \pm 0.18) \times 10^{-5} eV^2$,
$\theta_{12} = 0.846 \pm 0.021$.

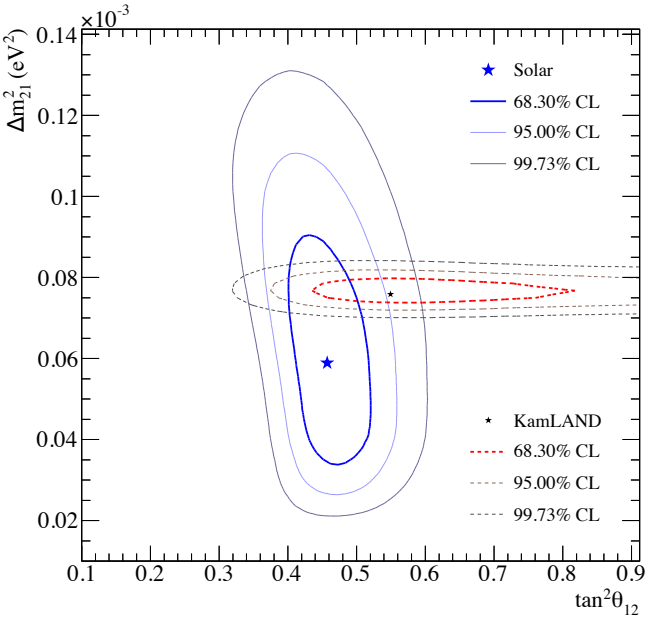

Figure 1.4: Combination of SNO and KamLAND to estimate the oscillation parameters [16].

The oscillation phonomenon was also observed in atmospheric neutrinos by the Super-KAMIOKANDE experiment [17]. The atmospheric neutrinos are produced by interaction between the cosmic ray and the atmosphere. Super-KAMIOKANDE is a Cerenkov detector, located in Kamioka mine, that detects the atmospheric neutrinos by charged-current interaction with nuclei $\nu_l + N \rightarrow l + N'$. The flux of upward-going and downward-going

neutrinos at the detector site would be symmetric. Super-KAMIOKANDE found a clear asymmetry between upward-going and downward-going neutrinos (see fig. 1.5).

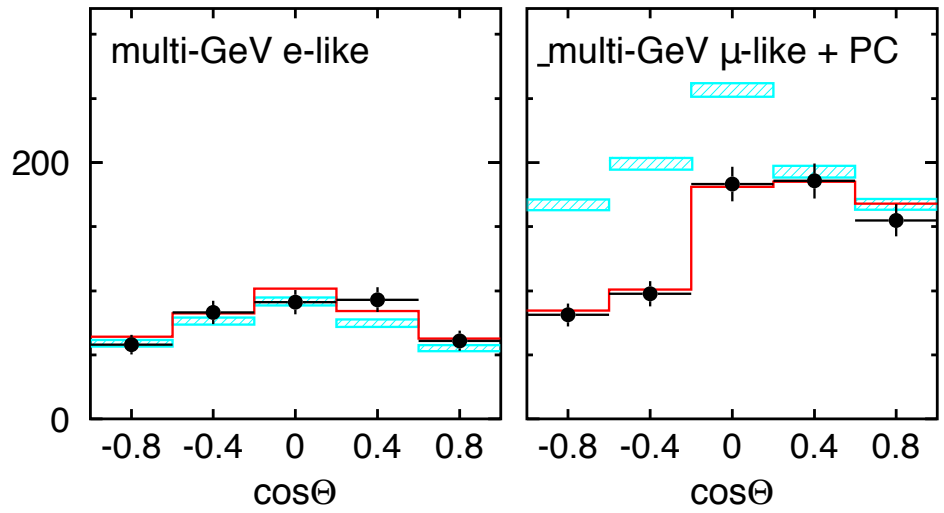

Figure 1.5: Zenith angle distribution of the muon neutrinos obtained by Super-KAMIOKANDE. On the left the distribution is right-left symmetric, and is in good agreement to the expectation without neutrino oscillation (blue line). On the right the observed number of upward-going muon neutrinos is half of the predictions. this effects is explained by neutrino oscillation (red line) [17].

The neutrino oscillation was confirmed by accelerator-based and long baseline experiments, which performed the estimation of atmospheric parameters. The most sensitive estimation of Δm^2_{23} and θ_{23} came from the second generation long baseline experiments, T2K [18] and $NO\nu A$ [19]. Both of them produce a narrow beam with mean energy close to the oscillation maximum to increase the neutrino flux and to minimize the background.
The first sensitive estimation of θ_{13} come from DAYA BAY [20], a reactor neutrino experiment designed to improve the measurement of electron antineutrino disappearance: $\overline{\nu_e} + p \rightarrow n + e^-$. The value of $sin^2(\theta_{13})$ is $0.089 \pm 0.010(stat) \pm 0.005(syst)$.
The results of neutrino oscillation parameters are listed in table 1.1 in term of best fit values and allowed 2σ ranges for the 3ν mass- mixing parameters.

1.5.2 Single beta decay

The direct electron neutrino mass determination is purely based on kinematics without further assumptions. Essentially, the electron neutrino mass

Parameter	Hierarchy	Best Value	2σC.L.
Δm^2_{12}	NH or IH	7.37 x 10^{-5}eV	7.07-7.73 x 10^{-5} eV
$sin(\theta_{12})$	NH or IH	0.297	2.65-3.34
Δm^2_{23}	NH	2.50 x 10^{-3}eV	2.41-2.58 x 10^{-3}eV
Δm^2_{23}	IH	2.46 x 10^{-3}eV	2.38-2.55 x 10^{-3}eV
$sin(\theta_{13})$	NH	0.014	0.0195-0.0036
$sin(\theta_{13})$	IH	0.018	0.0196-0.0238
$sin(\theta_{23})$	NH	0.437	0.397-0.563
$sin(\theta_{23})$	IH	0.569	0.404-0618
δ/π	NH	1.35	0.92-1.99
δ/π	IH	1.32	0.83-1.99

Table 1.1: Measured values of neutrino mixing parameter. NH stays for normal hierarcchy. IH stays for inverted hierarchy [21].

is determined by using the relativistic energy-momentum relation $E^2 = m^2 + p^2$. Therefore it is sensitive to the neutrino mass squared m^2_ν, that is estimated from endpoint of beta spectrum. The electron neutrino mass is given by a superposition of three mass eigenstates:

$$m^2_\nu = \Sigma |U^2_{ei}| m^2_{\nu i}. \tag{1.18}$$

The best β candidate to search absolute neutrino mass is tritium [22]. The tritium β decay is:

$$^3H \rightarrow ^3 He + e^- + \overline{\nu_e}, \tag{1.19}$$

which has an endpoint energy of 18.6 keV and a half-life of 12.3 yr.

The tritium is chosen because it has one of the smallest Q-value of all β emitters with a relativity short half-life, which implies an acceptable number of observed events during the experiment lifetime. The tritium electronic structure is simpler than heavier nuclei, so the β spectrum can be measured with small systematic uncertainties.

The technique used in the tritium experiments is the MAC-E-Filter (Magnetic Adiabatic collimation with an Electrostatic Filter), which combines high luminosity at low background and a high energy resolution, that are essential features to measure the neutrino mass in the endpoint region of electron spectrum. The isotropic β beam is transformed into a broad one flying almost in the same direction of magnetic field line. This means that the spectrometer acts as high-pass filter: only the electrons with enough energy to pass the electrostatic barrier are re-accelerated and collimated onto the detector while all others are reflected.

The MAC-E-Filters technique was used by the Troitsk and the Mainz experiments, which have an energy resolution respectively of 3.5 eV and 4.5 eV. Thanks to this innovative technique these experiments obtained significant

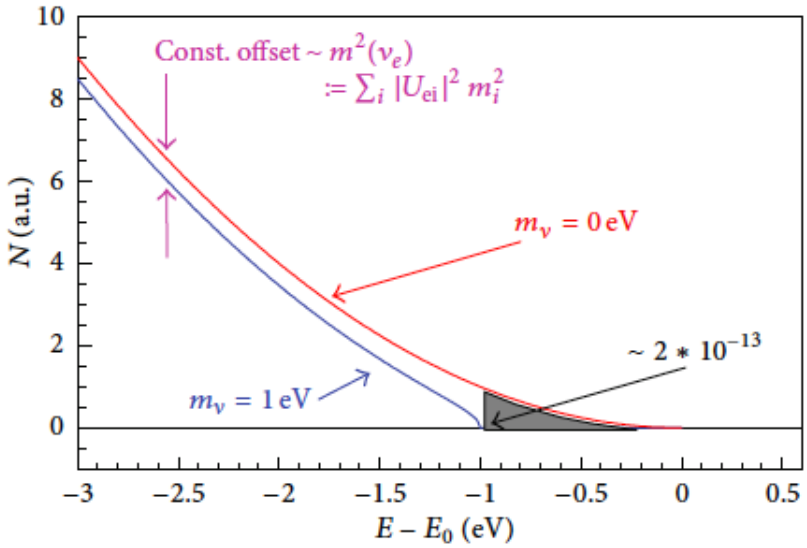

Figure 1.6: Expanded βspectrum of an allowed or superallowed β decay around its endpoint E_0 for $m_\nu = 0$(red line) and for an arbitrarily chosen neutrino mass of 1 eV (blue line). The gray-shaded area corresponds to a fraction of 2×10^{-13} of all tritium β decay [22].

results on the electron neutrino mass: $m_e < 2.1$ eV for the Troitsk experiment [23] and $m_e < 2.3$ eV for the Mainz experiment [24].
The upcoming KATRIN experiment (Karlsruke Tritium Neutrino) [25] develop MAC-E-Filters to reach a high energy resolution of 0.93 eV. It was designed to improve the sensitivity to the electron neutrino mass by a factor 10 to the present limit at 90% C.L..
Actually alternative methods are being developed for direct neutrino mass measurement. Project 8 [26] uses the technology from KATRIN gaseous tritium source combined with a sensitive array of microwave antennae to extract energy spectra of tritium decay electrons from the coherent cyclotron radiation emitted by individual electrons in a magnetic field. Experiment like ECHO [27], HOLMES [28], NuMES [29], use cryogenic detectors to study holmium electron capture decay:

$$^{163}\text{Ho} \rightarrow ^{163}\text{Dy}^* + \nu_e \rightarrow ^{163}\text{Dy} + E_C \tag{1.20}$$

which has an endpoint energy of 2.8 keV and a half-life of 4570 yr [30].
The sensitivity goal of direct neutrino mass experiments is $m_\nu < 200$ meV at 90% C.L. [31] .

1.5.3 Neutrino cosmology

Relic neutrinos play an important role in the evolution of the Universe and the implication of massive neutrinos has a strong impact on the cosmological observables. The number of relic neutrinos is slightly below that of relic photons that constitute the cosmic microwave background (CMB) [32]. The evidence of Cosmic Neutrino Background (CNB) has not been observed yet, but the study about the CMB spectrum and other cosmology observable prove its presence. In the early universe the three neutrino flavors are in thermal equilibrium with the primordial plasma through weak interaction, while they start decoupling from the rest of the plasma when the universe expanded and cooled.
The CMB anisotropies, in particular CMB lensing, and the large scale structure (LSS) can be used to estimate the sum of neutrino masses and the number of neutrino species. The contribution of neutrino to total radiation can be parametrized by the neutrino species numbers [33]:

$$\rho = \rho_\gamma + \rho_\nu = \left[1 + \frac{7}{8}\left(\frac{4}{7}\right)^{\frac{4}{3}} N_{eff}\right]\rho_\gamma. \tag{1.21}$$

The contribution to the matter density is related to the sum of neutrino mass:

$$\Omega_\nu = \frac{\sum_i m_i}{93.14 h^2 eV}. \tag{1.22}$$

Depending of hierarchy order, the $\sum_i m_i$ can be expressed by a function of the lightest neutrino mass m. In the case of normal hierarchy:

$$\begin{cases} m_1 &= m \\ m_2 &= \sqrt{m^2 + \delta m^2} \\ m_3 &= \sqrt{m^2 + \Delta m^2 + \delta m^2/2} \end{cases}.$$

In the case of inverse hierarchy:

$$\begin{cases} m_1 &= \sqrt{m^2 + \Delta m^2 - \delta m^2} \\ m_2 &= \sqrt{m^2 + \Delta m^2 + \delta m^2/2} \\ m_3 &= m \end{cases}$$

where δm^2 can be approximated with Δm^2_{12}, and Δm^2 with Δm^2_{13} [34].
The Plank Satellite [35], lunched in the 2009, confirmed that neutrino exist in three species and gave the most precise estimation of the sum of three mass eigenstates: $\mathrm{N}_{eff} = 3.04 \pm 0.18$, $\sum m_i < 0.17 eV$.

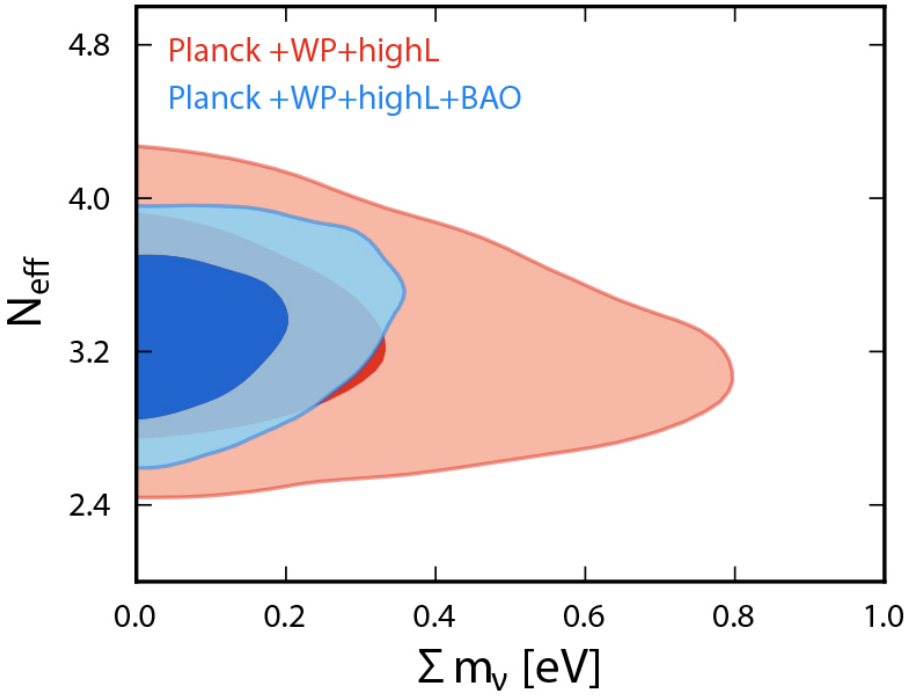

Figure 1.7: Plank results on the effective neutrino family number and on the sum of neutrino masses [35].

Chapter 2

Neutrinoless double beta decay

2.1 Double beta decay

The double beta decay is a second order process in which a nucleus changes its atomic number by two units:

$$(A, Z) \rightarrow (A, Z \pm 2). \tag{2.1}$$

It occurs for some even-even nuclei because the single beta decay is kinematically forbidden or it is suppressed by large change in angular momentum (see fig. 2.1). Two double beta decay modes can be considered: the two neutrino double beta decay ($2\nu\beta\beta$) and the neutrinoless double beta decay ($0\nu\beta\beta$), in which no neutrinos are emitted:

$$2\nu\beta\beta: \quad (A, Z) \rightarrow (A, Z \pm 2) + 2e^{\mp} + 2\overline{\nu}_e(\nu_e) \tag{2.2}$$

$$0\nu\beta\beta: \quad (A, Z) \rightarrow (A, Z \pm 2) + 2e^{\mp} \tag{2.3}$$

The Feynman diagrams for the two DBD modes are depicted in figure 2.2.

The two neutrino double beta decay is a process allowed by the Standard Model. It can be modeled as two successive single beta decays passing through virtual intermediate nuclear states and it does not require special proprieties of the neutrino. This process was first detected in 1987 in ^{82}Se [36] and it has been then observed for various other isotopes. Being a second order process in the weak interaction, half-lives for nuclei which undergo double beta decay are very long, of the order of $10^{18} - 10^{24}$ yr [37]. Table 2.1 shows $2\nu\beta\beta$ half-lives observed for various isotopes.

The double beta decay without neutrino emission is a rare process forbidden by Standard Model because it violates the lepton number conservation by two units.

The $0\nu\beta\beta$ decay can occur trough several mechanisms. All mechanisms are

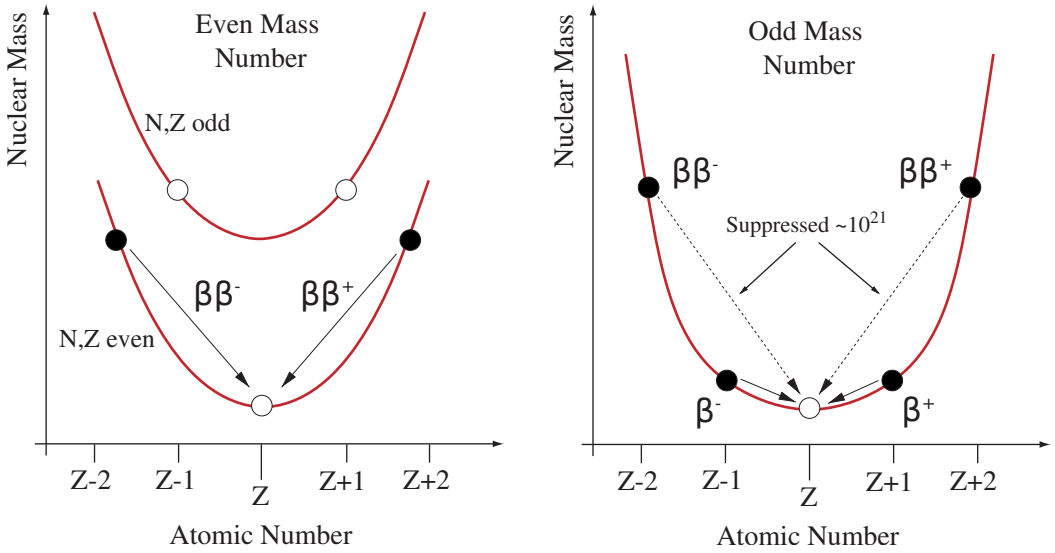

Figure 2.1: Atomic mass m as a function of atomic number Z for even A (left plot) and odd A (right plot) energy.

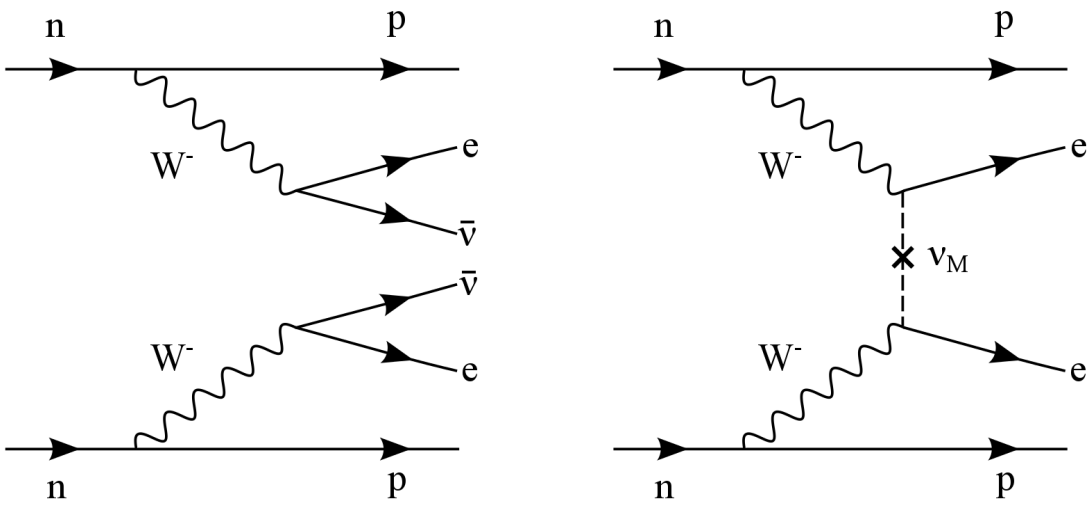

Figure 2.2: Two neutrino double beta decay on the left, double beta decay without neutrino emission on the right.

DBD reaction	$T^{0\nu}_{1/2}$ [yr]
^{48}Ca $\rightarrow^{48}$ Ti	$(4.4 \pm 0.64) \times 10^{19}$
^{76}Ge $\rightarrow^{76}$ Se	$1.84^{+0.14}_{-0.10} \times 10^{21}$
^{82}Se $\rightarrow^{82}$ Kr	$(9.2 \pm 0.7) \times 10^{19}$
^{96}Zr $\rightarrow^{96}$ Mo	$(7.1 \pm 0.4) \times 10^{19}$
^{116}Cd $\rightarrow^{116}$ Sn	$(2.88 \pm 0.17) \times 10^{19}$
^{128}Te $\rightarrow^{128}$ Xe	$(7.7 \pm 0.4) \times 10^{24}$
^{130}Te $\rightarrow^{130}$ Xe	$6.8^{+1.2}_{-1.1} \times 10^{20}$
^{136}Xe $\rightarrow^{136}$ Ba	$2.38 \pm 0.02(stat) \pm 0.14(syst) \times 10^{21}$
^{150}Nd $\rightarrow^{150}$ Sm	$(8.2 \pm 0.9) \times 10^{18}$
^{238}U $\rightarrow^{238}$ Pu	$(2.0 \pm 0.6) \times 10^{21}$

Table 2.1: Observed two neutrino double beta decay half-lives for various isotopes. The value are taken from [39], [40], [41], [42], [43].

based on the violation of the lepton number conservation and on specific neutrino proprieties. The simplest mechanism is described by the exchange of a virtual neutrino (fig. 2.2b) that is produced as neutrino at one vertex and it is absorbed as antineutrino at another vertex. The helicity flip requires the non zero mass of neutrino and its Majorana nature, because antineutrinos are right handed while neutrinos is left handed. The helicity flip and the smallness of neutrino mass cause the low rate of $0\nu\beta\beta$ decay.
Assuming only the three known light Majorana neutrinos are involved in the reaction, the rate of $0\nu\beta\beta$ decay is given by [38]:

$$\left[T^{0\nu}_{1/2}\right]^{-1} = G^{0\nu}(Q,Z)|M^{0\nu}|^2 \langle m_{\beta\beta}\rangle^2 , \tag{2.4}$$

where the $G^{0\nu}$ is the phase space factor and the $M^{0\nu}$ is the nuclear matrix element. $\langle m_{\beta\beta}\rangle^2$ is the effective Majorana mass that can be written as a combination of mass eigenvalues:

$$m_{\beta\beta} = \left| \sum_{i=1}^{3} A_i U^2_{ei} m_i \right| , \tag{2.5}$$

where $A_i = diag(e^{i\alpha_1}, e^{i\alpha_2}, 1)$ is a diagonal matrix including the two Majorana phases, U is PMNS mixing matrix, and m_j are the neutrino eingenstates.
The $0\nu\beta\beta$ decay has never been observed and only lower limits on its half-life $T^{0\nu}_{1/2}$ have been set so far. The experimental limits are listed in table 2.2.

2.1.1 Prediction on Majorana mass

The observation of $0\nu\beta\beta$ decay would imply that neutrino have a Majorana mass component and total lepton number violation, it would also provide

Isotope	$T^{0\nu}_{1/2}$ [yr]	Reference
^{48}Ca	$> 1.4 \times 10^{22}$	[44]
^{76}Ge	$> 3.0 \times 10^{25}$	[45]
^{87}Se	$> 1.0 \times 10^{23}$	[46]
^{100}Mo	$> 1.1 \times 10^{24}$	[47]
^{130}Te	$> 4.0 \times 10^{24}$	[48]
^{136}Xe	$> 1.1 \times 10^{25}$	[49]
^{150}Nd	$> 1.8 \times 10^{22}$	[50]

Table 2.2: Limits on $T^{0\nu}_{1/2}$ for $\beta\beta$ candidates.

important information on the absolute scale of neutrino mass and on the mass hierarchy.
The effective Majorana mass term depends on hierarchy order because it is related to the lightest neutrino eigenvalue. This relation depends on whether the hierarchy is normal or inverted because the lightest neutrino mass eigenvalue depends itself on the hierarchy. Considering the normal hierarchy case in which m_1 is the lightest mass eigenvalue, the Majorana effective mass can be written:

$$\begin{aligned} m_{\beta\beta} &= |U^2_{e1} m_1 + U^2_{e2} m_2 + U^2_{e1} m_3| \\ &= |U^2_{e1} m_1 e^{i\alpha_1} + U^2_{e2}\sqrt{\Delta {m_{12}}^2 e_{i\alpha_2} + m_1^2} + U^2_{e3}\sqrt{\Delta {m_{13}}^2 + m_1^2}| \\ &= |cos^2\theta_{12} cos^2\theta_{13} e^{i\alpha_1} m_1 + sin^2\theta_{12} cos^2\theta_{13} e^{i\alpha_2}\sqrt{\Delta {m_{12}}^2 + m_1^2} + sin^2\theta_{13}\sqrt{\Delta {m_{13}}^2 + m_1^2}|, \end{aligned} \tag{2.6}$$

where $\alpha_1$and α_2 are Majorana phases. A similar equation is easily obtained for the inverted mass hierarchy in which m_3 is the lightest mass eigenvalue. Introducing in the previous expression the measured values of mixing angle and the mass-squared splittings, a value of $m_{\beta\beta}$ is evaluated for each value of lightest neutrino mass (m_1 for *NH* or m_3 for *IH*). The value of CP violating phases (α_1, α_2, δ) are still unknown, so the predictions on $m_{\beta\beta}$ are obtained by letting them vary freely.
The prediction on $m_{\beta\beta}$ as a function of the lightest neutrino mass are reported in figure 2.3(a): the red zone is the allowed zone for the normal hierarchy and the green zone for the inverted hierarchy, the overlap of the two zones correspond to the degenerate case.
The effective Majorana mass can also be inferred by the cosmological observation of the total neutrino mass Σ, given by the sum of three active neutrino masses. Furthermore, the measurements of Σ have recently reached important sensitivities, as discussed in the previous chapter.
The observable Σ, can be written as function of the lightest mass eigenvalue:

$$\Sigma = m_l + \sqrt{m_l^2 + a^2} + \sqrt{m_l^2 + b^2}, \tag{2.7}$$

where m_l is the mass of the lightest neutrino and a and b are different constants depending on the neutrino mass hierarchy. Through this equation one can establish a direct relation between Σ and m_l and thus it is straightforward to plot $m_{\beta\beta}$ as a function of Σ. Figure 2.3(b) shows the value of $m_{\beta\beta}$ as a function of Σ in the normal (orange) and inverted hierarchy (blue).
The observation of $0\nu\beta\beta$ decay would prove the Majorana nature of neutrino and it is the unique process experimentally investigated to define that. On the contrary, if the process is not observed, the Dirac nature of neutrino cannot be confirmed: the presence of the vertical dip in the normal hierarchy band, which corresponds to a particular combination of the two Majorana phases, indicates that $m_{\beta\beta}$ could vanish even if neutrinos are Majorana particles.

2.1.2 Nuclear matrix elements

The extrapolation of $m_{\beta\beta}$ from measurement on limit of $T^{0\nu}_{1/2}$ is related to the knowledge of the phase space factor $G^{0\nu}$ and the nuclear matrix elements $M^{0\nu}$ (see eq 2.4). The $\beta\beta$ candidates have different phase space factors and nuclear matrix elements (NME), so their knowledge is necessary to compare the results of different experiments. Since the observation of $0\nu\beta\beta$ decay for an isotope is not enough to make the discovery, the confirmation and the comparison with different isotopes is needed to exclude that the observed signal comes from another process able to mimic the $0\nu\beta\beta$ signature. $G^{0\nu}$ represents the kinematic contribution of the decay and is proportional to the $Q^5_{\beta\beta}$, so a high Q-value means a higher probability that the decay occurs. $G^{0\nu}$ is precisely calculable, while the matrix elements $M^{0\nu}$ are the biggest source of theoretical uncertainty and cannot be determinated experimentally. The calculation of $M^{0\nu}$ is a many bodies problem depending on the nuclear structure of parent and daughter nuclei. Recently different theoretical approximations have been largely improved. The principal methods used are:

- *Interacting Shell Model* (ISM) [53], [54]: only a limited number of orbits around the Fermi level are considered but all the possible correlations within the space are included and the pairing correlations in the valence space are treated exactly. A good spectroscopy for parent and daughter nuclei is achieved;

- *Quasiparticle Random Phase Approximation* (QRPA) [55], [56]: cannot comprise all the possible configurations. Typically, single particle states in a Woods-Saxon potential are considered. The proton-proton and neutron-neutron pairings are taken into account and treated in the BCS approximation (proton and neutron numbers are not exactly conserved);

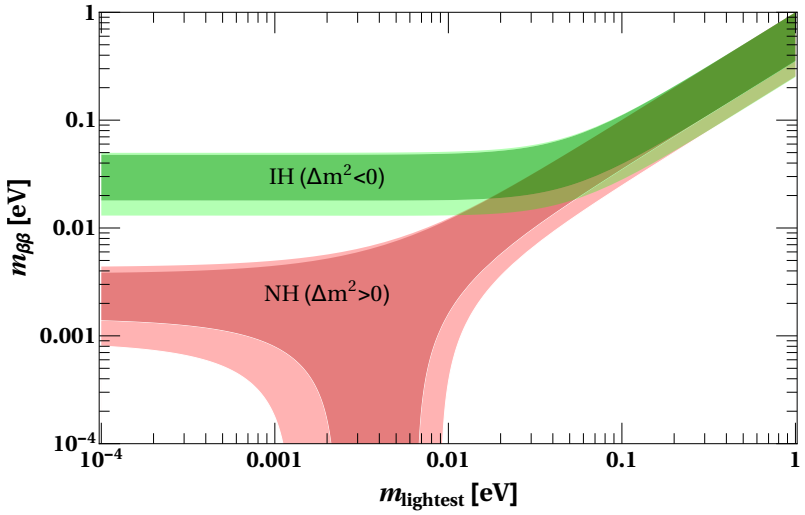

(a)

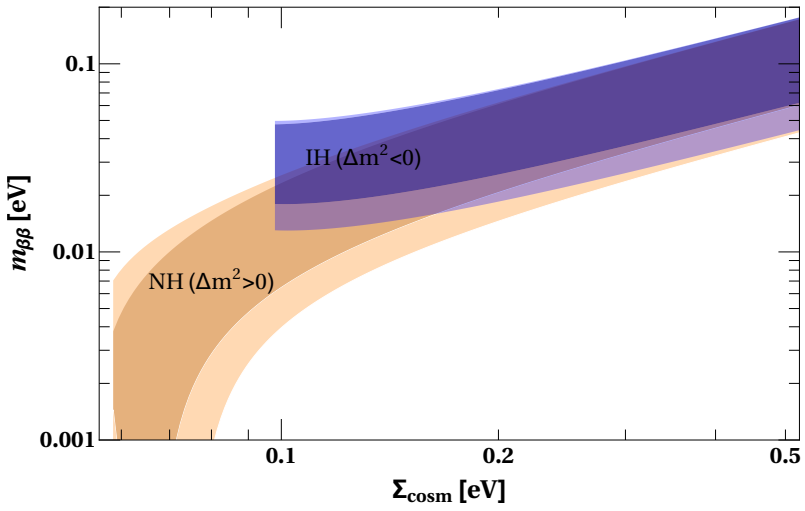

(b)

Figure 2.3: Predictions on $m_{\beta\beta}$ from oscillations as a function of the lightest neutrino mass (top) and of the sum of neutrino mass (bottom) in the two cases of *NH* and *IH*. The shaded areas correspond to the 3σ regions due to error propagation of the uncertainties on the oscillation parameters [51].

- *Interacting Boson Model* (IBM-2) [57]: the low lying states of the nucleus are modeled in terms of bosons. The bosons are in either s boson (L = 0) or d boson (L = 2) states. Therefore, one is restricted to 0+ and 2+ neutron pairs transforming into two protons. The bosons interact through one and two body forces giving rise to bosonic wave functions.

In figure 2.4 the comparison among the NME computed for different isotopes with these three different models is shown. The model used to compute the nuclear matrix elements depends on the isotope.

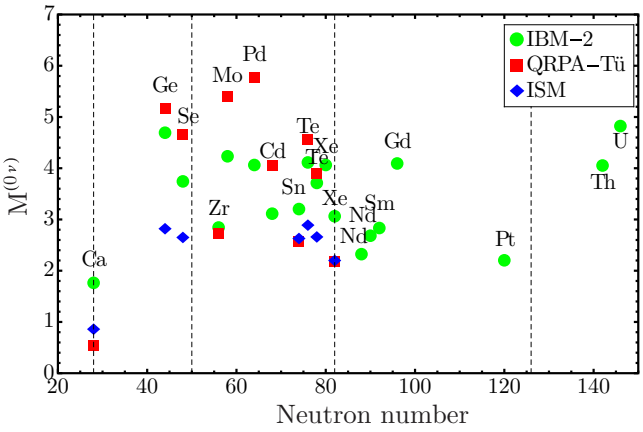

Figure 2.4: Most updated NMEs calculations for the $0\nu\beta\beta$ with the IBM-2, QRPA and ISM models. Figure from [57].

2.2 Lepton number violation

The observation of neutrino oscillation shows that the flavor lepton number is violated, instead the total lepton number violation has never been observed.
The conservation of total lepton number, as the baryon one, has not a deep justification. In the Standard Model lepton and baryon numbers are conserved quantity because an elementary process in which one of them varies has not been observed yet. In fact, it is suspected that the total lepton number conservation is not a basic law, but just an approximate symmetry related to the energy range that can be explored at the laboratory.
The $0\nu\beta\beta$ decay represents a process beyond the Standard Model in which the total lepton number conservation is violated. This process is based on the neutrino-antineutrino oscillation:

$$\nu \rightarrow \overline{\nu}, \tag{2.8}$$

that is similar to the case of neutrino flavors oscillation.
The observation of this process could solve an important question about the Universe: *why does matter dominate over antimatter?*.
Cosmology studies show that, in the early universe, the number of baryons [58] is:

$$\eta_\beta = \frac{\eta_\beta - \overline{\eta_\beta}}{\eta_\gamma} = (6.047 \pm 0.0074) \times 10^{-10}, \tag{2.9}$$

where η_β is the baryons density, $\overline{\eta_\beta}$ is the anti baryons density and η_γ the photons density.
Several models try to explain baryon asymmetry, all of which are based on the Sakharov conditions [59]:

1. any model must have a mechanism that violates the baryon number conservation;
2. that mechanism must also violate C-symmetry and CP-symmetry:
3. the mechanism must be active while the Universe was not in thermal equilibrium.

The most attractive model is the *baryogenesis via leptogenesis* [60] where the baryon asymmetry is generated by an excess of leptons. This theory is related to see-saw mechanism and non conservation of lepton number.
The excess of leptons was generated by RH heavy neutrino, which decay in two different modes:

$$\begin{cases} N_i & \to H + l \\ N_i & \to H^+ + \bar{l} \end{cases}$$

Since the RH neutrino and Higgs boson (H) do not carry lepton charge, both processes violate the conservation of lepton number. Through CP violation of N decays from tree-loop interface diagrams (see fig. 2.5), an asymmetry in the rates of the two processes can be generated to produce an excess of leptons.

2.3 Fundamentals for the search of $0\nu\beta\beta$ decay

The signature of $0\nu\beta\beta$ decay is a peak in the sum electrons spectrum at the Q-value of the reaction. The Q-value is given by the difference between the parent and daughter mass, subtracted by the sum of two emitted electron masses:

$$Q_{\beta\beta} = M_p - M_d - 2m_e. \tag{2.10}$$

The $2\nu\beta\beta$ electrons spectrum is continuous because part of the energy is carried away by the two neutrinos. In the $0\nu\beta\beta$ decay the total energy goes into two emitted electrons, so the signature is given by a monochromatic line at Q-value in the sum electrons spectrum (see fig 2.6).

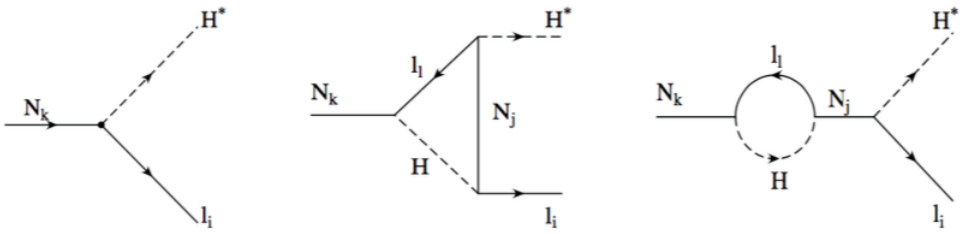

Figure 2.5: Tree-loop interface Feyman diagrams contributing to heavy neutrino decays leading to leptogenesis.

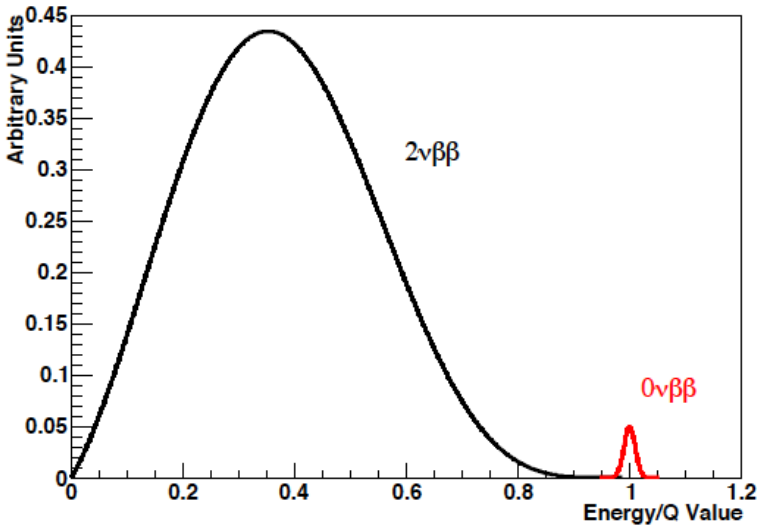

Figure 2.6: Summed electrons energy spectrum for double beta decay.

The observation of $0\nu\beta\beta$ decay is a challenging task from the experimental point of view. The current experimental method is based on the detection of the two emitted electrons. The main difficulty is the discrimination between $0\nu\beta\beta$ and background events, given by $2\nu\beta\beta$ decay and natural radioactivity.

2.3.1 The sensitivity

The most important parameter characterizing $0\nu\beta\beta$ experiments is the *sensitivity*. It is defined as the half-life corresponding to the minimum number of signal events observable above background at a given statistical significance (n_σ) [61]:

$$S^{0\nu}(n_\sigma) = \frac{ln2}{n_\sigma}\varepsilon N_a \frac{\eta}{A}\sqrt{\frac{M \times t}{B\Delta E}}, \tag{2.11}$$

where ε is the detector efficiency, N_a is the Avogadro number, η is the isotope abundance, A is the atomic mass number, M is the detector mass in kg, t is the live time of the experiment in years, B is the background expressed in $counts/(keV \cdot kg \cdot yr)$, ΔE is the energy resolution in keV.
The choice of the best $\beta\beta$ emitter is the first issue for DBD detectors. The criteria for the choice of the isotope are:

- *high isotopic abundance* η: to increase the the number of $0\nu\beta\beta$ events, as it is clear from Eq.2.11.
- *high Q-value* $Q_{\beta\beta}$: to suppress the background coming from natural radioactivity. A Q-value above 2615 keV [1] is preferred.

The principal isotope candidates are ^{48}Ca, ^{76}Ge, ^{82}Se,^{96},^{100} Mo, ^{116}Cd, ^{130}Te, ^{136}Xe, ^{150}Nd. All candidates have an isotopic abundance below 10%, except for ^{130}Te that has a natural isotopic abundance of 34.5%. Isotopic enrichment is therefore necessary in many cases.
To compare the discovery potential of experiments using different isotopes, the nuclear factor of merit is introduced:

$$F_N = m_e^2 G_{0\nu}|M_{0\nu}|^2, \tag{2.12}$$

it has dimension of yr^{-1}. In table 2.1 are reported the Q-value, the isotopic abundance and the nuclear factor of merit for some isotopes used in the search of $0\nu\beta\beta$ decay.
The background is a very delicate point for DBD experiment. There are several sources of background that need to be taken into account. They can be distinguished in internal, given by radioactive contamination in the detector material, and external, originated outside the detector.
The external background sources are:

[1] highest γ-line coming from natural radioactivity.

Candidate	$Q_{\beta\beta}$(MeV)	Abundance(%)	F_N $[yr^{-1}]$
^{48}Ca	4.27	0.187	0.54×10^{-13}
^{76}Ge	2.04	7.8	0.73×10^{-13}
^{82}Se	2.99	9.2	1.7×10^{-13}
^{100}Mo	3.03	9.6	5.0×10^{-13}
^{116}Cd	2.80	7.5	1.3×10^{-13}
^{130}Te	2.53	34.5	4.2×10^{-13}
^{136}Xe	2.45	8.9	0.28×10^{-13}
^{150}Nd	3.36	5.6	57×10^{-13}

Table 2.3: $\beta\beta$ candidate with a Q-value upper 2 MeV. The value of factor of merit are taken from [62].

- *muons*: their interactions produce high-energy secondary, as neutrons and electromagnetic showers;
- *neutrons*: produced by natural fission and (α,n) reactions;
- *radioactive isotopes*: produced by cosmogenic activation of the detector material.

The internal backgrounds are given by:

- detector contamination, mainly coming from ^{238}U and ^{232}Th chains (see figures 2.7 and 2.8);
- ^{222}Rn and ^{220}Rn that, being gases can easy diffuse trough the detector material.

The dominant background components depend on the detector technology. The external background can be suppressed by placing the detector underground and by enclosing it into a shielding system. At depths of underground facilities, muons are the only surviving component from cosmic rays. This background is generally rejected by veto systems. Neutrons flux can be suppressed by shielding the experimental setup with suitable neutron-catcher, while gamma rays are shielded by high Z material as lead and copper. The cosmogenic activation can be controlled by reducing the exposure of materials to cosmic-ray and by avoiding the use of nuclei with large activation cross-section.
Extremely accurate radio-purity control on detector components is required to reduce the internal background. The detectors are usually protected by radon contamination using small over pressure pure nitrogen in the experiment area.
In the CUORE case, the dominant background source is given by α surface contamination of the copper detector supports, as it will be discussed in the next chapter.

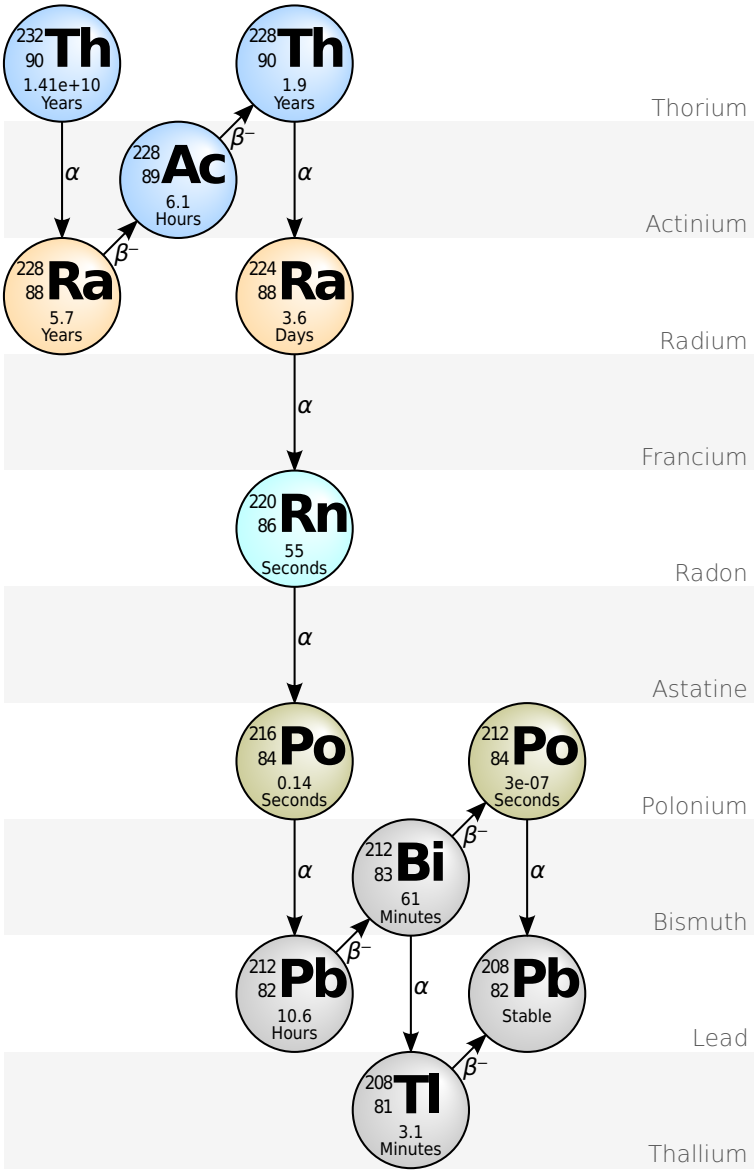

Figure 2.7: ^{232}Th chain.

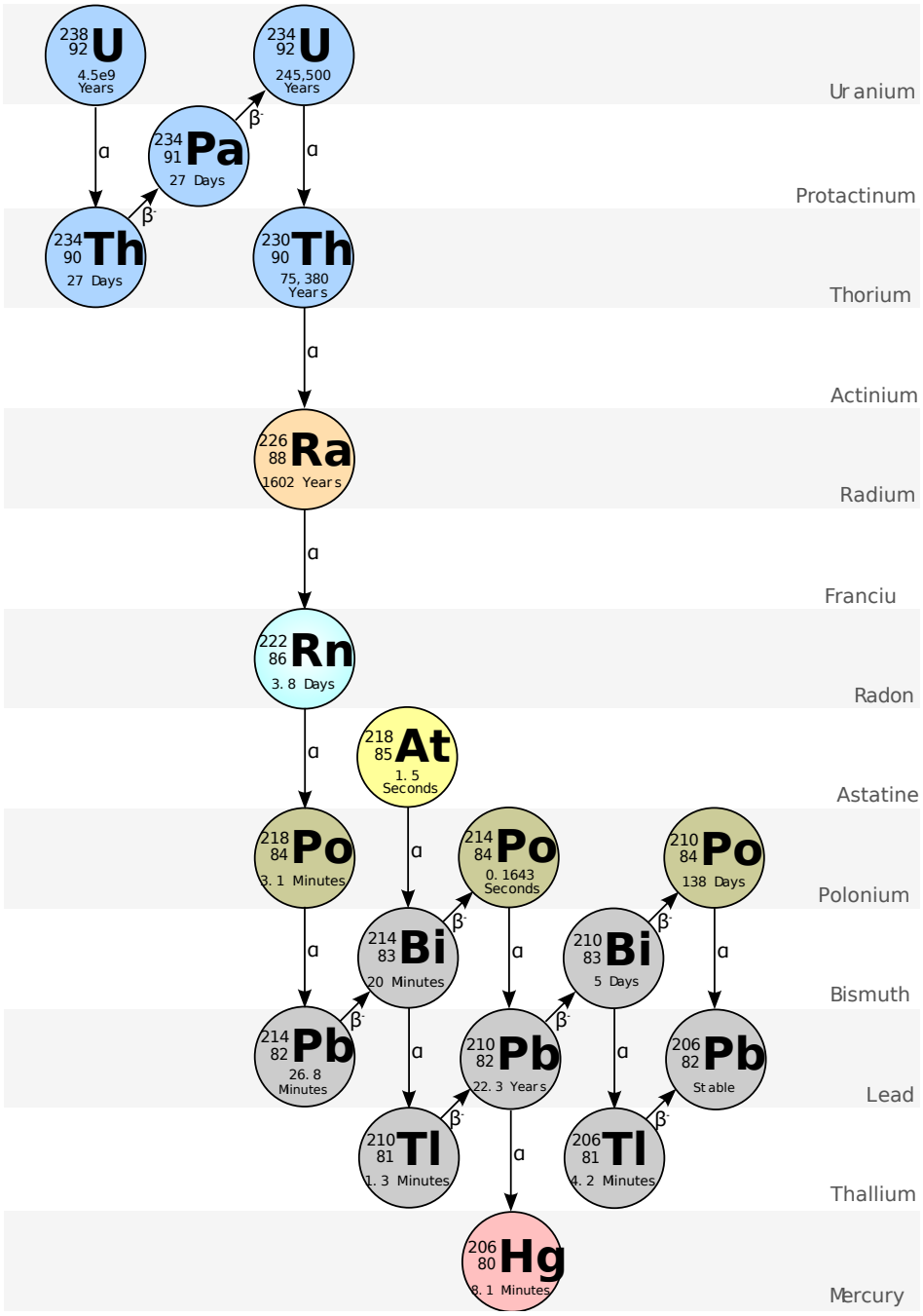

Figure 2.8: ^{238}U chain.

A high energy resolution is maybe the most relevant feature to identify the sharp $0\nu\beta\beta$ peak over an almost flat background. A good energy resolution is also the only protection against the intrinsic $2\nu\beta\beta$ background. The fraction F of $2\nu\beta\beta$ events contained in a ΔE energy window centered in the Q-value is given by:

$$F = \frac{S}{B} \approx \frac{m_e}{7Q_{\beta\beta}^5 \Delta E^6} \frac{T_{0\nu}^{1/2}}{T_{2\nu}^{1/2}}, \tag{2.13}$$

where $T_{0\nu}^{1/2}$ and $T_{2\nu}^{1/2}$ are respectively the half life of $0\nu\beta\beta$ and $2\nu\beta\beta$. The factor F depends strongly on the energy resolution; therefore, in order to discriminate the $0\nu\beta\beta$ events from the $2\nu\beta\beta$ intrinsic background, a good energy resolution is helpful.

2.3.2 Experimental technique

The $0\nu\beta\beta$ detectors can be classified in two main categories: calorimetric detectors in which source and detector coincide, and external source systems in which source and detector are two separate systems (see fig. 2.9).
The calorimetric technique has been implemented for different kind of de-

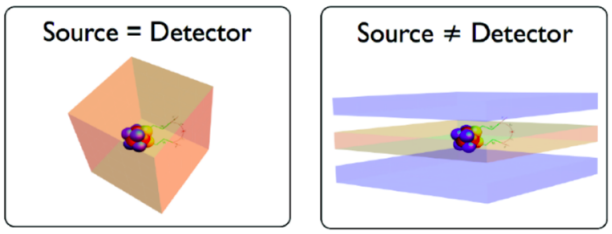

Figure 2.9: Two different approach to search the DBD: source = detector on the left, source ≠ detector on the right.

tectors: Ge-diodes, bolometers, liquid scintillators loaded with $\beta\beta$ isotope and liquid and gaseous Xe TPC. Thanks to the high efficiency of the calorimetric technique, large masses are achievable. Detectors with mass up to $\sim$ 300 kg have already proved to work and tonne-scale detectors seem possible. Ge-diodes and tellurium bolometers reach at the present the best energy resolution: respectively 3 keV and 5 keV around the Q-value of the reaction. Since these detectors have poor background rejection capability, they require a high radio-purity control of the used materials. On the contrary, liquid scintillators loaded with $\beta\beta$ isotope and liquid and gaseous Xe TPC have poor energy resolution but they reach low level of background thanks to the purification of liquid scintillators and the event topology reconstruction in TPC systems.

Besides having provided so far the best experimental results on $0\nu\beta\beta$, the calorimetric approach is still promising the best sensitivities and is therefore characterizing most of the future projects. The only disadvantage is that the calorimetric technique is not able to define event nature and topology, except for Xe-TPC.
In case of discovery of $0\nu\beta\beta$ decay, the topology reconstruction could represent a fundamental tool to understand the $0\nu\beta\beta$ mechanism.
External source detectors have good event topology reconstruction, thus making in principle easier to reach the zero background condition and to study the $0\nu\beta\beta$ mechanism. The detectors that are used are scintillators, solid state detector and gas chambers. The limit of this approach is the low efficiency, of order of 30%, and the low energy resolution that does not allow to distinguish between $0\nu\beta\beta$ events from $2\nu\beta\beta$ events.

2.4 Search for neutrinoless double beta decay

The most stringent limits on $0\nu\beta\beta$ half-life come from GERDA, CUORE-0, KamLAND-Zen and EX0-200. These experiments search the $0\nu\beta\beta$ decay by the following reactions:

- $^{76}\text{Ge} \rightarrow ^{76}\text{Se} + (2e^-)$ ($Q_{\beta\beta} = 2039$ keV) [63];
- $^{130}\text{Te} \rightarrow ^{130}\text{Xe} + (2e^-)$ ($Q_{\beta\beta} = 2527$ keV) [64];
- $^{136}\text{Xe} \rightarrow ^{136}\text{Ba} + (2e^-)$ ($Q_{\beta\beta} = 2457$ keV) [65];

The GERDA (GErmanium Detector Array) experiment is situated at Laboratori Nazionali del Gran Sasso, Italy. GERDA consists of high purity germanium detectors (HPGe) enriched to $\sim 86\%$ in ^{76}Ge, immersed in liquid Argon, which acts as cooling system and as shield against external background. The cryostat is installed in the center of a tank filled with 590 m^3 of ultra-pure water equipped with 66 PMTs as muon veto. The physics program of GERDA is divided in two stages. The phase-I has been operating between 2011-2013 with 20 kg of enriched semi-coaxial detectors [66]. Thanks to the shielding and the pulse shape discrimination, the level of background reached in the region of $Q_{\beta\beta}$ is $10^{-2} counts/(keV \cdot kg \cdot yr)$. During this first phase, the lower limit on the half-life of the reaction is $T^{0\nu}_{1/2} > 2.1 \times 10^{25} yr$. The Phase-II started in December 2015. The physics goals are a background level of $10^{-3} counts/(keV \cdot kg \cdot yr)$ and a sensitivity of $10^{26} yr$ for three years of data collection. In this second phase, 30 enriched BEGe detectors [67] are added for a total mass of 35 kg. The preliminary results of phase-II show an improvement of background reduction: $35^{+21}_{-15} \times 10^{-4} counts/(keV \cdot kg \cdot yr)$ for the coaxial detector and $7^{+11}_{-5} \times 10^{-4} counts/(keV \cdot kg \cdot yr)$ for the BEGe. The energy resolution is 4 keV FWHM for coaxial detector and 3 keV FWHM for BEGe. This is the best energy resolution reached in the search for double

beta decay. The $0\nu\beta\beta$ signal has not been observed and the lower limit on $T^{0\nu}_{1/2}$ is $5.2 \times 10^{25} yr$ at 90% C.L. [68].

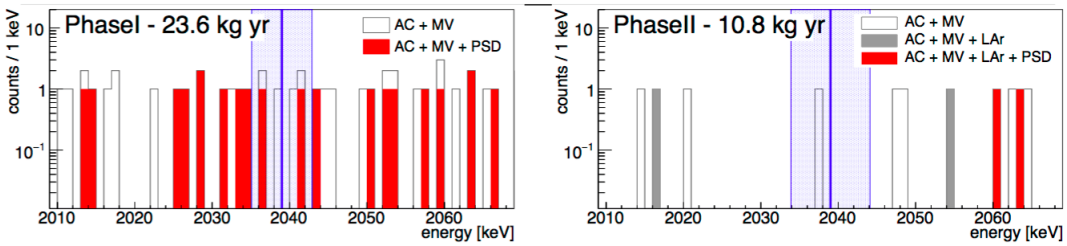

Figure 2.10: GERDA phase-I results on the right, GERDA phase-II result on the left [68].

KamLAND-Zen (KamLAND Zero-Neutrino Double Beta Decay) is a modification of the existing KamLAND detector, used to study neutrino oscillation. KamLAND-Zen consists of 320 kg of ^{136}Xe enriched xenon gas dissolved in 13 tonnes of liquid scintillator (Xe-LS) contained in a spherical balloon (IB) suspended at the center of the KamLAND detector. The IB is constructed from 25-μm-thick transparent nylon film and it is surrounded by 1 ktonne of liquid scintillator (LS), which acts as active shield. The isotopic abundances in the enriched xenon were measured by a residual gas analyzer to be $(90.77 \pm 0.08)\%^{136}$Xe and $(8.96 \pm 0.02)\%^{134}$Xe while other xenon isotopes have negligible presence. The data-taking of KamLAND-Zen started in 2011 and the physics program is divided in two phases. In the first phase (September 2011 - June 2012) the limit on half-life is $T^{0\nu}_{1/2} > 1.9 \times 10^{25} yr$ at 90% C.L.. The sensitivity was limited by an unspected background peak, due to the ^{110m}Ag β^- decay, just above the Q-value of ^{136}Xe. The Xe and Xe-LS was purified to reduce this source of background. The Phase-II started in December 2013 and finished in October 2015. Thanks to the Xenon purification, the background produced by $^{110m}Ag\beta^-$ decay was reduced by a factor of ten. The lower limit on $T^{0\nu}_{1/2}$ is upper $1.3 \times 10^{25} yr$ on 90% C.L., combing the Phase-I and Phase-II results: $T^{0\nu}_{1/2} > 1.07 \times 10^{25} yr$ [69].
EX0-200 (Enriched Xenon Observatory) is a cylindrical liquid xenon (LXe) time projection chamber (TPC), located underground at depth of $1,585^{+11}_{-6}$ meter water equivalent at the Waste Isolation Pilot Plant, New Mexico. The liquefied xenon (^{enr}LXe) is enriched to 80.6% in ^{136}Xe. The TPC provides position and energy measurements of ionization deposits in the LXe by simultaneously collecting the scintillation light and the charge. Avalanche photodiodes (APDs) measure the scintillation light. The principal sources of background are given by uranium/thorium contamination and ^{137}Xe. The lower limit on $T^{0\nu}_{1/2}$ is $1.1 \times 10^{25} yr$ at 90% C.L. [70], obtained by the data collected between 2011 and 2013.
The search of neutrinoless double beta decay by CUORE-0/CUORE will be

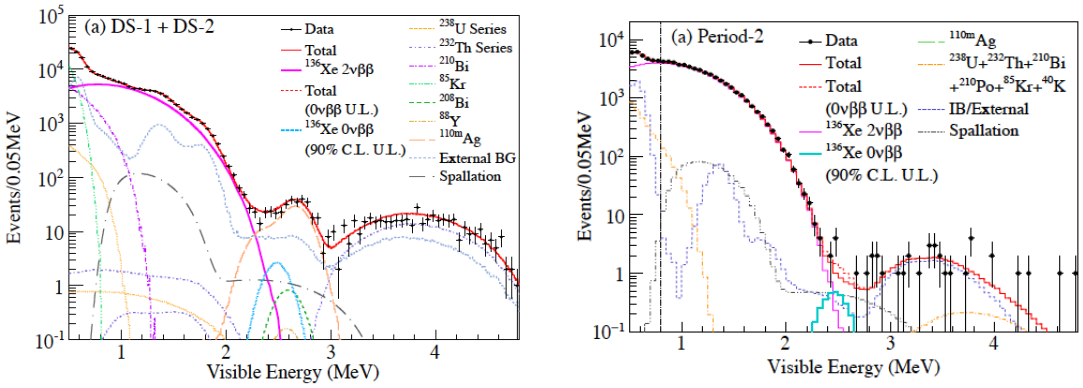

Figure 2.11: Energy spectrum for $\beta\beta$ candidates obtained during phase-I (right) and phase-II (left) by KamLAND-Zen [69].

discussed in the next chapter.

2.4.1 Limit on effective Majorana mass

The effective Majorana mass can be expressed as a function of the sensitivity by following relation:

$$m_{\beta\beta} = \frac{m_e}{M^{0\nu}\sqrt{G^{0\nu} S^{0\nu}_{1/2}}}. \tag{2.14}$$

Given the sensitivity reached by germanium and xenon experiments, the limit on effective Majorana mass are:

- GERDA phase-II: $m_{\beta\beta} < [160, 260]$ meV,
- EX0-200: $m_{\beta\beta} < [190, 450]$ meV,
- KamLAND-Zen phase-II : $m_{\beta\beta} < [61, 165]$ meV,

The limits on effective Majorana mass are estimated for the minimum and maximum value of $M^{0\nu}$. The nuclear matrix element is estimated by QRPA model for the ^{136}Xe, instead it is estimated by ISM model for the ^{76}Ge.
The most stringent limit on effective Majorana mass is obtained by KamLAND-Zen (see fig. 2.12).

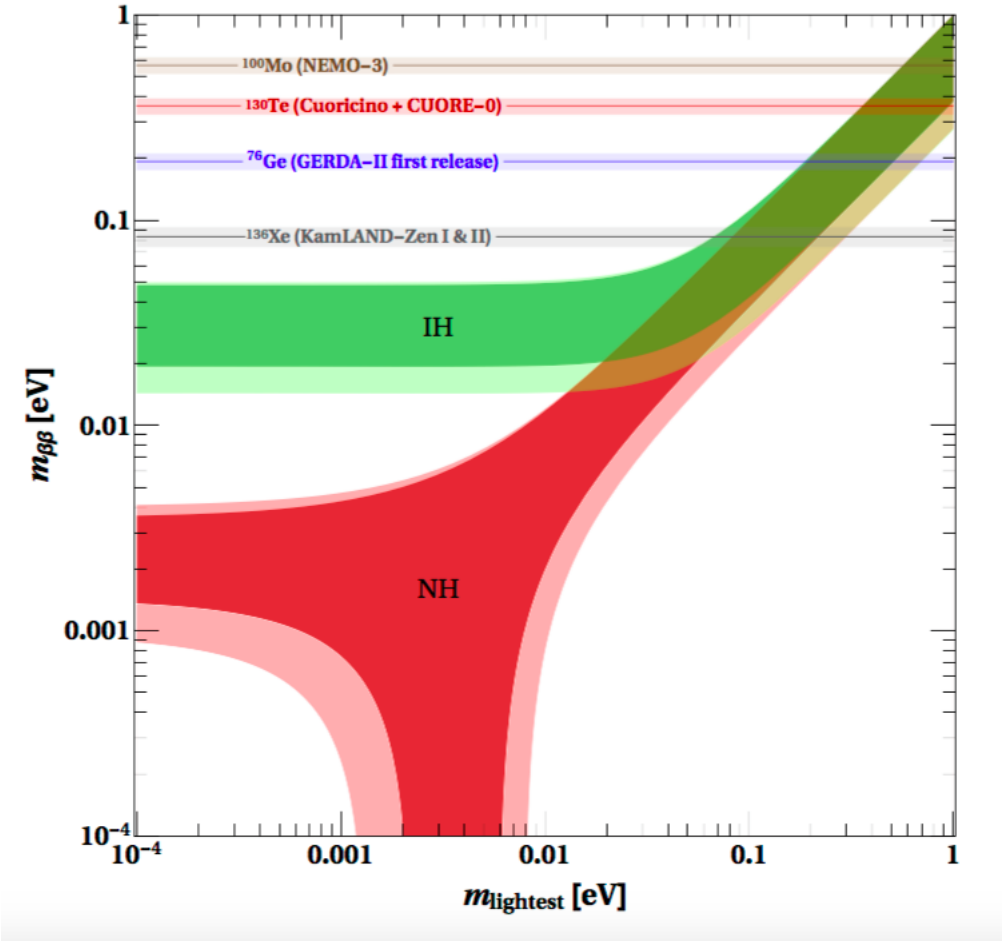

Figure 2.12: Present limit on effective Majorana mass [71].

2.4.2 Towards Inverted Hierarchy: future detectors

The goal of the next generation DBD experiment is to investigate the IH region. To this goal the germanium experiments need a sensitivity on $T^{0\nu}_{1/2}$ of $\sim 4 \times 10^{28} yr$ (see fig. 2.13), while the xenon experiments of $\sim 9 \times 10^{27} yr$ (see fig. 2.14).

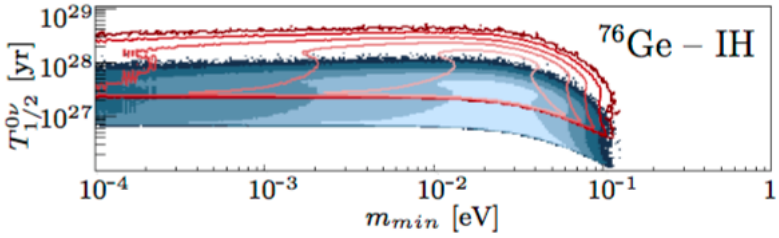

Figure 2.13: $0\nu\beta\beta$ decay half-life for ^{76}Ge as a function of the lightest neutrino mass. The blue region is obtained with $|M^{0\nu}| = 5.16$ and the red region with $|M^{0\nu}| = 2.81$ [72].

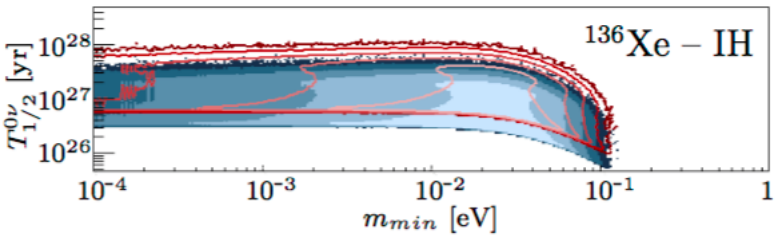

Figure 2.14: $0\nu\beta\beta$ decay half-life for ^{136}Xe in function of the lightest neutrino mass. The blue region is obtained with $|M^{0\nu}| = 3.05$ and the red region with $|M^{0\nu}| = 2.18$ [72].

The upcoming HPGe detector is the MAJORANA experiment, which will be situated in the Sanford Underground Laboratory, USA. The DEMONSTRATOR [73], is a MAJORANA prototype developed to define the best technique to build a large scale germanium experiment. The MAJORANA-DEMONSTRATOR consists of a mixture of BEGe detectors including, 15 kg fabricated from natural-isotopic-abundance Ge and 29.7 kg fabricated from Ge enriched to $> 87\%$ in ^{76}Ge. These detectors are contained within two low-background copper cryostats. Each cryostat will contain seven closely-packed stacks of detectors, called strings, with up to five detectors comprising each string. The goal of the DEMONSTRATOR is to achieved background level at or below of 3 $counts/(keV \cdot kg \cdot yr)$ in a 4 keV interval around the region of interest. The MAJORANA-DEMONSTRATOR and

the GERDA collaboration intent to merge and purse a joint tonne-scale $0\nu\beta\beta$ experiment that combines the best technology from both collaborations.
nEXO [74] and NEXT [75] are the upcoming detectors that search $0\nu\beta\beta$ decay with ^{130}Xe. nEXO is the next_phase of EXO experiment. The principal modifications of EXO detector include improved self-shielding with the larger mass, a better energy resolution using lower noise silicon phomultipliers, increased segmentation to improve event reconstruction. The nEXO goal sensitivity is 6.6×10^{27} yr at 90% C.L. using 5 tonnes of enriched xenon after five years of data-taking. The NEXT (Neutrino Experiment with a Xenon TPC) experiment uses enriched Xenon in a high pressure (15 bar) TPC. It is designed to have high energy resolution of 0.3% at Q-value and to have a high discrimination power between signal (two electron tracks with a common vertex) and background (mostly, single electrons or alphas). The goal is to reach a level of background of $8 \cdot 10^{-4} counts/(keV \cdot kg \cdot yr)$.
SNO+ detector [76] is an upgrade of SNO experiment to search the neutrinoless double beta decay of ^{130}Te. The technique is similar to KamLAND-Zen: tellurium dissolved in a liquid scintilllator (Te-LS), which replaced the pure heavy water used in SNO. An innovative technique has been developed to load tellurium at concentration levels of several percent into LS maintaining good optical properties and reasonably high light yield.
In table 2.5 the sensitivity for upcoming and future detectors are listed.

Experiment	Isotope	$S^{0\nu}_{1/2}$[yr]	Reference
GERDA-II	^{76}Ge	1.5×10^{26}	[77]
MAJORANA-D	^{76}Ge	3.0×10^{25}	[78]
CUPID-0	^{82}Se	1.8×10^{25}	[79]
SuperNEMO	^{82}Se	1.0×10^{26}	[80]
AMoRE-II	^{100}Mo	1.1×10^{27}	[81]
CUORE	^{130}Te	9.5×10^{26}	[82]
SNO+ Phase II	^{130}Te	2.0×10^{26}	[83]
EXO-200	^{136}Xe	5.7×10^{25}	[74]
KamLAND2-Zen	^{136}Xe	1.0×10^{27}	[69]
nEXO	^{136}Xe	5.0×10^{27}	[84]
NEXT-100	^{136}Xe	6.0×10^{25}	[85]
PandaX-III	^{136}Xe	1.0×10^{26}	[86]

Table 2.4: Upcoming and future DBD detectors sensitivity.

Chapter 3

CUORE

3.1 CUORE: ^{130}Te $0\nu\beta\beta$ search

CUORE (Cryogenic Underground Observatory for Rare Events), situated at Laboratori Nazionali del Gran Sasso, is a starting 1-tonne experiment which searches the $0\nu\beta\beta$ decay of ^{130}Te using the bolometric technique. A bolometer is a Low Temperature Detector (LTD) in which the energy of the incident particle is converted in thermal phonons. The bolometric technique was first proposed by Simon for the study of nuclear phenomena [87]. In 1949 Andrews detected for the first time alpha particles using superconductive bolometers [88]. Then thermal detectors were developed for different topic of research, as solar neutrino spectroscopy, X ray spectroscopy, material contamination analysis, dark matter detection and rare processes search. The use of large bolometric detectors was first proposed by Fiorini and Niinikoski in 1983 [89]. The bolometric technique will be discussed in same detail in the next chapter.
CUORE [90] consists in 988 TeO_2 crystals arranged in a modular structure in 19 towers. Each tower is an array of 52 TeO_2 crystals, disposed in 13 floors, on each floor there are four $(5 \times 5 \times 5)$ cm^3 crystals with a mass of 750 g. The total mass of CUORE is 741 kg. In figure 3.1 the CUORE towers are shown.

CUORE bolometers will be operated at $\sim$10 mK temperature. The expected energy resolution is 5 keV at 2615 keV peak and the expected background level is 10^{-2} $counts/(keV \cdot kg \cdot yr)$ in the energy region around the Q-value of ^{130}Te (Region of Interest-ROI[1]).
CUORE searches for neutrinoless double beta decay by the following reaction:

$$^{130}Te \rightarrow^{130} Xe + 2e^-, \tag{3.1}$$

the Q-value is 2528.8 ± 1.3keV.
The bolometric technique offers a wide choice of isotope candidate, as ^{48}Ca,

[1]The corresponding energy range is 2470-2570 keV.

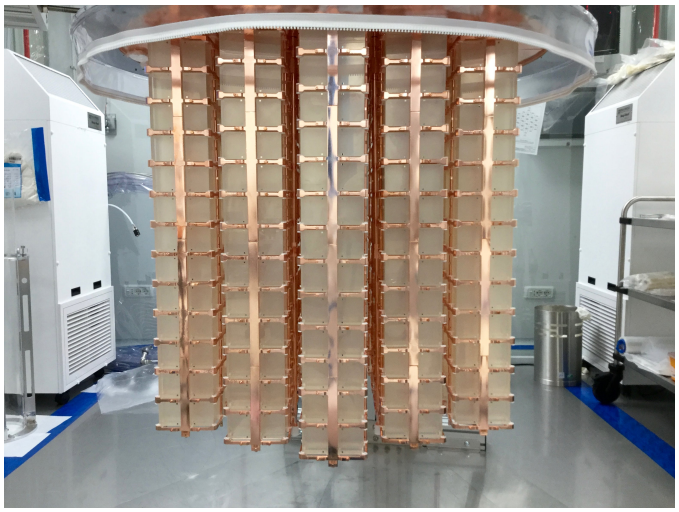

Figure 3.1: CUORE towers.

^{76}Ge, ^{100}Mo, ^{116}Cd, the only requirement being that the candidate nucleus be part of a compound which can be grown in the form of a crystal with good thermal and mechanical properties.
The ^{130}Te Q-value is between the Compton edge and the ^{208}Tl peak, which is the highest line of natural radioactivity. There are several isotopes that have a Q-value above the 2615 keV peak but they have a low isotopic abundance and therefore require an enrichment. On the contrary, the ^{130}Te has a natural isotopic abundance of 34%, so enrichment is not mandatory (fig. 3.2). This is a great advantage because the enrichment process can introduce crystal contaminations and is an expensive process.
The Q-value of ^{130}Te is high enough to have a favorable space factor[2]($G^{0\nu}$), that is $14.58 \cdot 10^{-15}$ [52].
As it was discussed in the previous chapter, the estimation of the nuclear matrix elements is the principal source of uncertainty and its evaluation depends on the different isotope. In the case of ^{130}Te NME varies between [91]:

- smallest value: $|M^{0\nu}| = 2.18$ estimated by QRPA models;
- largest value: $|M^{0\nu}| = 3.05$ estimated by IBM;

Given the value of $G^{0\nu}$ and the range of NME, the needed sensitivity on $T^{0\nu}_{1/2}$ to investigate the IH is of order of $9 \times 10^{27} yr$ and it is of order of $6 \times 10^{30} yr$ to investigate the NH for the ^{130}Te case [72]. This estimation is obtained by formula 2.4 and using the cosmological bound. Figure 3.3 shows the half-life of $0\nu\beta\beta$ for ^{130}Te as a function of lightest neutrino: the red regions are obtained with the smallest value of $|M^{0\nu}|$ and the blue regions with the largest value of $|M^{0\nu}|$.

[2]As it was discussed in paragraph 2.1.2: the $G^{0\nu}$ is proportional to $Q^5_{\beta\beta}$.

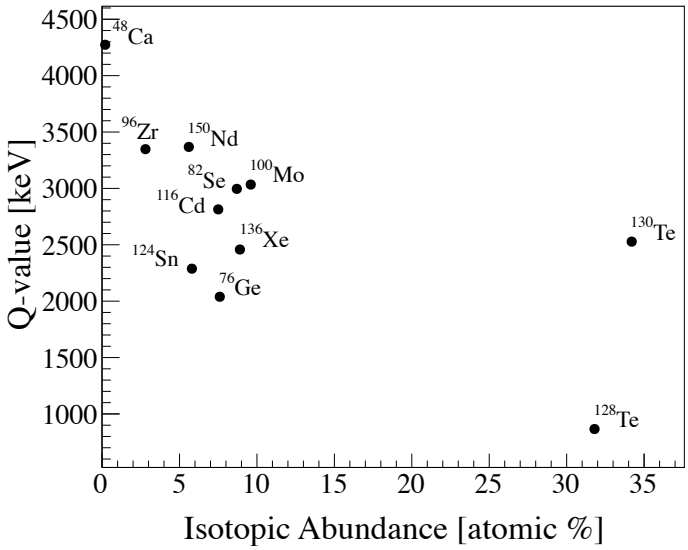

Figure 3.2: Natural abundances and Q-values for several commonly used $0\nu\beta\beta$ isotopes.

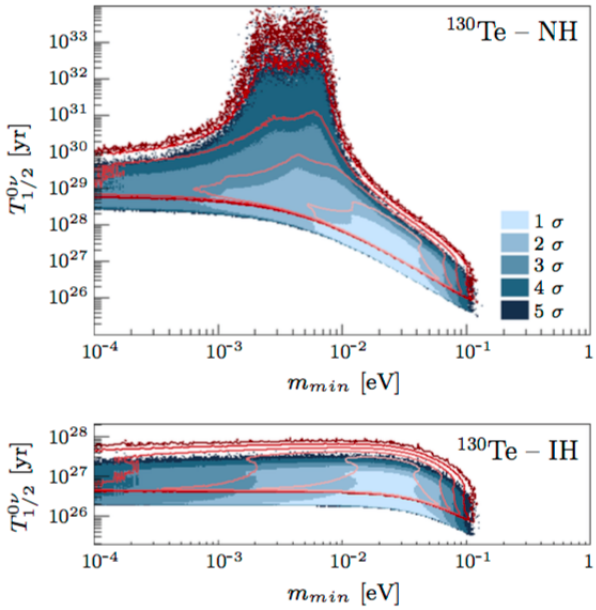

Figure 3.3: $0\nu\beta\beta$ decay half life for ^{130}Te as a function of the lightest neutrino mass with the application of the cosmological bound. The blue regions are obtained with $|M^{0\nu}| = 3.05$, the red curves with $|M^{0\nu}| = 2.18$. The different color shadings correspond to the 1, . . . , 5 σ coverage regions [72].

3.2 Cryogenic system and shielding

CUORE towers are housed in a dedicated custom-built cryogens-free dilution refrigerator. It is planned to cool a large mass at 10 mK in stable condition for a long period of data-taking [92]. Due to the severe radioactivity constraints, CUORE cryostat has to satisfy several additional requirements which are rather uncommon in standard cryogenic devices.
The cryogenic system must satisfy the following requirements:

- the cooling power of the refrigerator has to account for the thermal load produced by the ∼2600 read-out wires running from 10 mK to room temperature;
- the detector and the cryogenic system have to be mechanically decoupled to minimize the noise induced by cryostat vibrations;
- the cryostat components have to fulfill stringent radio-purity control and a shielding has to be used to reduce the background coming from ^{232}Th and ^{238}U chains in the surrounding;
- since CUORE is expected to collected data for a period of five years, the cryogenic system must be stable, service-free and capable to operate with high duty-cycle.

CUORE cryostat consists of six copper vessels thermalized to different temperature stages: 300 K, 40 K, 4 K, 600 mK (still plate), 50 mK and 10 mK (mixing chamber plate). A schematic view of the cryostat is shown in figure 3.4. The 40 K stage is an intermediate radiation shield between the room temperature Outer Vacuum Chamber (OVC) and the Inner Vacuum Chamber (IVC) thermalized to 4K. The 40 K and 4 K vessels are wrapped by Multi-Layer Insulation (MLI) to reduce the heating from thermal radiation. The amount of MLI is limited by radioactivity constraints.
The copper is chosen in order to preserve the radio-purity requirement in the rare event search. In order to satisfy the CUORE background goal the levels of ^{232}Th and ^{238}U must be $< 2 \cdot 10^{-6}$ Bq/kg and 10^{-4} Bq/kg respectively. The copper vessels were properly cleaned by citric acid and hydrogen peroxide solution to remove the possible contamination introduced on the surfaces during manufacturing.
In addition, inside the cryostat there are two lead shieldings that improve the detector protection from environmental radioactivity and from contaminations present on the outer layers of the cryostat itself. A 2.5 tonnes lead shield (see fig. 3.5) is present above the tower support plate (TSP) and is thermalized to 50 mK (Top Lead Shield in figure 3.7); a 4.5 tonnes shield made of ancient roman lead (see fig. 3.6) is placed between the 4K and the 600 mK vessels and it is thermalized to 4 K (Ancient Roman lead in figure 3.7). The complete cryogenic structure is shielded by an external

modern lead shield.

The CUORE cryogenic system is a dilution unit refrigerator, pulse-tube assisted:

1. the temperature of 4 K is reached by five two-stage pulse tubes (PT) coolers mounted on the room temperature OVC top flange. The total cooling power of the pulse-tubes is 200 W at 40 K and 7.5 W at 4 K.

2. the base temperature is reached by ^{3}He/^{4}He dilution unit custom designed by Leiden Cryogenics. It is capable to circulate more than 8 mmol/s of ^{3}He/^{4}He mixture in order to guarantee high cooling power, that is 2 mW at 100 mK and 4μW at 10 mK.

The choice of PT arise from the fact that, unlike conventional cryogen based dilution units, the PT based dilution refrigerators do not require frequent interruption for refilling the cryogen, increasing then the duty cycle of the experiments.
The CUORE cryostat makes use of an auxiliary sub-system, called the fast cooling system (FCS), to speed-up the cooling down from room temperature to 4 K. The FCS employs a closed cycle to have forced convection of cold gas in the IVC. The total mass to be cooled to 4 K is about 15 tonnes. The pulse tubes alone would take few months to cool down this mass, instead with the FCS the cool down period is reduced to two weeks.
The detector and the cryogenic system are mechanically decoupled to minimize the noise produced by external vibration which would spoil the energy resolution of the detector. The CUORE detector suspension is a two-stages low frequency isolation system (see fig. 3.8). The first section of the suspension operates at room temperature and consists of three $Minus-K$ springs, placed on the Main Support Plate (MSP). In a $Minus-K$ [93] spring the vertical motion isolation is provided by a stiff spring that supports the weight load (the $Y-beam$ mass and the detector mass), combined with a negative−stiffness mechanism. The net vertical stiffness is made very low without affecting the static load−supporting capability of the spring. Beam columns connected in series with the vertical-motion isolator provide also horizontal motion isolation. The net result is a compact passive isolator capable of very low vertical and horizontal natural frequencies and very high internal structural frequencies. The second section is the cryogenic suspension system, made out of three composite cables, directly connected to the $Y-beam$, which support the whole detector mass, bypassing the different cryogenic shields. The material of the CUORE suspension must have high tensile proprieties, low thermal conductivity and low radioactive contamination, so the chosen materials are stainless steel tie bars, Kevlar 49 ropes and copper bars [94].

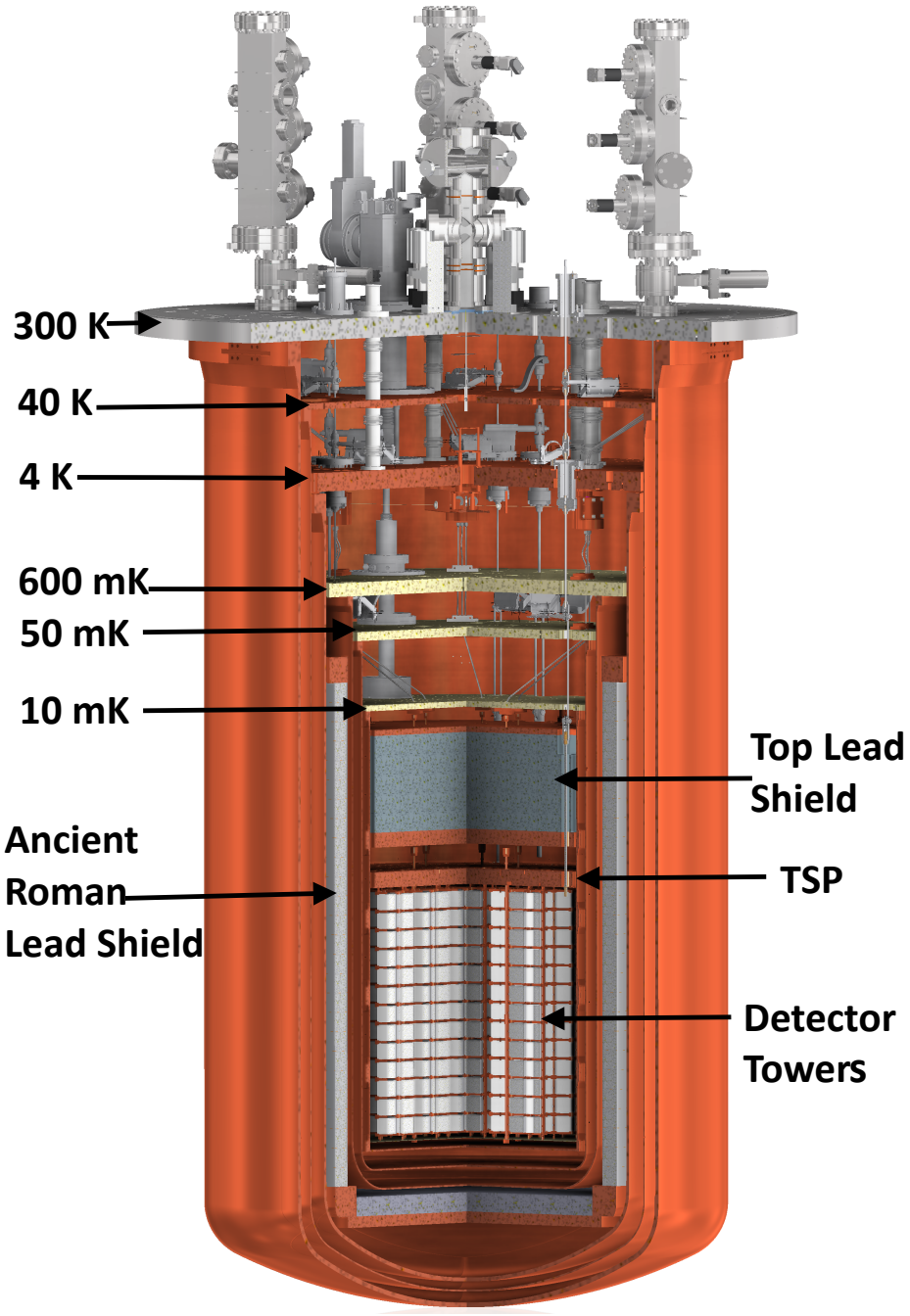

Figure 3.4: A complete schematic of the CUORE cryostat.

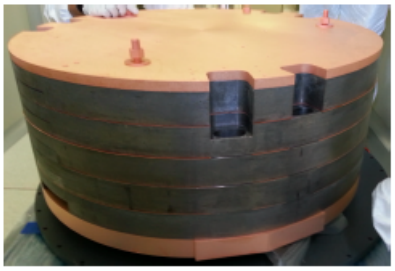

Figure 3.5: Modern top lead shield.

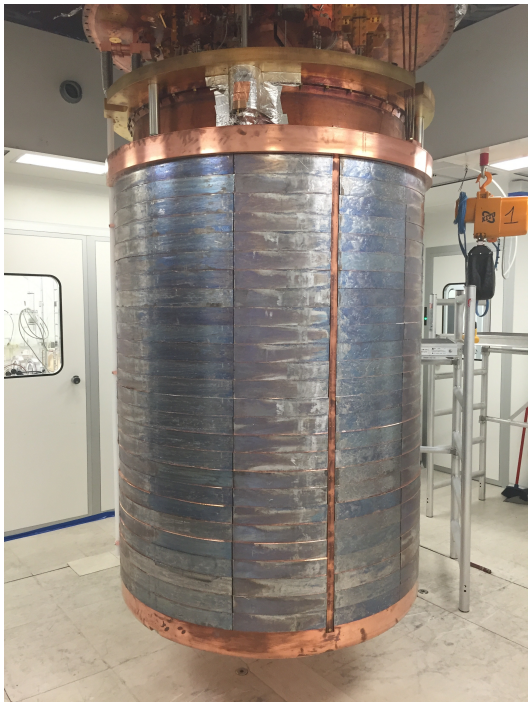

Figure 3.6: Ancient roman lead shield.

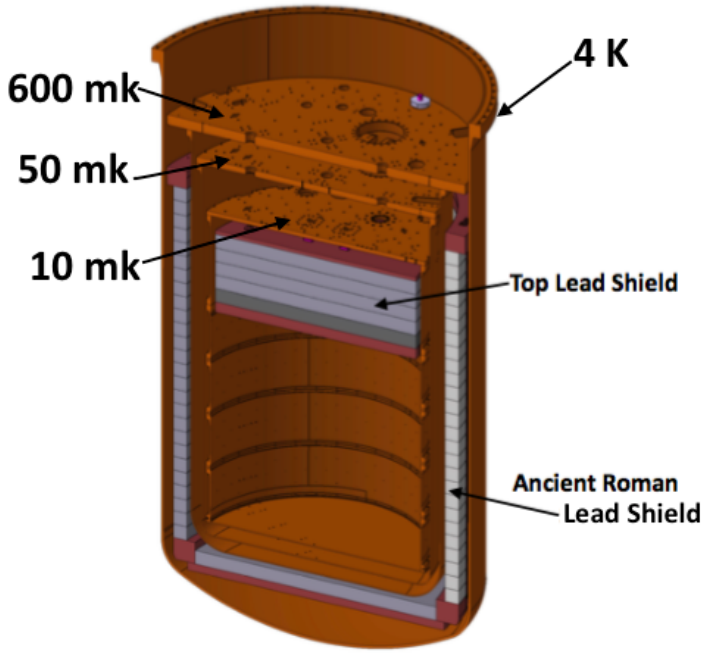

Figure 3.7: Schematic of CUORE shielding.

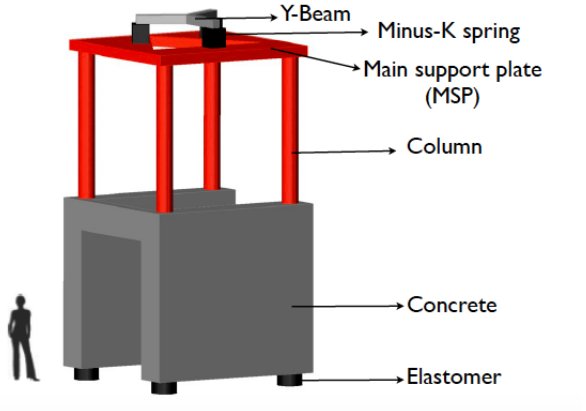

Figure 3.8: Sketch of the detector support layout: there are the column supports and the main support plate (MSP). On the MSP are placed the three Minus−K spring and the "Y−beam".

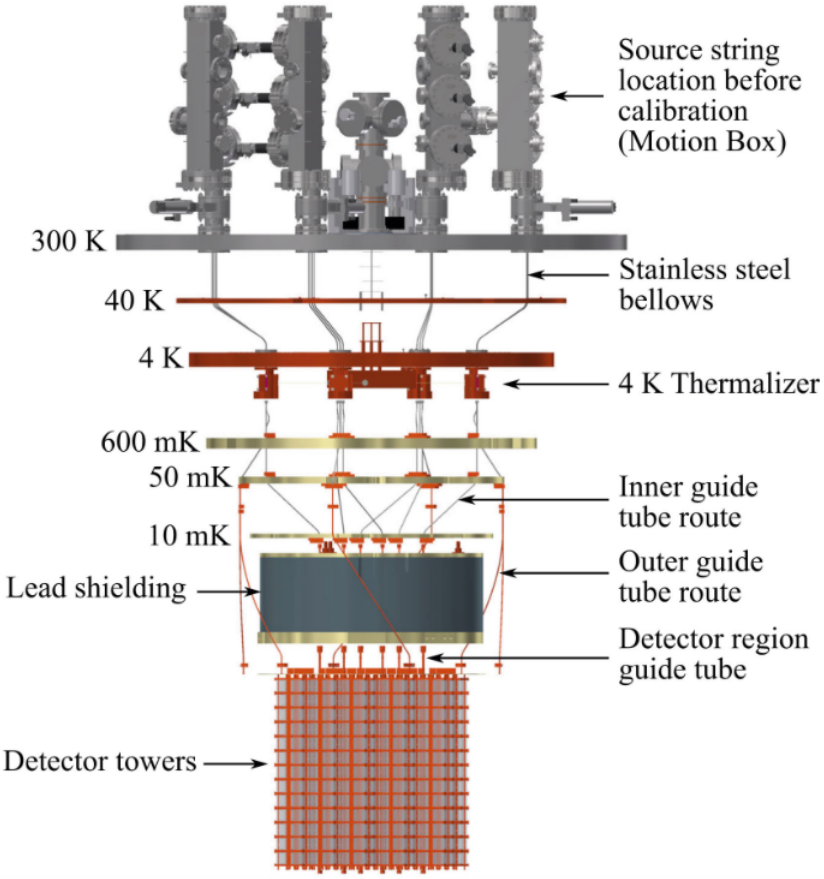

Figure 3.9: The detector calibration system (DCS): 12 Kevlar strings and 25 Teflon − coated copper capsules per string connected to a motor head on the top of the cryostat [95].

The detector calibration system (DCS) [95] consists of 12 Kevlar strings and 25 Teflon-coated copper capsules per string, which contain small thoriated tungsten wire. Each source string is wound on a spool that is connected to a motor on the top of the cryostat, which turns the spool to raise and lower the source string. The source strings are first cooled to 4K by mechanical squeezing before being lowered further into the cryostat (see fig. 3.9).

Before the detector installation, there where several cold runs to test the Dilution Unit (DU) performance and to study the thermal load introduced by the different components (wiring, shielding, DCS, FCS, ...). In the last cold run, with full load except the detector, the system reached a base temperature of (6.3±0.04) mK in stable condition. The cool down with the FCS was successfully tested, the 4 K temperature was reached in 16 days. The subsequent cool down from 4K to base temperature took about 24 hrs [96].

3.3 CUORE-0: the first tower

CUORE-0 is an array of 52 TeO_2 crystals disposed in the CUORE tower style. The total mass is 39 kg of TeO_2.
CUORE-0 is the first tower produced using the low-background assembly line designed for CUORE in order to minimize the radioactive contamination of detector components and radon contamination. The CUORE assembly line is based on strict selection of materials and an extreme radio-purity control during the assembly process [97].
The assembly is done following a "zero contact" philosophy for the detector components, i.e. no exposure to air to prevent possible radon contamination and minimized contact (in space and time) with other materials. The assembly procedure consists of two principal steps. In the first step the thermal sensor, used to convert the temperature variation in electrical signal, is glued to the crystal. The second step is the tower assembly. These two procedures used two specific glove boxes under nitrogen atmosphere to minimize radon contamination. In figure 3.10 the two glove boxes are shown: gluing box on the left and tower glove box on the right.
All copper parts of detector (frame, columns, ecc..) are cleaned by TECM

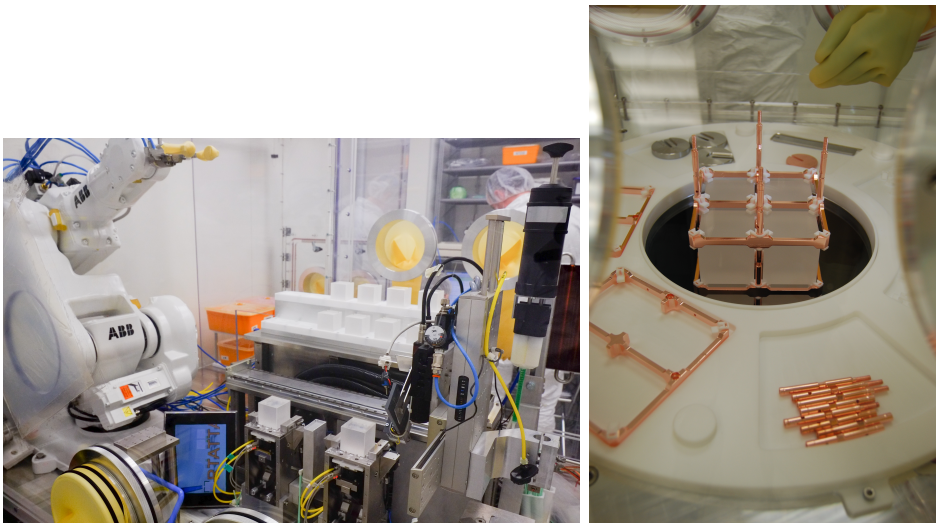

Figure 3.10: On the left the gluing glove box used for sensor-crystal coupling. It is a semi-automatic system designed to guarantee a good reproducibility of the coupling. On the right the tower glove box used for tower assembly. Both glove boxes are under nitrogen flow to protect the detector from radon contamination.

technique for radio-purity requirements. The TECM cleaning consists in a sequence of different step of surface treatments: tumbling, electopolishing, chemical etching and magnetron plasma cleaning. Moreover, to reduce the

cosmogenic activation, the exposure of detector parts to cosmic rays is minimized. The detectors parts, after having been produced, are packed and then stored in the underground laboratories, inside stainless-steel cabinets, which are continuously flushed with nitrogen.
Differently than the CUORE towers, CUORE-0 was surrounded by a lateral copper shield (see fig. 3.11) and it was cooled by a commercial cryostat. The tower was also shielded by 1.4 cm of cylinder of Roman lead and two discs of roman lead placed one on the top and one the bottom against the intrinsic radioactivity of the cryogenic system. The cryostat is shielded by modern lead, that is surrounded by a anti-radon box flushed with nitrogen gas to reduce radon contamination. The entire apparatus was enclosed in a Faraday cage to minimize electromagnetic interference (see fig. 3.11).

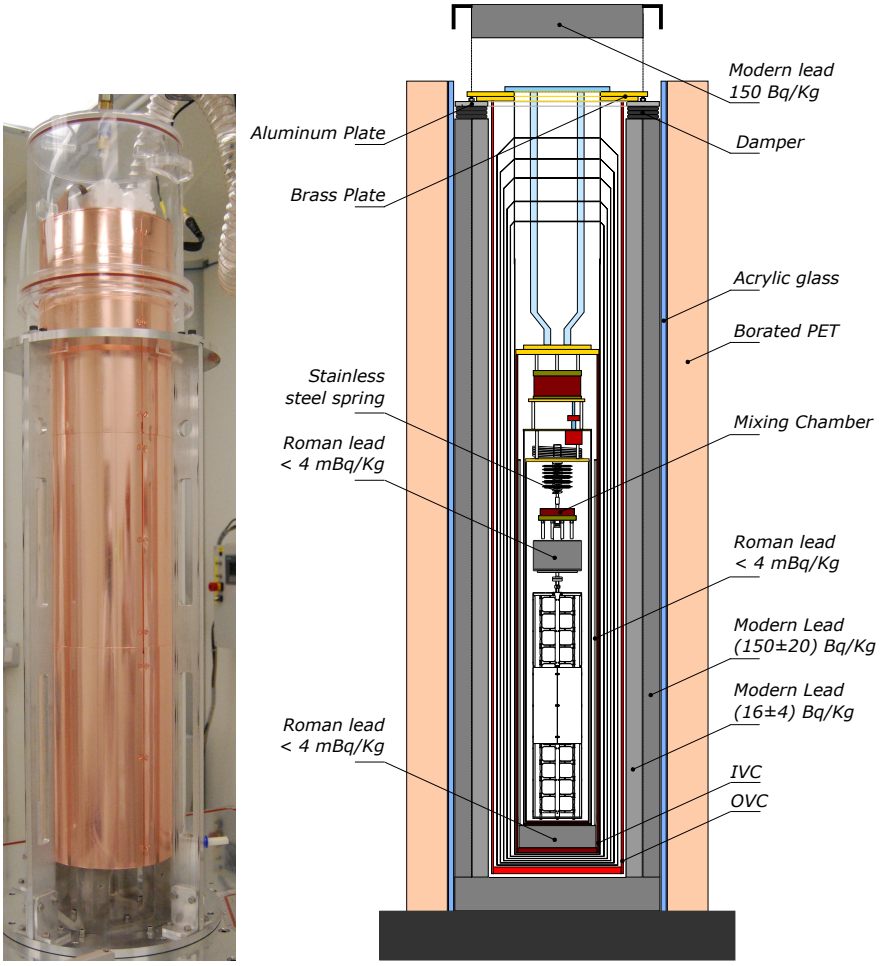

Figure 3.11: On the left the CUORE-0 copper shield under nitrogen flow. On the right a sketch of CUORE-0 cryostat and shielding [97].

CUORE-0 was operated between 2013 and 2015 as CUORE prototype in order to:

- test the validity of bolometric technique for $0\nu\beta\beta$ search;
- test the CUORE DAQ and analysis framework;
- test and debug the CUORE tower assembly line;
- check the background reduction thanks to the assembly line designed for CUORE towers.

3.3.1 Alpha background reduction

In CUORE, the dominant background is originated by α particles, emitted from radioactive nuclei located within few μm of a surface facing the detector, that lose part of their energy in this dead layer before reaching the detector. The result is a flat continuous energy spectrum from 4-5 MeV to zero.
In the past years different CUORE prototypes were built in order to characterize and optimize the CUORE α background.
Before CUORE-0, the CUORICINO experiment [98], was operated between 2003 and 2008 to study the background of the CUORE bolometers. CUORICINO was a single tower of 62 TeO_2 crystals with a CUORE tower like design. CUORICINO demonstrated that the dominant background in the CUORE-like bolometers is given by α contamination of copper, so the new assembly line was developed and its efficacy was tested by CUORE-0.
In figure 3.12 the background energy spectra obtained by CUORICINO (black) and CUORE-0 (red) are shown. The background sources can be distinguished in two different components:

- *gamma background*: multi Compton event originated from the 2615 keV peak due to a ^{232}Th contamination of the cryostat itself;
- *alpha background*: ^{232}Th and ^{238}U contaminations that come from surface contamination of crystal and copper frame.

Since CUORE-0 and CUORICINO were operated in the same cryostat, the gamma contribution is almost the same. This contribution is expected to be reduced in CUORE thanks to the better shielding and the radio-purity control on the cryogenic system components, strictly selected to minimize the level of contamination. Moreover, all the CUORE copper vessels were properly cleaned before the installation of the detector.
The α contribution was a dominant background component in CUORICINO, whereas it is a sub-dominant component of the background in the ROI in CUORE-0. Indeed, the background rate measured in the alpha region $(2.7 - 3.9$ MeV) is 0.016 ± 0.001 $counts/(keV \cdot kg \cdot yr)$ in CUORE-0,

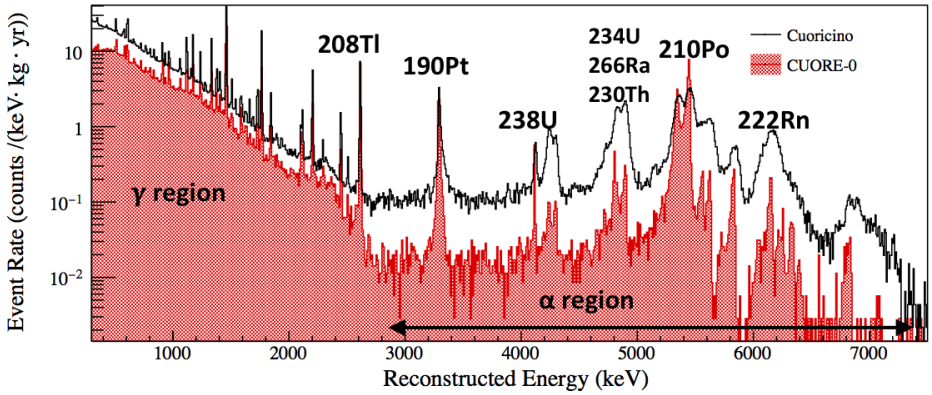

Figure 3.12: CUORE-0 (red) and CUORICINO (black) background energy spectra. The gamma component is almost the same because both experiments were operated in the same cryostat. The alpha component is reduced in CUORE-0 thanks to the new assembly line and the cleaning protocols. The ^{190}Pt peak is a bulk contamination and does not affect the background in the ROI.

while was a factor of 7 higher in CUORICINO, that is
0.110 ± 0.001 $counts/(keV \cdot kg \cdot yr)$ [97]. In this estimate, the ^{190}Pt peak, centered at 3249 keV, was excluded because platinum is a bulk contamination of ^{130}Te crystal and it does not affect the CUORE background in the ROI.
In the ROI, the total background rate measured by CUORE-0 is
$0.058 \pm 0.004(stat) \pm 0.002(syst)$ $counts/(keV \cdot kg \cdot yr)$, corresponding to a factor 3 reduction respect to CUORICINO, where the rate was
0.169 ± 0.006 $counts/(keV \cdot kg \cdot yr)$ [97].

3.3.2 Projected CUORE background

The study of CUORE-0 background demonstrated the efficacy of CUORE assembly line and cleaning protocols to reduce the α contamination of the copper structure.
A detailed Monte Carlo simulation was performed to evaluate the expected background in CUORE, based on the CUORE-0 results and on the knowledge of background sources.
The CUORE background sources can be classified according to the originating region in:

- *external region*: γ, neutrons and muons fluxes; the latter is reduced by 3400 m.w.e. rock;
- *far region*: radioactive contamination of Roman lead, modern lead, superinsulation, stainless steel rods, stainless steel 300 K plate;

Region	Source	Bkg rate$[counts/(keV \cdot kg \cdot yr)]$
External	γ flux	$< 3.9 \cdot 10^{-4}$
	n flux	$8 \cdot 10^{-6}$
	μ flux	$1.04 \cdot 10^{-4}$
Far	Bulk of Rods and 300 K Flange	$3 \cdot 10^{-5}$
	Bulk of SI	$2.1 \cdot 10^{-6}$
	Bulk of Modern Pb	$< 2.0 \cdot 10^{-4}$
	Bulk of Roman Pb	$3.22 \cdot 10^{-3}$
	Bulk of Copper	$< 1.7 \cdot 10^{-3}$
Near	Cosmogenic activation of TeO_2	$< 7.3 \cdot 10^{-5}$
	Cosmogenic activation of copper	$< 2.4 \cdot 10^{-9}$
	Bulk and surface of copper	$9.50 \cdot 10^{-3}$
	Bulk and surface of TeO_2	$1.30 \cdot 10^{-3}$

Table 3.1: Main contribution expected in the ROI of CUORE for the various components [99]. The value of bulk and surface contamination of copper and TeO_2 are estimated by CUORE-0 results.

- *near region*: bulk and surface contamination of copper and TeO_2 (principally given by ^{238}U and ^{232}Th chains), and cosmogenic activation in copper and TeO_2.

Special care has been put in the reduction of background coming from cosmogenic activation of copper and TeO_2, that produce ^{60}Co and ^{110m}Ag. Indeed their decays affect the ^{130}Te neutrinoless double beta decay ROI. ^{60}Co ($\tau_{1/2} = 5.27yr$, Q = 2.82 MeV) is produced both in copper and TeO_2. It $\beta-$decays mainly with the emission of two γs. To mimic the energy of $0\nu\beta\beta$ event, both γs and electron must deposit the energy in the same crystal, requiring ^{60}Co to be either in the TeO_2 crystal or in the copper parts close to the bolometers. ^{110m}Ag is produced only in the tellurium. It can either $\beta-$decays in the stable isotope ^{110}Cd (Q = 3.01 MeV) or it can make an isomeric transition to ^{110}Ag, which than further $\beta-$decays in ^{110}Cd (Q = 2.89 MeV). Both ^{110m}Ag and ^{110}Ag emit in their decay numerous photons. The decays of ^{110m}Ag and ^{110}Ag can mimic $0\nu\beta\beta$ events when the total energy deposited in a single crystal by the photons and electrons falls within the ROI. As discussed before, copper and TeO_2 were stored underground, after their production, to minimize their exposure to cosmic rays. The background rate estimated by MC simulation for this different components is shown in table 3.1.

In figure 3.13 the main background contributions expected in the ROI of CUORE for the various components are reported. The expected background level in the ROI is of order of $10^{-2} counts/(keV \cdot kg \cdot yr)$.

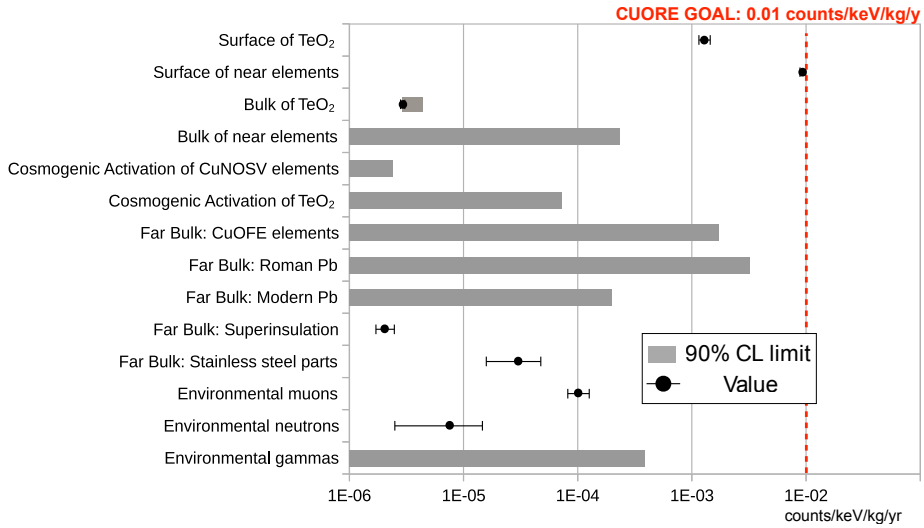

Figure 3.13: The main background contributions expected in the CUORE-ROI.

3.4 Search of $0\nu\beta\beta$ with ^{130}Te

CUORE-0 was also a neutrinoless double beta decay experiment that reached a sensitivity on $T^{0\nu}_{1/2}$ of 2.9×10^{24} yr and set a good limit on the effective Majorana mass $m_{\beta\beta}$.
Figure 3.14 shows the best-fit in the ROI. This energy interval contain 233 candidates in the total exposure of 35.2 $kg \cdot yr$ of TeO_2 or in 9.8 $kg \cdot yr$ of ^{130}Te considering the natural abundance 34.167%. The best-fit gives the following Bayesian lower limit at 90% C.L. [100]:

$$T^{0\nu}_{1/2} > 2.7 \times 10^{27} yr.$$

The limit on $T^{0\nu}_{1/2}$ can be translated in a limit on effective Majorana mass of $270 - 650$ meV. In this estimate the NME elements are calculated by the different models described in [[101], [105]]. Figure 3.15 shows the sensitivity on $m_{\beta\beta}$ reached by CUORE-0 and the expected CUORE sensitivity, that is $9.5 \times 10^{25} yr$ at 90% C.L. [106] for five years of data-taking, given an energy resolution of 5 keV and a background level of $10^{-2} counts/(keV \cdot kg \cdot yr)$. CUORE will be able to investigate a range of $m_{\beta\beta}$ of $40 - 100$ meV, that is near the inverted hierarchy region.

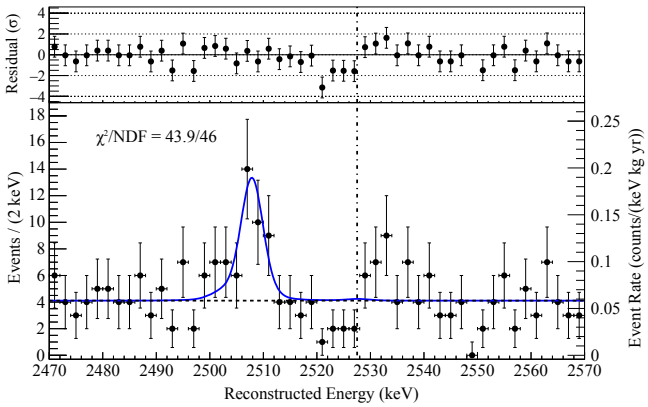

Figure 3.14: Bottom: best fit in the energy region on 2470 −2570 keV. The peak at ∼ 2507 keV is produced by ^{60}Co double-gammas. Top: residuals of the best fit and the binned data [100].

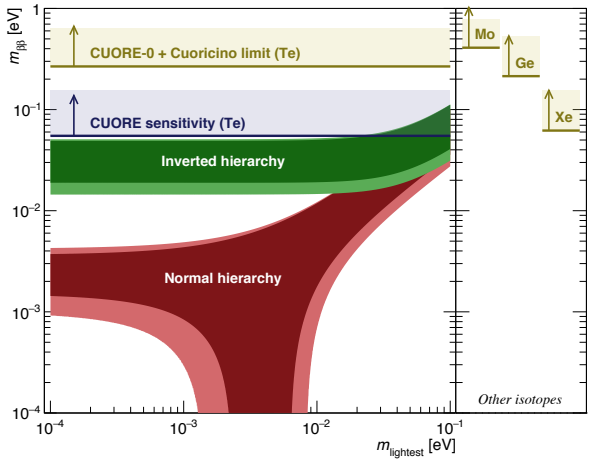

Figure 3.15: CUORE-0 sensitivity and expected CUORE sensitivity on effective Majorana mass as a function of the lighest neutrino mass.

Chapter 4

Bolometric technique

4.1 Bolometer detector

In particle physics most common energy detectors measure the energy released by a particle impinging in the detector converted into ionization and excitation of atoms. In these detectors a large fraction of the released energy is lost as it converts into phonon excitation. This loss worsen the precision with which the energy is reconstructed.
Low temperature detectors measure the deposited energy converted in phonons by means of the corresponding temperature rise. If there is no loss of energy trough competing channels (i.e. scintillation or long lived phonon trapping) all the energy released in the detector is eventually converted into phonons, increasing the precision in the energy reconstruction.
Moreover the fact that the typical energy of the energy carrier in bolometric detectors, namely the phonon, is much smaller that the one of conventional detectors (ionized electron or scintillation light), makes the statistical fluctuation of a given released energy much smaller than in conventional detector, thus the energy reconstruction more accurate.
A bolometer [107] consists of three principal parts: an *absorber*, where the incident particle deposits the energy, a *thermal sensor*, which converts the energy released into the absorber in a electrical signal and a *thermal link* between the absorber and heat sink. A schematic representation of a bolometer is shows in figure 4.1.

Given the simplest bolometer thermal model, in which the thermal conductance (G) is given by the thermal coupling between crystal and heat sink (see fig. 4.2), the temperature variation induced by particle interactions is given by following relation:

$$\Delta T(t) = \frac{\Delta E}{C} exp\left(-\frac{t}{\tau}\right), \tag{4.1}$$

where C is the heat capacity of the crystal, G is the thermal conductance and τ is the decay time of thermal signal ($\tau = \frac{C}{G}$).

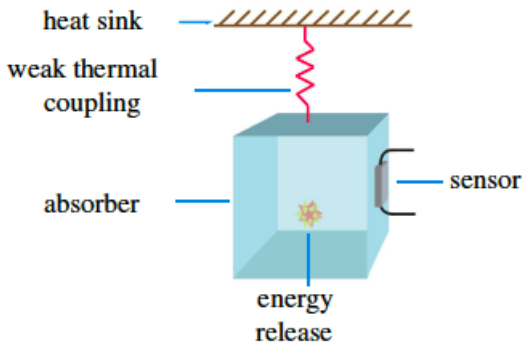

Figure 4.1: Scheme of a bolometric detector.

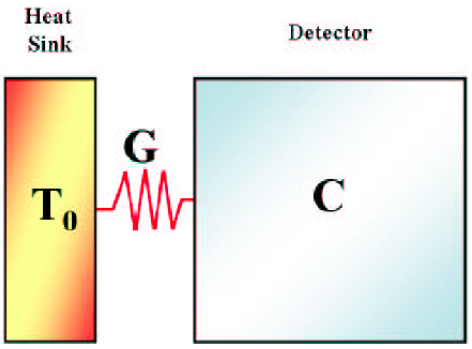

Figure 4.2: The simplest thermal model to describe a bolometric detector.

Since the amplitude of the thermal signal is proportional to the ratio $\frac{\Delta E}{C}$, for a given energy deposition, smaller C means higher thermal signal. A 1 MeV particle impinging on a absorber crystal of 1 mole at room temperature generates a temperature variation ΔT of $10^{-18} - 10^{-15}$ K, which is impossible to measure. Since the heat capacity decreases with the temperature, typical operating temperatures for bolometers are in the range between 10 and 100 mK.

4.2 Energy absorber

The best choice for the energy absorber is a dielectric and diamagnetic crystal, which has a low heat capacity C at low temperature.
The specific heat is given by the sum of lattice contribution c_r and electrons

contribution c_e:

$$c(T) = c_r(T) + c_e(T). \tag{4.2}$$

The lattice contribution is proportional to the cube of temperature over Debye temperature Θ_D:

$$c_r(T) = \frac{12}{5}\pi^4 k_B N_A \left(\frac{T}{\Theta_D}\right)^3, \tag{4.3}$$

where k_B is the Boltzmann constant, N_A is the Avogrado number.
The electrons contribution is proportional to the ratio between temperature and Fermi temperature Θ_F:

$$c_e(T) = \frac{\pi^2}{\Theta_D} ZR \frac{T}{\Theta_F}. \tag{4.4}$$

In a dielectric and diamagnetic crystals, the dominant contribution to the specific heat is given by the lattice contribution. Since this is proportional to T^3, it is very low at low temperature.
The low temperature heat capacity of a dielectric and diamagnetic crystal of mass m can be expressed as:

$$C(T) = \beta \frac{m}{M} \left(\frac{T}{\Theta_D}\right)^3, \tag{4.5}$$

where $\beta = 1944 JK^{-1}mole^{-1}$ and M is the molecular weight.

4.2.1 Thermalization process

The thermalization process, that represents the conversion mechanism of the energy deposited by an interaction into thermal signal, can occur in a bolometer through nuclear and electronic channels [108].
Nuclear channel: particles scattering off nuclei produce vibrational excitations. During the interaction process, structural damages of the lattice could be also produced where the energy can be stored. If this energy is not converted in phonons, the statistical fluctuation of the number of the produced defects can cause a reduction of the detector energy resolution. The fraction of the energy deposited in the nuclear channel depends on the particle incident: it is negligible in case of electrons or photons, but it becomes significant for alpha particle.
Electronic channel: let's take into consideration the kinetic energy transfer from a charged particle produced by a nuclear process to a semiconductor crystal. The particle is slowed down in few μm (heavy particles) or mm (electrons) from its interaction point and normally stops in the crystal. Along its track it produces many electron−hole pairs having at the

beginning very high spatial density and energy. These charge carriers interact first with each other and spread very quickly inside the crystal. As a quasi−equilibrium situation is reached, they undergo their final degradation via direct interaction with the lattice site: these interactions produce phonons. During this step undesirable processes can take place, indeed a fraction of the pair energy can leave the crystal or can be stored in stable or metastable states instead of going into the crystal lattice. It is possible to have: *radiative recombination* of e/h couples with the escape of the emitted photon, *non-radiative recombination* that take too much time compared to signal development, *trapping* of electrons and holes in the impurity sites or lattice defects. This process reduce the energy resolution of the energy absorbed.
To describe the thermalization of phonons [109] is useful to use the mono dimensional representation of the phonon dispersion curves. The e/h pair

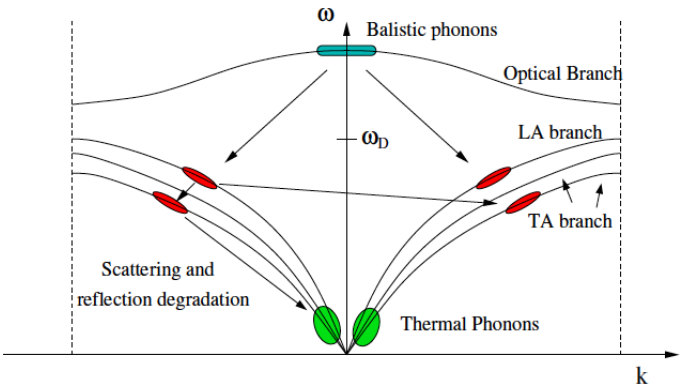

Figure 4.3: Athermal phonon thermalization model.

recombination process across conduction and valence bands produces high energy and low momentum phonons on the optical branch. This phonons decay in longitudinal acoustic band (LA) in a very short time (10/100) ps. The decay produces two phonons each having half the energy of initial one and opposite momenta. The final result is a phonon system in the LA branch with energy of order of $h\omega_D$ (where $\omega_D = 2\pi\nu_D$, ν_D is the cut off Debye frequency that depends on the crystal). This energy is much higher than the average energy of thermal phonons at the bolometer working temperature, therefore this phonon population starts to decay towards a thermal distribution. This happens via three principal processes: phonon/phonon interaction, scattering on impurities and reflection on crystal surfaces. The first channel is possible thanks to the anharmonicity of the lattice potential. However, this anharmonicity is less important when the crystal temperature and the phonon energy decrease. Moreover, while the LA phonons decay is allowed and it is responsible for the transverse acoustic (TA) phonons

production, the decay of the TA phonons is forbidden by the momentum conservation law.

4.2.2 Intrinsic energy resolution

The intrinsic energy resolution ΔE of a bolometer is given by:

$$\Delta E = \sqrt{k_B C(T) T^2}, \tag{4.6}$$

where k_B is the Boltzmann constant, C is the heat capacity given by formula 4.5.
The intrinsic energy resolution of a detector is limited by the statistic fluctuation of the produced elementary excitations. Given the number of elementary excitation:

$$N = \frac{E}{\varepsilon}, \tag{4.7}$$

where ε is the energy to produced an elementary excitation, the theoretical energy resolution is given by:

$$\frac{\Delta E}{E} = 2.35 \frac{\Delta N}{N}. \tag{4.8}$$

In a scintillator detector ε is about 100 eV, whereas in a gas detector and in a solid state detector ε is about 30 eV and 3 eV respectively. In a bolometer the energy of an elementary excitation is less than 0.01 eV therefore
energy resolutions more than an order of magnitude better than the ones of conventional devices are possible.

4.3 Phonon sensor

The phonon sensor is usually a thermistor, which is a resistive device used to convert the thermal signal into an electrical signal. The electrical signal is proportional to the energy of the phonons collected in the energy absorber. The thermistor can be classified in two principal classes:

- semiconductor thermistors (STs): Si or Ge doped crystal by thermal neutrons;
- transition edge sensors (TESs): superconductive film kept at critical temperature T_C.

The thermistor performances are described by the logarithmic sensitivity η, which is given by:

$$\eta = \left| \frac{d\log R(T)}{d\log T} \right|. \tag{4.9}$$

The relation between resistance and temperature in a thermal sensor is obtained by the logarithmic sensitivity formula:

$$\frac{dR}{R} = \eta \frac{dT}{T}. \tag{4.10}$$

It is evident that a large η means a higher response of the device. The value of η is usually in the range $1 - 10$ for ST and it is in the range $10^2 - 10^3$ for TES.

4.3.1 Transition edge sensor

The TESs are intrinsically fast ($\sim \mu s$), and so they can detect athermal phonons. Their working point lies in a narrow range of temperature.
A typical example of a resistance-temperature curve for a TES is shown in figure 4.4. The superconductive film is deposited on the absorber crystal, with typical thickness of a few hundred nanometers [110]. This technique can take advantage of the SQUID technology as read-out. TESs are made normally only by a single superconductor, but it is possible also to use a bilayer film formed by a normal metal and a superconductor. In the latter case, because of the proximity effect, the normal metal is driven superconductive and the resulting T_C can be much lower than that of the pure superconductor. In this way it is possible to tune the T_C by adjusting the thickness of the layers.

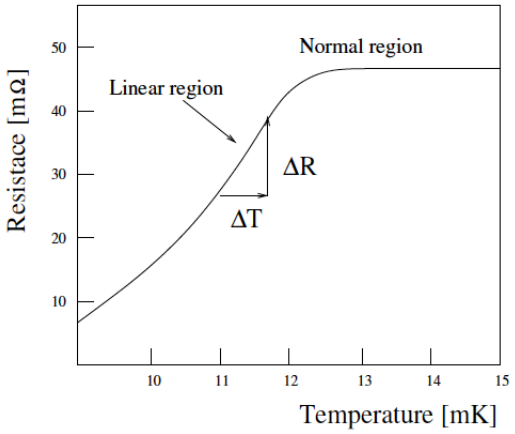

Figure 4.4: Resistance of a TES thermistor as a function of the temperature.

4.3.2 Semiconductor thermistor

The ST response is very slow ($\sim$ ms), but they operate in large range of temperature. A ST is mainly sensitive to the thermal phonons but it also

gives information about the athermal component of the signal [111].
A semiconductor has the valence band completely full and the conduction band completely empty. The energy gap between the two band is of O(eV), for the germanium is 0.67 eV and for silicon is 1.14 eV. This means that for semiconductors without impurities the conduction is possible for high temperature because the energy activation is equal or higher than the energy gap. Since k_BT is of order of 0.025 eV at room temperature, the conduction can only happen at high temperatures.
At low temperature the conduction is given by the presence of impurities, because the impurities generate energy levels between the valence and conduction band. The conduction regime depends on working temperature and concentration of impurities.
Depending on the number of dopant atoms, a semiconductor, can behave as an insulator or a metal even at temperatures close to the absolute zero. So, there exists a critical concentration of dopants N_C that characterizes the transition from the insulator to the metallic behavior of a semiconductor. The region near this concentration is named metal-insulator transition region (MIT) [112].
At temperature lower than 10 K, the conduction occurs between two different impurity levels, without using the conduction band. When the donor concentration is increased, the wave function of the external electron of the donor atom overlaps with the external electron wave function of the neighboring donor atoms. In this situation the electrons are not localized and the conduction happens when the electron jumps from a donor state to the another one by tunneling effect, this conduction regime is called *hopping mechanism*. The migration is activated by phonons, which transmits the necessary energy to the electron to pass trough the potential barrier that separate the two dopant sites.
If $T \ll 10$K and if the net doping atom concentration is slightly lower than N_C, the conduction regime is given by *Variable Range Hopping* (VRH) [113]. The energy of the phonons which are responsible for the conduction mechanism is low and charge carriers migrate also to far impurity sites with free energy levels which are close to the Fermi energy. The concentration of minority charge determines the density of states close to the Fermi level. In the VRH regime, the resistivity is strongly dependent on the temperature, the relation is given by the following law:

$$\rho(T) = \rho_0 exp\left(\frac{T_0}{T}\right)^{\gamma}, \tag{4.11}$$

where ρ_0 and T_0 depend on the doping level.
The exponent γ is equal to 1/4 in the Mott model [114], for a three-dimensional system and for low compensation levels. For larger values of ratio between the acceptor concentration N_A and the donor concentration N_D, the Coulomb repulsion among the electrons leads to the formation of a

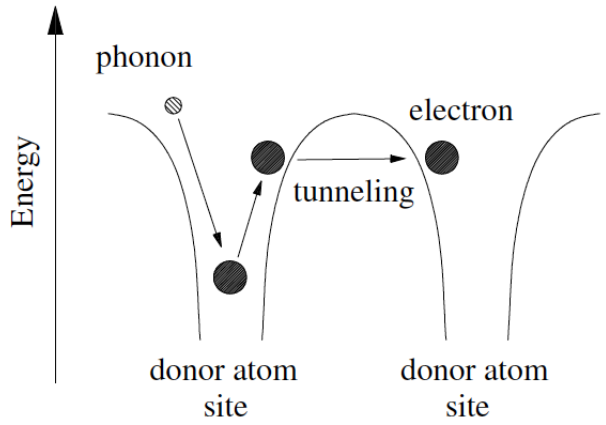

Figure 4.5: Schematic representation of hopping conduction mechanism.

gap (Coulomb gap) in the electron state density near the Fermi energy. The value of γ in this case becomes 1/2 [115].

Chapter 5

CUORE bolometers

5.1 CUORE single module

A CUORE module is the single floor of a tower: it consists of a 2×2 array of cubic TeO_2 crystal absorbers. The four crystals are mechanically and thermally coupled to copper holders, acting as heat bath, using Teflon (PTFE) pieces, acting as thermal coupling. Each crystal is equipped with a semiconductor thermistor (NTD-Ge), which converts the thermal signal in an electrical signal, and a silicon heater, which provides fixed reference pulses for the stabilization of the bolometer response. The NTD-Ge and the heater are glued on the crystal by Araldite Rapid glue, acting as thermal coupling between crystal and sensor/heater.
On the external side of the frames, copper pads are fixed to carry the signal to the electronic read-out. The electrical connection of the sensors is realized by gold wires bonded on copper pads. A sketch of the CUORE single module with its main components is shown in figure 5.1.

5.1.1 Tellurium dioxide crystal

The choice of TeO_2 crystal was determined by its useful properties:

- *high Debye temperature*: a high Θ_D means low heat capacity, so high sensitivity can be achieved; the Θ_D of TeO_2 is 232 K and the heat capacity of a 750 g crystal is 2.3×10^{-9} J/K at 10 mK [116];
- *good thermal and mechanical properties*: large single crystals with excellent mechanical properties can be grown;
- *compound quality and mass*: Te dominates the TeO_2 with respect to the mass (about 80%) permitting to work with large quantity of tellurium.

A dedicated production line was set up for the growth and surface processing of the TeO_2 crystals, in order to reduce the presence of bulk and surface

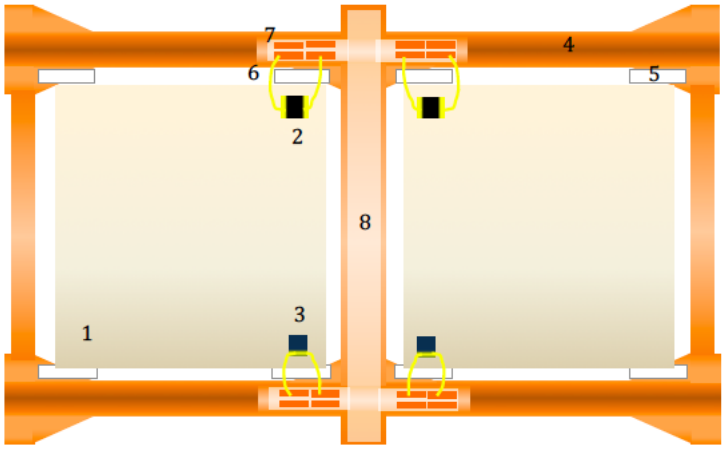

Figure 5.1: Lateral view of the CUORE single module, with all its components: 1) the TeO_2 crystal absorber, 2) the NTD-Ge thermistor, 3) the Si heater, 4) the copper frame acting as thermal bath, 5) the PTFE spacers, linking the absorber to the bath, 6) the gold wires, 7) the copper pad and 8) the wire tray for carrying out the electrical signal.

radioactive contamination into the crystals [117]. The production process of TeO_2 crystals for CUORE is divided into two major phases: crystal synthesis and crystal polishing. Bulk contamination is a risk in the crystal synthesis phase, while surface contamination is the main concern during the crystal processing.
The crystals were grown using Bridgman process in platinum crucibles which consists in two successive crystal growth processes with two associated iterations of TeO_2 powder synthesis, as illustrated in figure 5.2. This procedure guarantees a high quality in terms of radio-purity requirements and bolometer performance. After production the raw crystal ingots were exposed to rough mechanical processing (cutting with specific orientation and shape). The CUORE crystals have strict specifications concerning dimensions, face quality and crystallographic orientation. The final dimension must have cubic shape with a strict tolerance of (50.00 ± 0.05) mm in order to exactly fit in the mechanical holder. The square faces of the final crystals are parallel to crystallographic planes (0 0 1), (1 1 0) and (1 -1 0). The final process is the cleaning that is divided into two steps: chemical etching and polishing. All of production operations were performed in a dedicated clean room.

The crystal production has been outsourced to SICCAS (Shanghai Institute of Ceramics, Chinese Academy of Sciences). Production and certification protocols have been developed and high sensitivity measurements have been performed to check the radio-isotope concentrations in raw materials, reactants, consumables, ancillaries and products used for crystals produc-

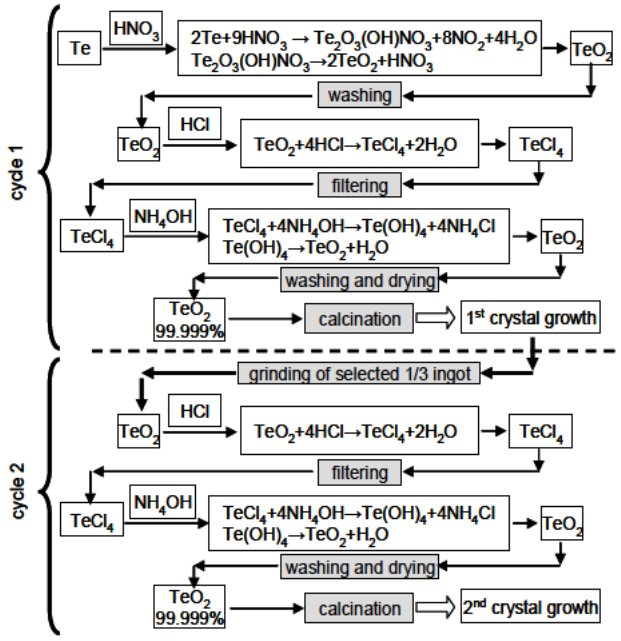

Figure 5.2: Raw material and crystal sinthesys applied for the CUORE crystal.

tion. Moreover some crystals were cryogenically tested in order to check the radio-purity level and bolometer performance at LNGS. The requested limits of bulk and surface contamination were respectively of $< 2.1 \times 10^{-13} g/g$ and $< 2.0 \times 10^{-9} Bq/cm^2$ for ^{232}Th, $< 2.1 \times 10^{-13} g/g$ and $< 8.9 \times 10^{-9} Bq/cm^2$ for ^{238}U [118].

5.1.2 Copper frame

The heat bath is given by the copper support structure, which includes the copper frame, the copper columns and the wire trays used for electronic readout connection (see fig. 5.3). The total mass of copper support is about 3.5 kg per tower. Since the copper is the principal source of background, the amount of copper is minimized in CUORE/CUORE-0 respect the CUORICINO case. In CUORICINO each module was separated from the one below, instead in CUORE the tower is a single unit in which the copper frame acts both as bottom and top holder for adjacent floors (see fig. 5.4).
As previously discussed, the copper is opportunely cleaned by TECM technique to reduce the radioactive contamination. In $2009 - 2010$ a bolometric test was performed (Three Tower Test) to test the cleanliness of CUORE/CUORE-0 copper. The test yielded an upper limit of 1.3×10^{-7} Bq/cm^2 at 90% C.L. for the cleaned copper for both ^{238}U and ^{232}Th [120].

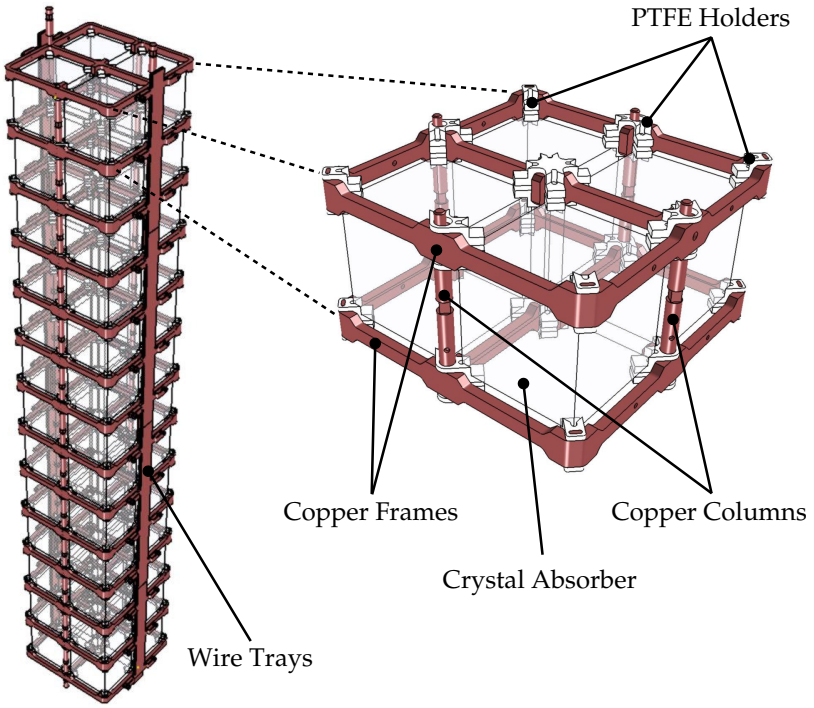

Figure 5.3: Modular structure of CUORE tower in which the copper is used for crystal support, wires trays, collums support. To minimize the amount of copper, each frame acts as bottom and top for adjacent floors.

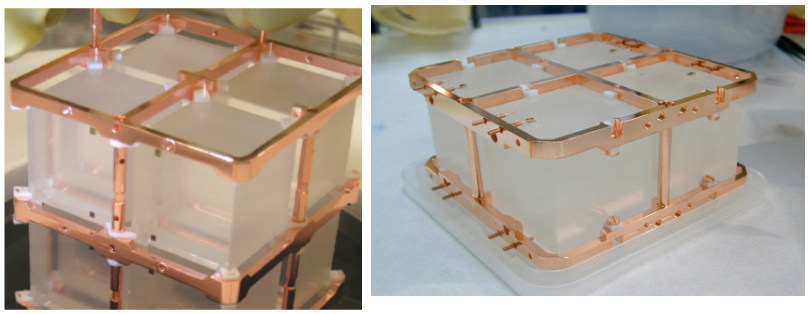

Figure 5.4: On the left an array of 2 CUORE modules. On the right a single module of CUORICINO.

5.1.3 Teflon support

PTFE blocks used to support the crystal inside the copper frame. Since the PTFE support directly touches the detector, the PTFE was opportunely selected and validated with a long radio-assay campaign. The upper limit of radioactive contamination is: 1.5×10^{-12} g/g for ^{232}Th and 1.8×10^{-12} g/g for ^{238}U. After the production, the surface of PTFE holders was thoroughly cleaned by soap and nitric acid to remove any leftover impurity from the machining. Then they are stored in nitrogen until the tower assembly.
The Teflon pieces must be manufactured following precise dimensional tolerances and considering the different thermal contraction of PTFE, copper and TeO_2. The three different types of pieces which are used are shown in figure 5.5 and their position in the tower is shown in figure 5.3.

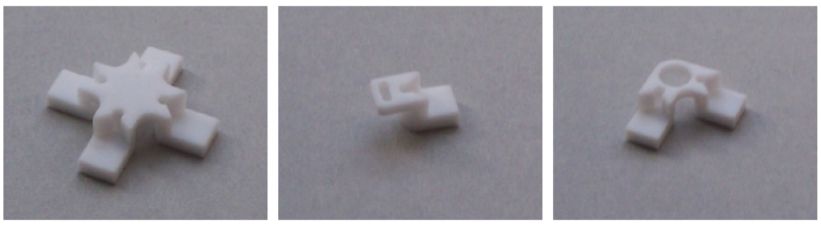

Figure 5.5: The three different types of Teflon block used to hold the crystals in the copper frames.

5.1.4 NTD-Ge sensors

The CUORE sensor is an ultra-pure germanium crystal doped by neutron transmutation technique (NTD-Ge). The germanium wafers are bombarded with thermal neutrons, that, inducing nuclear reactions, creates donor level (As and Se) and acceptor (Ga) impurities by the following nuclear processes:

$$\begin{cases} {}^{70}\mathrm{Ge}(21\%) + n \rightarrow {}^{71}\mathrm{Ge} + \gamma & (\sigma = 3.47 \pm 0.17b) \\ {}^{71}\mathrm{Ge} + e^- \rightarrow {}^{71}\mathrm{Ga} + \nu_e & (t_{1/2} = 11.4d) \end{cases} \quad \text{Acceptor}$$

$$\begin{cases} {}^{74}\mathrm{Ge}(36\%) + n \rightarrow {}^{75}\mathrm{Ge} + \gamma & (\sigma = 0.16 \pm 0.08b) \\ {}^{75}\mathrm{Ge} \rightarrow {}^{75}\mathrm{As} + e^- + \overline{\nu_e} & (t_{1/2} = 83min) \end{cases} \quad \text{Donor}$$

$$\begin{cases} {}^{76}\mathrm{Ge}(7.4\%) + n \rightarrow {}^{77}\mathrm{Ge} + \gamma & (\sigma = 0.16 \pm 0.0014b) \\ {}^{76}\mathrm{Ge} \rightarrow {}^{77}\mathrm{As} + e^- + \overline{\nu_e} & (t_{1/2} = 11.3h) \\ {}^{77}\mathrm{As} \rightarrow {}^{77}\mathrm{Se} + e^- + \overline{\nu_e} & (t_{1/2} = 83min) \end{cases} \quad \text{Double donor}$$

The neutron flux must be stable to obtain the correct doping concentration, during the CUORE NTD production the nominal flux was 3.6×10^{18} n/cm^2. The neutrons energy must be lower than 5 MeV because an excess of fast

neutrons would produce radioactive contaminants (^{3}H, ^{65}Zn, ^{68}Ge). In order to measure the performance of the doped thermistors it is necessary to wait for the decay of the activation product ^{71}Ge (τ=11.4 days). Given the high neutron flux at which the Germanium wafers are exposed, it is necessary to wait at least a few months before testing the cryogenic performance of the sensor. After the decay of ^{71}Ge the wafers are heat treated to repair the crystal structure and are cut to obtain pieces of the desired geometry.
The NTD-Ge sensors operate in the Variable Range Hopping Regime (VRH), in which the resistivity is correlated to temperature by the following relation:

$$R(T) = R_0 exp\left(\frac{T_0}{T}\right)^{\frac{1}{2}}, \tag{5.1}$$

where T_0 depends on doping level and R_0 depends on both the doping level and the sensor geometry. The CUORE−NTDs have dimensions of
$(3 \times 2.9 \times 0.9)$ mm^3.
The R_0 and T_0 parameters were experimentally measured. The NTDs were coupled to a heat sink by a high conductivity epoxy. The temperature of heat sink was varied in the range $(15 - 50)$ mK. The measured values for the R_0 and T_0 parameters for CUORE −NTD are: $R_0 = 1.13$ Ω, $T_0 = 3.84$ K, corresponding to a resistance of about 370 $M\Omega$ at 10 mK.

5.1.5 Silicon heater

The heater is a silicon chip on which a heavily doped meander is realized through standard processes of silicon planar technology. The meander has a low-mobility metallic behavior at low temperatures, providing a constant resistance of ~ 300 $k\Omega$.
Since the thermal detectors are sensitive to temperature drifts, which would spoil their intrinsic energy resolution, the heater is used to correct this effects during the first level of data analysis. The heater periodically inject a fixed−energy pulse into each crystal to emulate particle interaction and bolometer response. The amplitude of the heater pulses is studied as function of baseline average value[1]; since the baseline value represents the bolometer temperature, a polynomial fit of the baseline vs heater amplitude (see fig. 5.6) is used to correct the signal pulse amplitude drift [119].
In order to have a reliable temperature drift correction, all the CUORE-0 heaters were characterized to determine their resistance value and its stability with temperature. Also the uniformity of the implant has to be proved by measuring the pads-to-pads low temperature resistances.

[1] CUORE-0 pulse are acquired in a time window of 5 s, the value of baseline is measured in the pre-trigger time window (1 s).

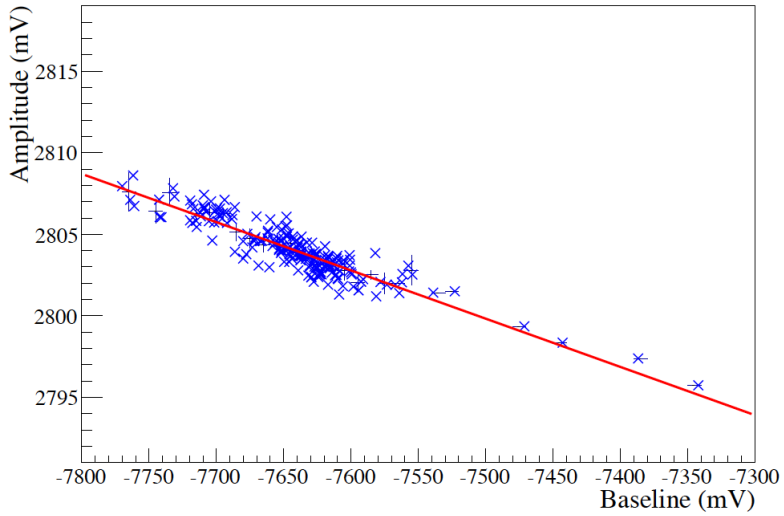

Figure 5.6: Example of fit of baseline vs heater amplitude used to correct the signal pulse amplitude.

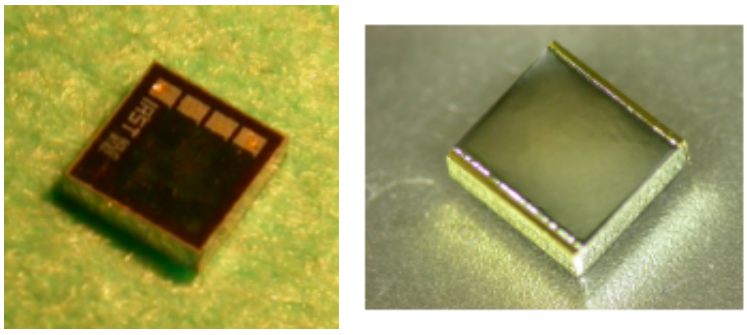

Figure 5.7: A silicon heater on the left. A NTD-Ge on the right.

5.1.6 Gluing of sensor and heater to crystals

The gluing between crystal and heater/sensor is done by an array of glue spots of Araldite Rapid [121]. This specific glues was chosen for its rapid curing time ($\sim$ 1 hour), low radioactivity ($< 2.2 \times 10^{-10}$ g/g for ^{232}Th and $< 8.2 \times 10^{-10}$ g/g for U) and for its good thermal conduction. Furthermore, its cryogenic performance was established in previous TeO_2 bolometric tests. The thermistor is glued to the crystal by nine dots while the heater is glued to the crystal by five dots (see fig. 5.8). The glue distribution into array of glue spots compensates the different thermal contraction between TeO_2, glue and semiconductor chip, in order to prevent fractures or detachments of the elements occurring at low temperatures. The sensor−crystal gluing plays a crucial role in the bolometer performance. A semi automatic system was developed to guarantee a precise and reproducible sensor−crystal coupling in the CUORE assembly line. This system (see fig. 3.10) includes a robotic arm to lift and position the crystal and a Cartesian pointer to dispense glue dots on the sensor and heater via a pneumatic dispenser.

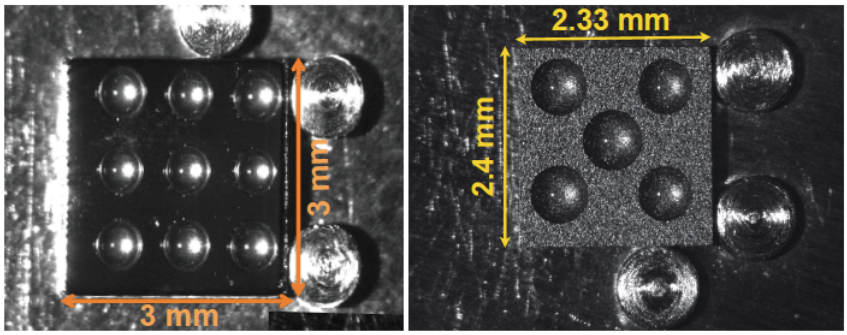

Figure 5.8: Glue-spot matrices deposited on a thermistor (left) and a heater (right) using the CUORE gluing workstation.

5.1.7 Wiring readout: Cu-PEN tapes and gold wires

Each CUORE crystal is instrumented with one thermistor and one heater. At the low temperature stage the signal is read out by a set of 2.4 m long, 80 μm thick, Cu tapes having Polyethylene Naphthalate substrate (Cu-PEN tapes).
The design of Cu-PEN tapes must satisfy different specifications, as low background, negligible cross-talk, negligible microphonics, very large parasitic impedance and high level of packaging. Each tower is equipped with two packs of nine wire tapes each. Each packs has tree tapes to connect the 26 thermistors, and one tape to connect the heaters of the same 26 crystals. Figure 5.9 shows the different tape shapes used for thermistors and heaters:

T1 reads the signals of thermistors from floor one to five (the counting starts at the top of the tower), T2 for signals from floor six to nine, T3 for signals from floor ten to thirteen and the heater tape, which contains two separate channels that connect each of two columns of 13 heaters in parallel. The two packs tape are glued on the copper wires tray, running on the two opposite side of the towers.

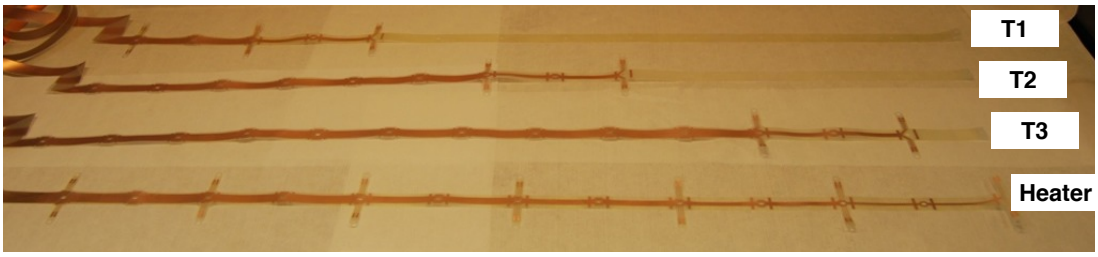

Figure 5.9: The four types of CUORE/CUORE-0 Cu−PEN tapes. The picture shows the bottom $\sim$ 80 cm of the tapes that were located on the sides of the tower.

The electrical connections between thermistor/heaters and read-out chain are made by 25 μm diameter gold wire connections at the low temperature stage. Each gold wire is first bonded to the chips and then to the Cu-PEN trace. For redundancy two wires were bonded for each electrical connection. In CUORE-0/CUORE the bonding process is done after the gluing and after all the crystals are placed in the tower (see fig. 5.10).

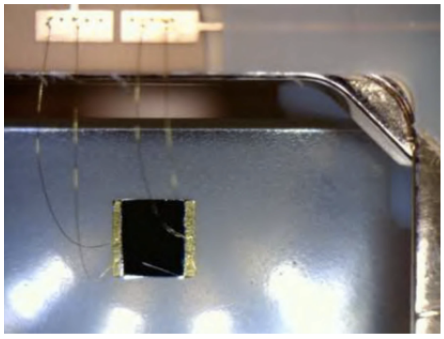

Figure 5.10: Detail of the bonding connection of a NTD thermometer. The gold pads of the thermistor are connected to the copper pads of the Cu-PEN cable through gold wires.

5.2 Bolometer operation

To measure the temperature variation, the semiconductor sensor is biased by the circuit shown in figure 5.11. The bias current is generated by a voltage generator (V_{BIAS}) closed on a load resistance R_L put in series with the sensor resistance R_{bol}. The load resistance is much higher than sensor resistance so that the current is constant and the thermistor voltage is:

$$V_{bol}(T) = I_{bol} \cdot R_{bol}(T). \tag{5.2}$$

The bias current produces a power dissipation $P = VI$ which increases the temperature and acts back on the resistance R(T), until an equilibrium is reached. This phenomenon is called "electrothermal feedback" which produces a non−ohmic behavior in the $I - V$ relation, that deviates from the linearity (see fig. 5.12). Increasing the bias current, the slope of the $I - V$ curve increases until the inversion point (IP) in which the curve slope starts to decrease. In static conditions the thermistor electric and thermal parameters are described by a point on the load curve. The working point is given by the intersection between the $I - V$ load curve and the line given by the equation $V = V_{bol} - IR_L$.
In static condition the sensor temperature is:

$$T_S = T_{hs} + \frac{P}{G}, \tag{5.3}$$

where the T_{hs} is the heat sink temperature and G the conductance between sensor and heat bath.

The relation between P and R at different temperatures is shown in figure 5.11.

Given the circuit in figure 5.11 the voltage signal is given by:

$$\Delta V = \frac{R_L}{R_L + R} \cdot V \cdot \eta \cdot \frac{\Delta T}{T_S} \sim \frac{E}{CT_S} \cdot \eta \cdot \sqrt{P \cdot R}, \tag{5.4}$$

where T_S is the static detector temperature, ΔT is the increase of detector temperature, η is the logarithmic thermistor sensitivity. The expression vanishes for $P \to 0$ and for $P \to \infty$ because $CT_S \to \infty$.
Neglecting the noise, the optimal working point is analytically determined by a scanning of pulse amplitude for fixed energy varying the bias current and selecting the point in the linear region of $I - V$ curve and in which the signal amplitude is maximal (see fig. 5.12).
The eletronic readout system [97] provides a low-noise system to acquire the detector signals and to monitor and optimize its performances. It consists of six parts: front-end, antialiasing filter, pulser, linear power supply, AD/CD pre-regulator and data acquisition system (see fig. 5.13).

The front-end provides low-noise DC bias to the NTDs. It also performs the

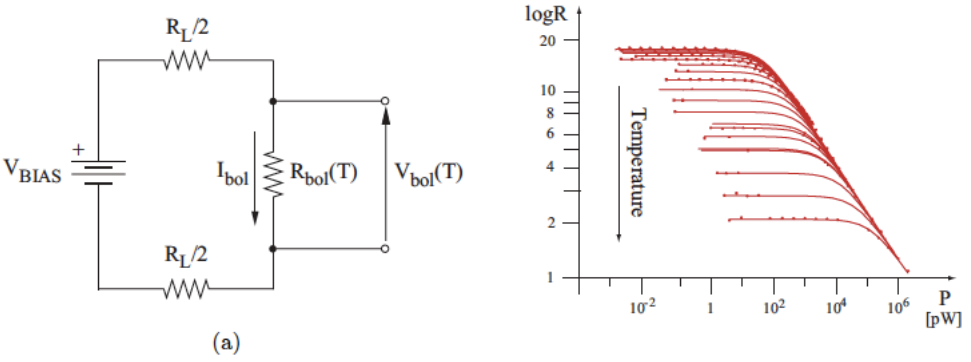

Figure 5.11: The left picture shows the electric scheme of the bias circuit used for thermistor readout. The right picture shows the dependence of the resistance on the power dissipation for various values of the base temperature. Curves with lower resistance at P=0 correspond to higher base temperatures.

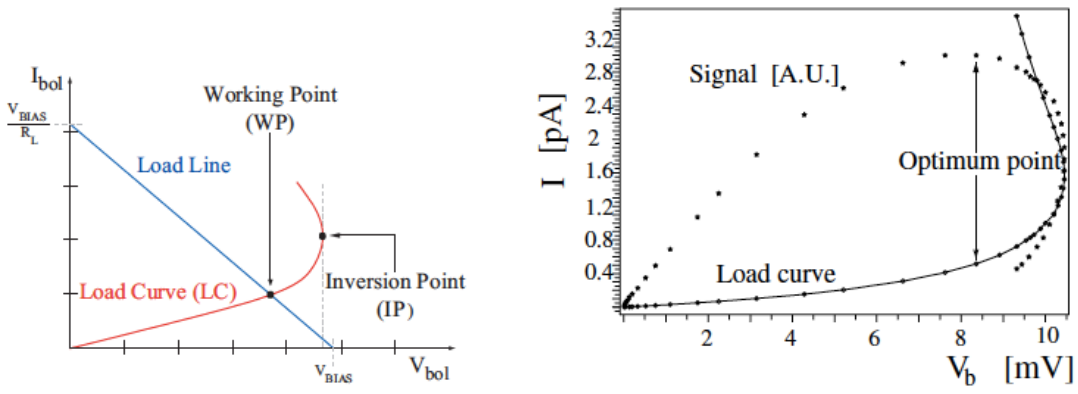

Figure 5.12: Load curve of a semiconductor thermistor. On the left the working point is determined by the intersection of the sensor characteristic curve with the bias circuit load line. On the right the load curve is shown together with the corresponding signal amplitude.

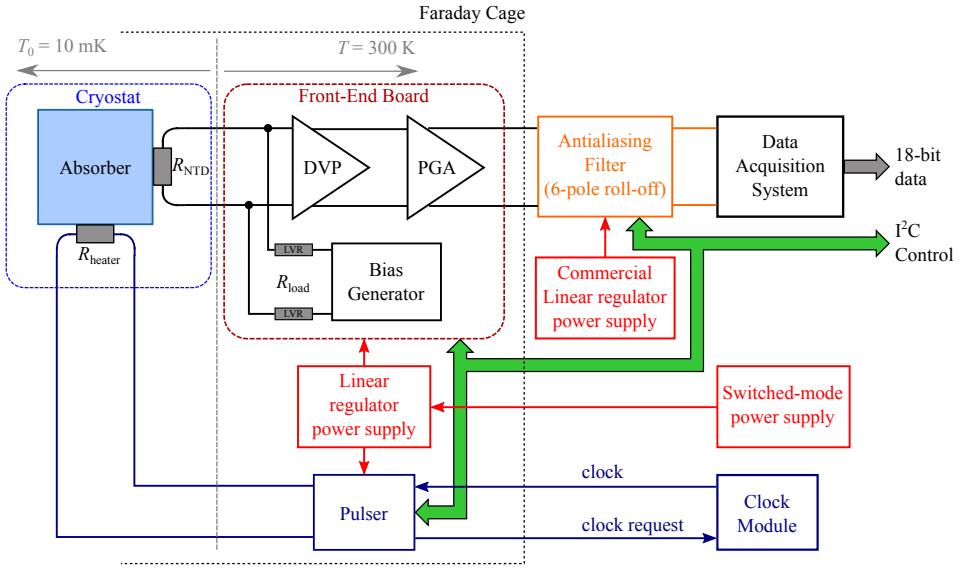

Figure 5.13: CUORE-0 electronics block diagram.

readout of the voltage across the NTD and passes the voltage signal through a two stage amplifier (DVP and PGA) to increase the voltage signal from $\sim 100\ \mu V/MeV$ to $\sim 1V/MeV$.

5.2.1 CUORE-0 working point

After the CUORE-0 cool down, the optimal working point was evaluated for each bolometer. For each CUORE-0 crystal this measurement consists in the evaluation of bolometer voltage, baseline RMS and amplitude of a fixed energy heater pulse for each value of bias current.
The bolometer voltage is evaluated as:

$$V_S = \frac{V^+ - V^-}{2G_S}, \tag{5.5}$$

where V^+ and V^- are the output bolometer voltages measured for two opposite bias voltages V_{BIAS}. The difference of output bolometer voltage is divided for the know gain of readout chain (G_S) to eliminate possible offset produced by readout chain. The baseline noise RMS is evaluated by average noise power spectrum. The reference amplitude is given by the average of several pulser amplitudes.
In figure 5.14 the result of the optimal working point for CUORE-0 bolometers is shown. On the top the characteristic $I - V$ curve and the pulser amplitude curve are shown. On the bottom the RMS noise and the signal-to-noise curve are shown. The RMS noise decreases for high bias current. The optimal working point is chosen to maximize signal-to-noise, given by

the ratio between the reference pulser amplitude and RMS noise.
In CUORE-0 the average bolometer signal amplitude, defined as the ratio

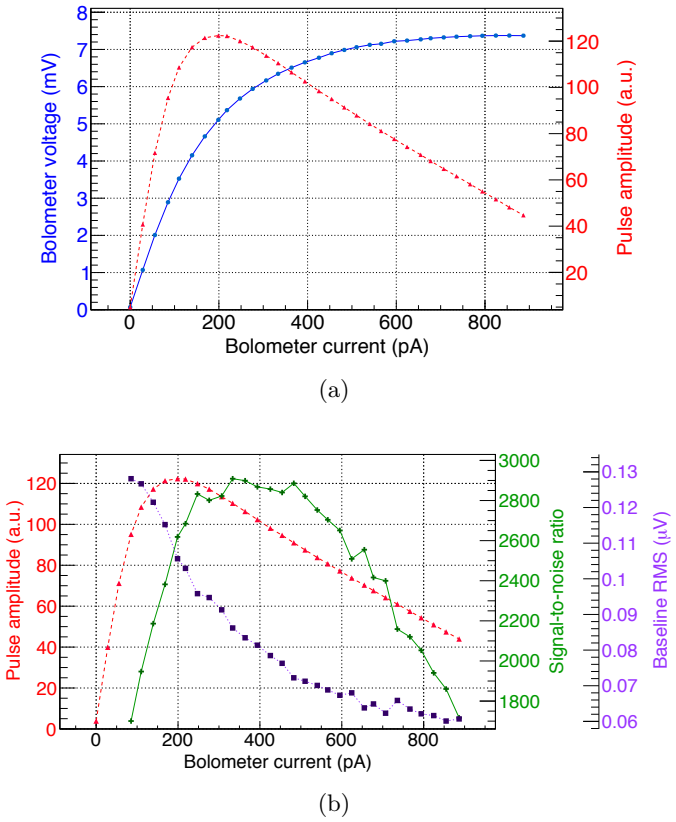

Figure 5.14: Detector characterization curves. Top: I-V curve (blue solid) and pulse amplitude curve (red dashed). Bottom: The same pulse amplitude curve (red dashed) with the baseline RMS curve (purple dotted) and their ratio (green solid) [97].

between the pulse amplitude and the energy released into the crystal, is $\sim 76.6\ \mu V/MeV$. In figure 5.15 a typical 2615 keV pulse is shown.

5.2.2 Thermistor uniformity

Each NTD-Ge thermistor was characterized in order to determine the values of R_0 and T_0, see section 5.1.4., before the assembling process. However in the past was observed that the stress induced by differential thermal contraction between the glue and the NTD could alter the NTD-Ge characteristic parameters, R_0 and T_0. As a consequence (assuming that all the NTDs of the CUORE-0 towers are at the same temperature) an estimate of the reproducibility of the gluing process can be deduced from the distribution of the

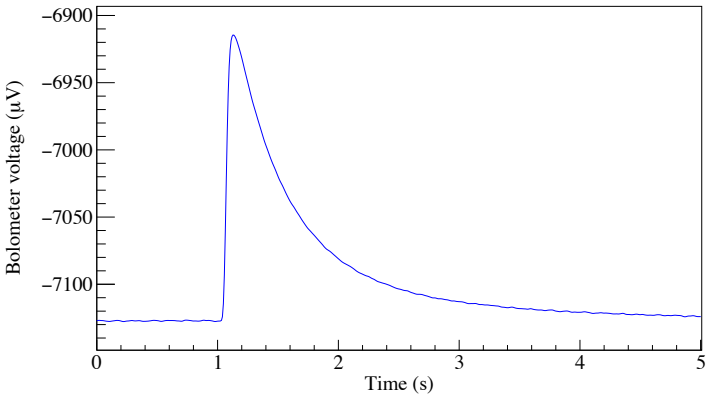

Figure 5.15: A typical 2615 keV pulse.

NTD temperatures derived from their base resistances. The temperature distribution of all CUORE-0 bolometers was compared with CUORICINO, in which the gluing between sensor and crystal was performed with a manual procedure, in order to study the effect of gluing process on NTD-Ge parameters. The thermistor temperature is evaluated using equation 5.1:

$$T(R_{base}) = T_0 \left[ln \frac{R_{base}}{R_0} \right]^{1/2}, \tag{5.6}$$

where R_{base} is the sensor resistance measured with low bias current. The same measurement was done for CUORICINO bolometers.
In figure 5.16 the ratio T/T_{avg}, where T_{avg} is the average of bolometer measured temperature, is shown. The narrower distribution of
CUORE-0 respect to CUORICINO demonstrates the improvement achieved by the gluing process adopted for the CUORE towers.

5.3 Noise sources

In a bolometer detector the noise sources are given by the vibrations of cryogenic apparatus, electronic readout and Johnson noise .
In CUORE-0 the dominant noise comes usually from vibrations of cryogenic system. They produce an energy dissipation into the crystal, that causes a temperature variation. This temperature variation has a frequency spectrum similar to the signal one. The cryogenic apparatus vibrations also changes wire-wire capacitance and wire-ground capacitance: this noise is known as *microphonic noise*.
The Johnson noise produced by a resistance R working at temperature T is

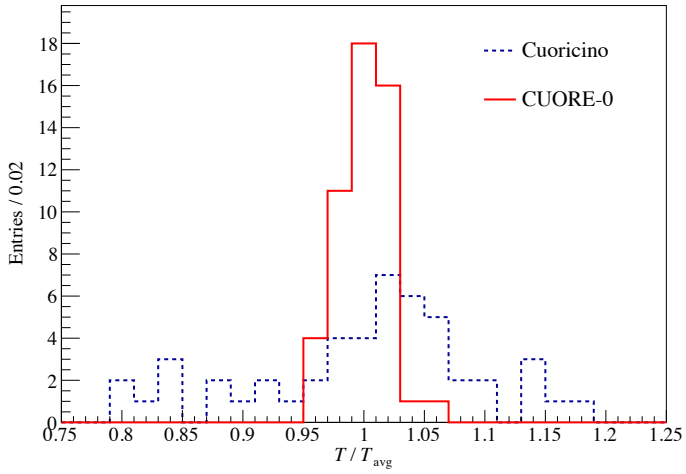

Figure 5.16: Comparison of the base temperatures of the bolometers normalized to their average temperature for CUORE-0 (red line) and Cuoricino (blue dashed line) [97].

due the agitation of the charge carriers and it can be expressed as:

$$\Delta V^2 = 4k_B T_R R, \tag{5.7}$$

so the bolometer output voltage becomes:

$$\Delta V_b^2 = \frac{\Delta V_L^2}{R_L^2}\left(\frac{R_S R_L}{R_S + R_L}\right)^2 \simeq 4k_B T \frac{R_S^2}{R_L}. \tag{5.8}$$

The CUORE front-end electronics is designed in order to introduce negligible noise in the frequency range (0-20) Hz of the CUORE signals. The noise produced by the electronic readout is of three types:

- *series*: generated by the JFET[2] transconductance;
- *series 1/f* : that amount to 15 eV rms;
- *parallel shot*: that amount to 130 eV rms at room temperature.

5.4 CUORE-0 bolometer performance

The energy resolution is an important parameter in the $0\nu\beta\beta$ search because it determines the ability to discriminate the $0\nu\beta\beta$ peak from the background. The energy resolution of CUORE-0 bolometers was evaluated using calibration data collected while the detector was exposed to thoriated tungsten

[2]Present in the differential amplifier of front-end, DVP and PGA in figure 5.13.

wire sources. These sources were inserted between the OVC of the cryostat and the external lead shield on opposite sides of the tower. In figure 5.17 the sum calibration spectrum of all CUORE-0 channels is shown [97].

The energy resolution has been evaluated on ^{208}Tl photo−peak (2615 keV)

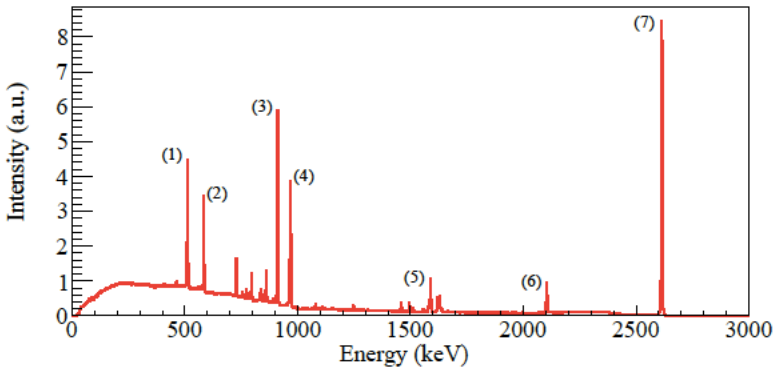

Figure 5.17: CUORE-0 sum calibration spectrum. The peaks are identified as γ lines from the decay of nuclei in the ^{232}Th decay chain: (1) 511 keV ($e+e-$ annihilation), (2) 583 keV (^{208}Tl), (3) 911 keV (^{228}Ac) ,(4) 965 keV and 969 keV (^{228}Ac), (5) 1588 keV (^{228}Ac) (6) 2104 keV (^{208}Tl with single 511 keV escape), (7) 2615 keV (^{208}Tl).

because it is the high−statistics signal closest to the ROI (2527.5 keV) (see fig. 5.18). The energy resolution was estimated for each CUORE-0 channel and the values distribution is reported in figure 5.19. The effective mean of the FWHM values for all CUORE-0 channels is 4.9 keV [100], so the CUORE goal of 5 keV seems to be within reach.

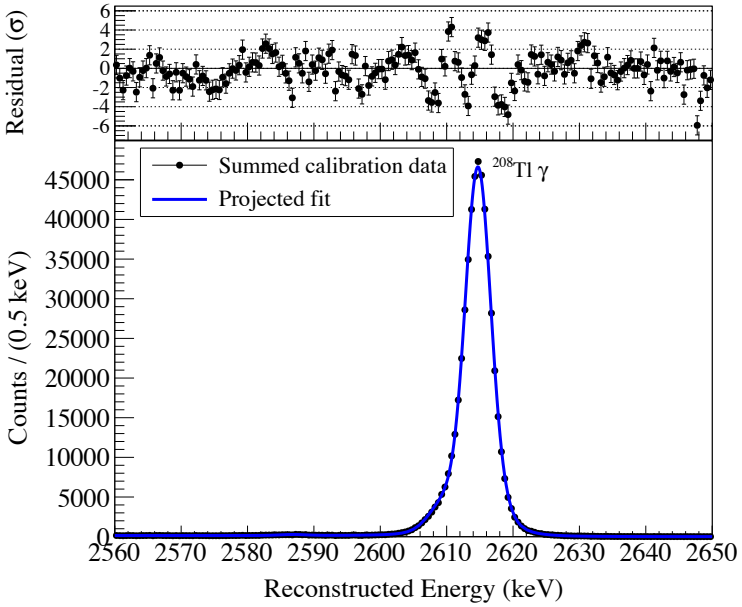

Figure 5.18: CUORE-0 crystal energy resolution estimated by ^{208}Tl photopeak.

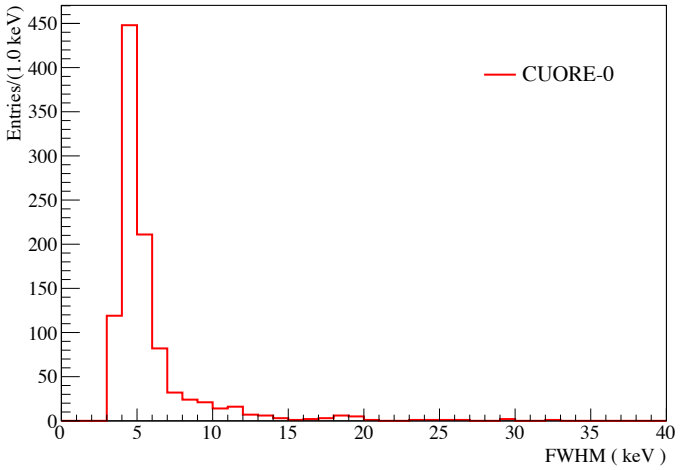

Figure 5.19: CUORE-0 channels energy resolution distribution.

Chapter 6

CUORE-0 bolometer response model

6.1 Introduction

The aim of this Ph.D. thesis is the study of CUORE-0 response and behavior in order to better understand the CUORE detector.
The response of a CUORE bolometer is more complex than the ideal bolometer one, which was described in section 4.1. Up to now a full thermal model able to characterize the CUORE detector response has not been developed. Finding the different components of the CUORE-0 pulses and correlating them to physics parameters will allow a better understanding of the detectors and possible improvements of the response (e.g. energy resolution).

6.2 CUORE bolometer thermal model

A predictive thermal model should be composed by the relevant heat capacities and thermal conductances, chosen among all the possible components. In the previous chapter the CUORE bolometer was described in detail. Contribution to heat capacities could be given by:

- TeO_2 crystal;
- PTFE support;
- glue;
- silicon heater;
- NTD lattice;
- NTD electrons.

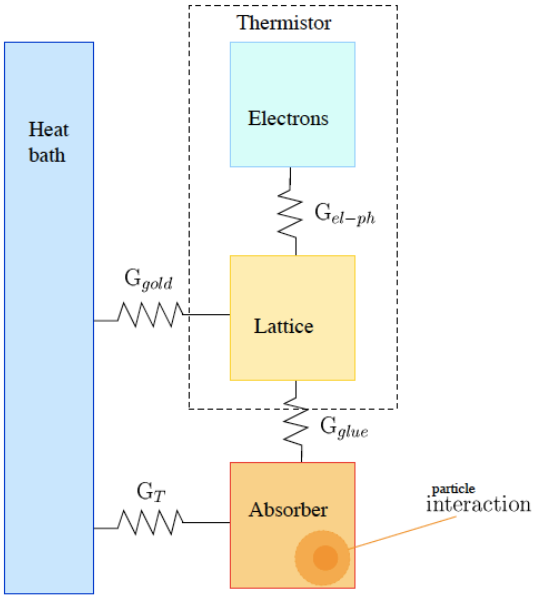

Figure 6.1: One possible CUORE thermal model. The thermal couplings are given by teflon support (G_T), glue spot (G_{glue}), gold wires and electron/phonon decoupling (G_{gold}) [122].

The thermal conductances to be considered are:

- Teflon support (thermal link copper/crystal);
- glue spots (thermal link sensor/crystal and heater/crystal);
- gold wires (thermal link copper/sensor and copper/heater).

The thermal models normally take also into account the decoupling between electrons and phonons in the semiconductor sensor produced by power dissipation. This effect is described by the so called *Hot Electron Model* (HEM). According to this model the electron system and lattice system are at two different temperatures, T_e and T_r, and the two systems are connected by a thermal conductance G_{el-ph}.
Several thermal models were developed to describe the CUORE bolometer response, one of them is reported in figure 6.1. None of them completely characterizes the CUORE bolometers response and their performances, and do not explain the different responses observed for each CUORE-0 crystal (see fig. 6.2).

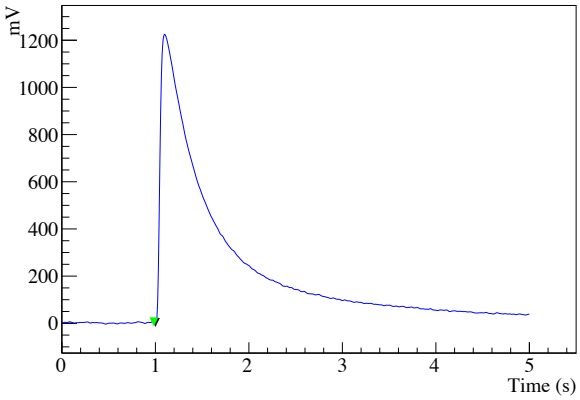

(a)

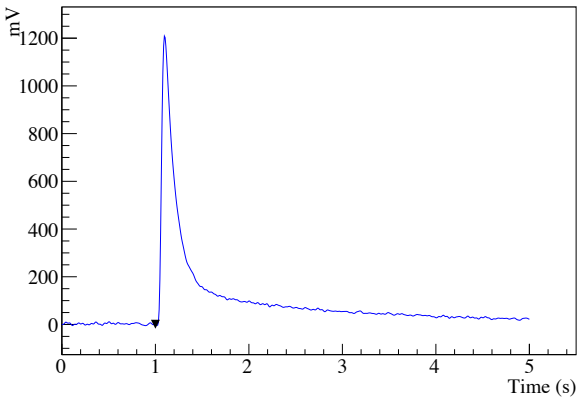

(b)

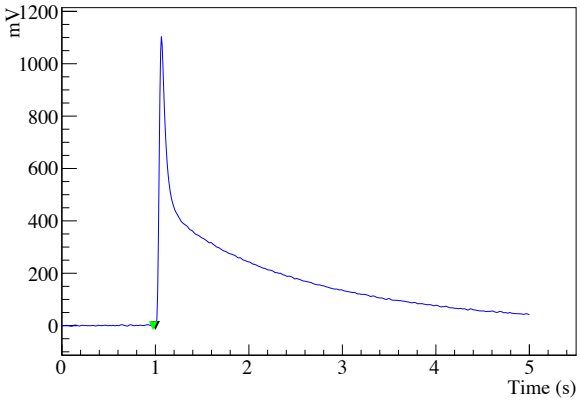

(c)

Figure 6.2: Example of CUORE-0 pulse shapes.

The aim of this Ph.D.-thesis is the developing of CUORE thermal model using a reverse approach, namely:

- define a set of parameters which describe the pulse shape;
- find possible correlations between pulse shape parameters and physical one;
- identify the effective heat capacities and thermal conductances;
- develop a predictive thermal model.

The energy resolutions measured by CUORE-0 shows that each crystal has a different one and it is not dominated by electronic effects, so a deeper comprehension of CUORE detectors could improve the energy resolution.

6.3 Pulse shape model

A bolometer can be described by an electrical circuit, in which any heat capacity is replaced by an electrical capacity, the thermal conductivities act as electrical conductances, the temperature acts as a voltage and the power released into the crystal is represented as a current generator. In the Laplace domain the electrical capacity is represented by an impedance $Z = \frac{1}{sC}$ and the electrical conductance by $G = 1/R$.
The circuit response is given by the inverse Laplace transform of the product between the transfer function F(s) and input signal I(s):

$$L^{-1}[F(s) \times I(s)], \tag{6.1}$$

where s is the standard Laplace variable $s = j\omega$.
Since it is normally assumed that the energy released by a particle interaction is much faster than the circuit response, I(s) is written as a δ function ($L^{-1}[I(s)] = 1$). Therefore the solution of the thermal circuit is the inverse Laplace transform of F(s). The transfer function F(s) can be written as:

$$F(s) = \frac{b(s)}{a(s)} = \frac{b_m s^m + b_{m-1} s^{m-1} + ... + b_1 s + b_0}{s^n + a_{n-1} s^{n-1} + ... + a_1 s + a_0}, \tag{6.2}$$

where the numerator b(s) and denominator a(s) depends on circuit's elements.
An equivalent form, in which the transfer function can be written, is:

$$F(s) = K \frac{(s - z_0)(s - z_i)...(s - z_{m-1})(s - z_m)}{(s - p_0)(s - p_i)...(s - p_{n-1})(s - p_n)}, \tag{6.3}$$

in which the z_i and the p_i are defined as the *zeros* and the *poles* of F(s). The *zeros* are the roots of the numerator b(s) and represented the values in

which the F(s)=0. The *poles* are the roots of the denominator of a(s) and represented the values in which the $F(s) \to \infty$.
The degree of F(s) is equal to $R = n - m$, where n is the degree of a(s) and m is the degree of b(s). In the case of stable circuit ($R \geq 1$), as the CUORE thermal circuit, the F(s) can be decomposed as a function of the poles:

$$F(s) = \frac{A_1}{s - p_1} + \frac{A_2}{s - p_2} + ... + \frac{A_n}{s - p_n}. \tag{6.4}$$

If the poles are all negative and real (as normally happens in thermal circuits), thus the inverse Laplace transform of each single terms of F(s) is an exponential:

$$\frac{A_i}{s - p_i} \Longleftrightarrow A_i exp[p_i t]. \tag{6.5}$$

Each amplitude A_i can be estimated as the residual in the poles of transfer function:

$$A_i = \lim_{s \to p_i} (s - p_i) F(s)|_{s=p_i}. \tag{6.6}$$

As a consequence, in the time domain, the bolometer response can be described by a sum of n exponentials:

$$A_1 exp[p_1 t] + A_2 exp[p_2 t] + ... + A_n exp[p_n t], \tag{6.7}$$

The number of time constants is determinated by the number of poles, $\tau_i = -\frac{1}{p_i}$, which correspond to the number of the independent heat capacities of the thermal circuit, so the definition of time constants that describe the CUORE pulse shape could provide the identification of effective heat capacities.
The sign of the amplitudes depends on the number of zeros of F(s) and on their values compared to the value of the poles. For example in the case in which F(s) has three poles and one zero, ordered as:

$$p_3 < p_2 < z_0 < p_1, \tag{6.8}$$

the three corresponding exponentials amplitude are:

$$\begin{cases} A_1 = \frac{p_1 - z_0}{(p_1 - p_2)(p_1 - p_3)} \\ A_2 = \frac{p_2 - z_0}{(p_2 - p_1)(p_2 - p_3)} \\ A_3 = \frac{p_3 - z_0}{(p_3 - p_1)(p_3 - p_2)} \end{cases}$$

The sign of A_1 and A_2 is positive and A_3 is negative, so the response of the circuit is described by one rise plus two decays:

$$A_1 exp[p_1 t] + A_2 exp[p_2 t] - A_3 exp[p_3 t]. \tag{6.9}$$

It is important to note that in this case:

$$A_1 + A_2 + A_3 = 0. \tag{6.10}$$

The fact that the sum of the amplitudes is equal to zero is valid in general when $R \geq 2$.
Given the previous considerations, the pulse shape fit function that has been used to fit the CUORE-0 pulses is the following:

$$F_{pulse} = \begin{cases} 0 & t \leq t_0 \\ A_1 exp\left[-\frac{t-t_0}{t_1}\right] + A_2 exp\left[-\frac{t-t_0}{t_2}\right] + ... - (A_1 + A_2 + ...A_n) exp\left[-\frac{t-t_0}{t_r}\right] & t > t_0 \end{cases}$$

where t_0 is the trigger time. Since the pulse is zero at trigger time, the amplitude of the rise exponential is imposed equal to the sum of the amplitudes of the decay exponential:

$$A_r = -(A_1 + A_2 + ...A_n). \tag{6.11}$$

The pulse shape is fitted varying the number of exponentials in order to identify the minimum number of time constant that describe the CUORE bolometer response.

6.4 Electronic chain model

The full fit function must take into account the effects produced by the electronics on the pulse shape, mainly by the RC filter and by the 6-poles Bessel filter. The 6-poles Bessel filter is used to reduce the aliasing noise in the out-of-band frequency. It was chosen because it preserves the shape of the input signal even when its roll-off is close to the signal frequency bandwidth. The RC filter is produced by parasitic capacitance of wiring that connects the NTD sensor to the readout electronic system.

6.4.1 Bessel filter function

The six poles Bessel function is:

$$B(\sigma) = \frac{10395}{\sigma^6 + 21\sigma^5 + 210\sigma^4 + 1260\sigma^3 + 4725\sigma^2 + 10395\sigma + 10395}, \tag{6.12}$$

where σ is the normalized Laplace variable:

$$\sigma = s\frac{2.70339501}{\nu_t}, \tag{6.13}$$

and ν_t is the Bessel cutoff frequency, that is 12 Hz in CUORE-0.
The principal effects of the Bessel filter are a distortion on the rise of the

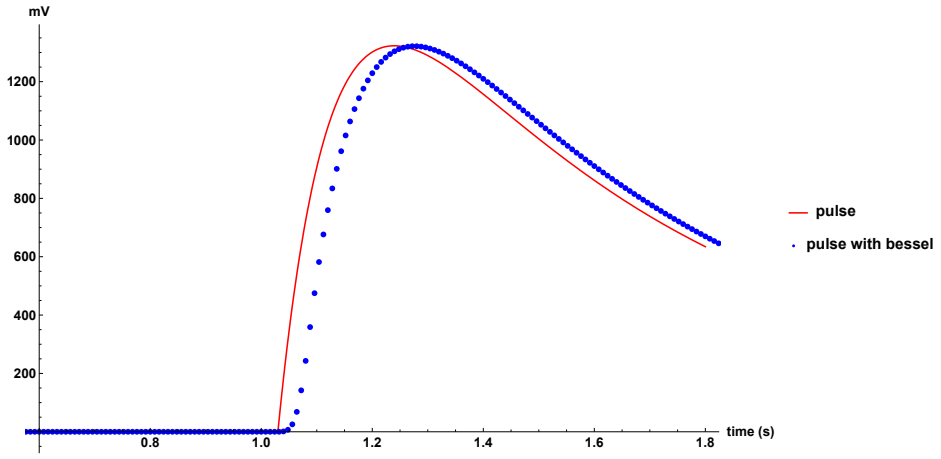

Figure 6.3: Effects on the rise of pulse produced by bessel filter with 12 Hz cutoff frequency.

pulse and a delay on the trigger time of the pulse (see fig. 6.3).

Since the Bessel function in very complex, it is easier to simulate the filter effects using a sigmoid function to simplify the fit computing program. The sigmoid function has a s-shape that describes the pulse distortion produced by Bessel filter (see fig. 6.4).

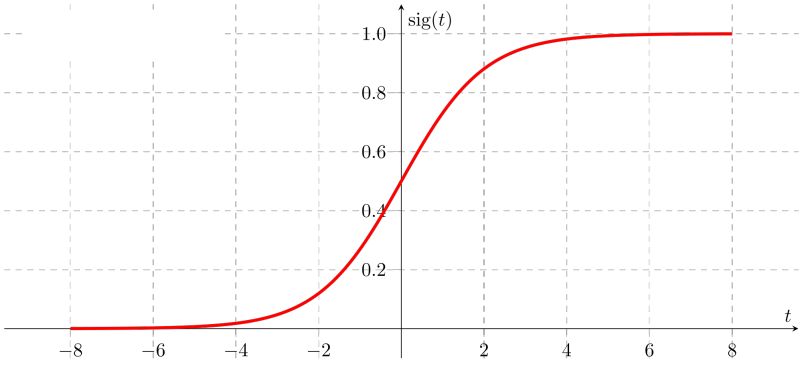

Figure 6.4: Sigmoid function. Its s-shape simulated the Bessel distorsion on the pulse.

The sigmoid function is:

$$sigmoid = \frac{1}{1 + exp[-s(t - s_0)]}. \tag{6.14}$$

The parameter s represents the slope of the sigmoid, that simulates the pulse rise distortion. The parameter s_0 is used to estimate the delay on the trigger time produced by Bessel filter, that is $s_0 - t_0$.

6.4.2 RC filter function

The RC filter function is:

$$H(s, RC) = \frac{1}{1 + sRC_p}, \tag{6.15}$$

and the corresponding cutoff frequency is given by:

$$\nu_{RC} = \frac{1}{2\pi RC_p}, \tag{6.16}$$

where C_p is the parasitic capacitance of the wiring, that carries the signal out of the cryostat (which depends on the length of the wires) and R is the NTD working point resistance.
Each bolometer has a different RC cutoff frequency because each NTD has its own working point resistance and the parasitic capacity depends on the crystal position in the tower.
In CUORE-0 the wiring consists of three different wires in series, each one with its own capacitance: the one of Cu-PEN tape (see section 5.1.5), the one of the cable which carries the signal from the mixing chamber to the 300 K plate of the cryostat (C_{cryo}) and the one of the fisher cable (C_f) which connects cryostat feedthroughs to front-end electronic at room temperature. The three capacitance are in parallel, so the total capacity is:

$$C_p = C_{Cu-PEN} + C_{cryo} + C_f. \tag{6.17}$$

The capacitance of Cu-PEN tape varies in the range $[26 - 37]$ pF, the capacitance of low temperature wiring varies in the range $[368 - 668]$ pF and the fisher cable capacitance is 135 pF[1]. The total capacity varies in the range $[529 - 831]$ pF.
The pulse shape analysis was done on two datasets[2], in which the working point resistance[3] varies in the range $[15 - 60]$ $M\Omega$ and $[10 - 30]$ $M\Omega$.
In the time domain the RC filter is described by the following exponential:

$$f_{RC}(t) = \frac{1}{RC_p} exp\left[-\frac{t}{RC_p}\right], \tag{6.18}$$

where $\tau = RC_p$ is the RC time constant.

[1] The vales of parasitic capacitance are measured for the wiring of all CUORE-0 channels.

[2] The CUORE-0 data collection was organized in runs, with each run lasting approximately one day. The runs are distinguished in background run, in which the background spectrum is evaluated, and calibration run, in which the calibration energy parameters are defined. Runs were grouped into datasets, which started and ended with a calibration measurement, each of which lasted approximately three days.

[3] The NTD working point resistance is measured at the beginning of each dataset.

6.5 Definition and optimization of fit function

The CUORE-0 response model is given by the following equation:

$$L^{-1}[B(s) \times H(s, RC) \times F_{pulse}(s)], \tag{6.19}$$

where $B(s)$, $H(s, RC)$ are the Bessel function and the RC filter function, respectively.
Given all the previous considerations, the used fit function is given by:

$$\frac{1}{1 + exp[-s(t - s_0)]} \times \left[\frac{1}{RC_p} exp\left[-\frac{t}{RC_p} \right] \bigotimes F_{pulse}(A_n, t_r, t_{d_i}) \right]. \tag{6.20}$$

Two different datasets, acquired in different conditions and calibrated with different sources, were analyzed. One dataset was collected using the standard CUORE-0 acquisition (LF dataset) with a 12 Hz Bessel cutoff frequency and 125 Hz frequency sampling. The calibration was done by a thorium source, the energy spectrum is shown in figure 5.18.
In the final period of CUORE-0 data-taking, one "ad hoc" measurement (HF dataset) was done for the thermal model study. The pulses were acquired with a Bessel cutoff frequency of 120 Hz and a frequency sampling of 1 kHz, while the calibration was done with ^{56}Co source; the corresponding energy spectrum is shown in figure 6.5.
The RC cutoff frequency varies in the range [4 - 17] Hz and [7 - 27] Hz for

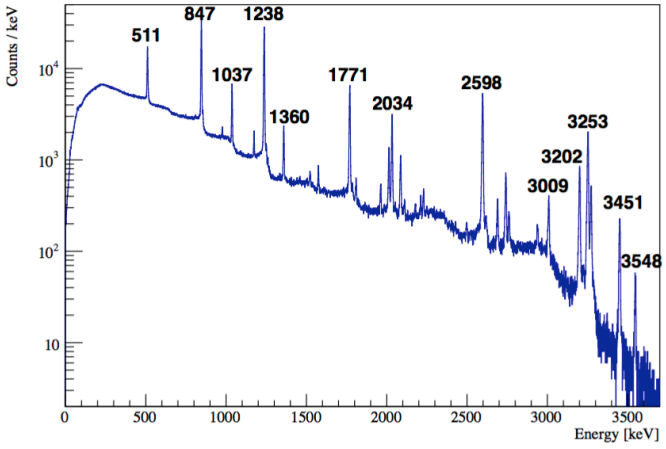

Figure 6.5: ^{56}Co calibration energy spectrum.

the LF and HF dataset, respectively.

6.5.1 Average pulse response

Firstly the average pulse, which is an average of single pulses, was used to try to define the number of the time constants that describe the pulse.
The average pulse is built in order to minimize the noise effects and it is used in the optimum filter to evaluated the amplitude of the pulses. The optimum filter is given by the following formula:

$$H(\omega) = A\frac{S^*(\omega)}{N(\omega)}, \tag{6.21}$$

where A is a normalization factor, $S^*(\omega)$ is an ideal signal without noise (average pulse) and $N(\omega)$ is the noise power spectra evaluated on the baseline.
The average pulse is produced for each dataset using the 2615 keV calibration run events. The average pulse building is divided in two principal phases: pulse alignment and averaging. The time position of the pulse peak is measured for each event, after that the single peaks are aligned so that the maximum occurs in the same time position. Then the single pulses are linearly averaged with equal weighting, the maximum is given by the average of single pulse peaks. Generally the average pulse is obtained using a few hundred single pulses.
Since the noise effects are minimized in the average pulse, this makes it a good pulse sample to define the time constants that describe the shape.
The best fit of average pulses was obtained by the sum of five exponentials: two rise and three decay time constants. The first rise is equal to the RC filter time constant, that varies between [9,35] ms for the LF dataset and it varies between [6,21] ms for HF dataset. In figure 6.6 an example of fit on an average pulse is shows. On the left a standard CUORE-0 average pulse, on the right the high frequency Bessel average pulse of the same channel. The

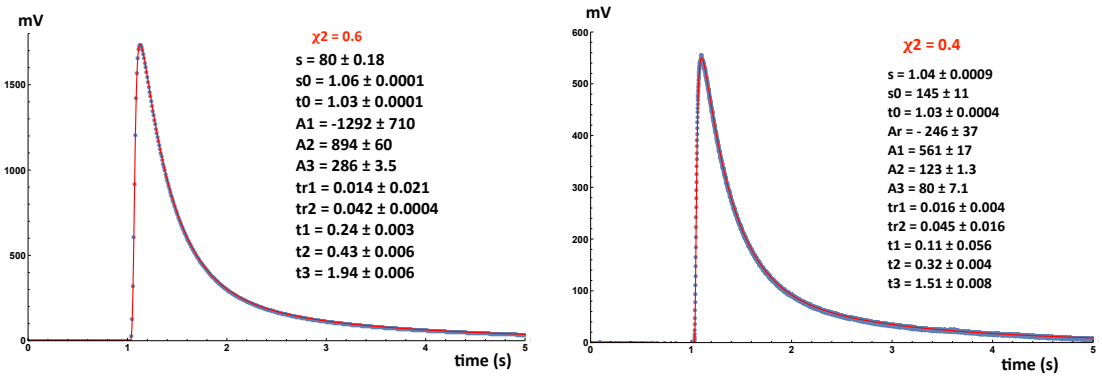

Figure 6.6: Fit of average pulses: low bessel frequency case on the left and high bessel frequency case on the right.

fit model does not describe well the first part of the pulse: this mismatch is more evident in the pulse acquired in the LF dataset(see fig. 6.7(a)) than in the one acquired in the HF dataset(see fig. 6.7(b)).

The conclusion is that this fit function is not a good model for all CUORE-

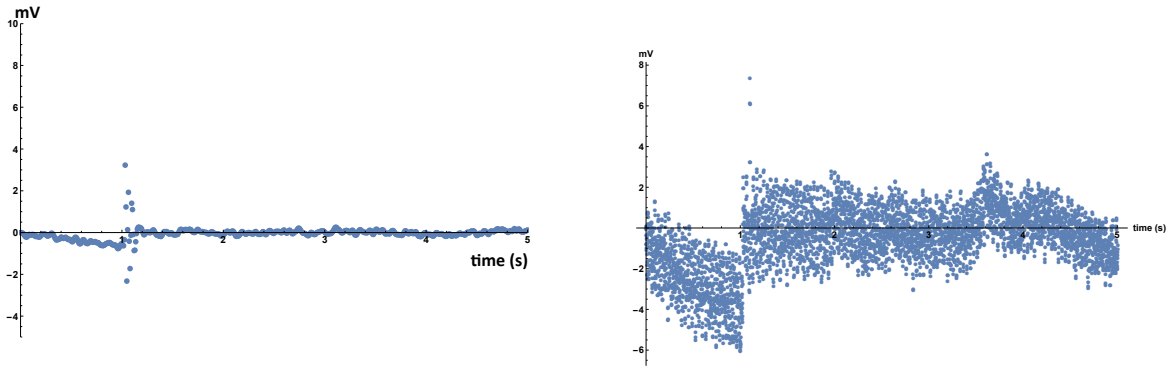

(a) (b)

Figure 6.7: Fit residuals of the pulses shown in figure 6.6.

0 crystals. In some crystals the mismatch on the rise is quite large (see fig. 6.8), while in other crystals, in which the RC time constant is higher than 20 ms, the fit program has problems to converge.

The problems found in the average pulse modeling come from the average

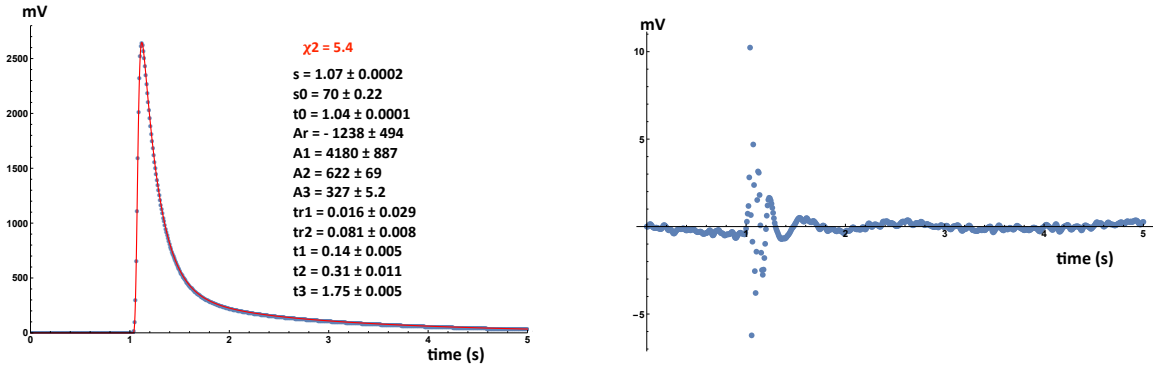

(a) (b)

Figure 6.8: Average pulse example for another CUORE-0 channel: in this case the mismatch on the rise is larger than the example of figure 6.6.

pulse itself. In fact it was built assuming that the single pulse shape is constant for a given bolometer, but pulse shapes are slightly different, as it shown in figure 6.9. The different pulse shape could be seen looking at the

long decay time estimation, that is 1.30 ± 0.009 s in one case (blue one) and it is 2.19 ± 0.015 s in another case (red one).

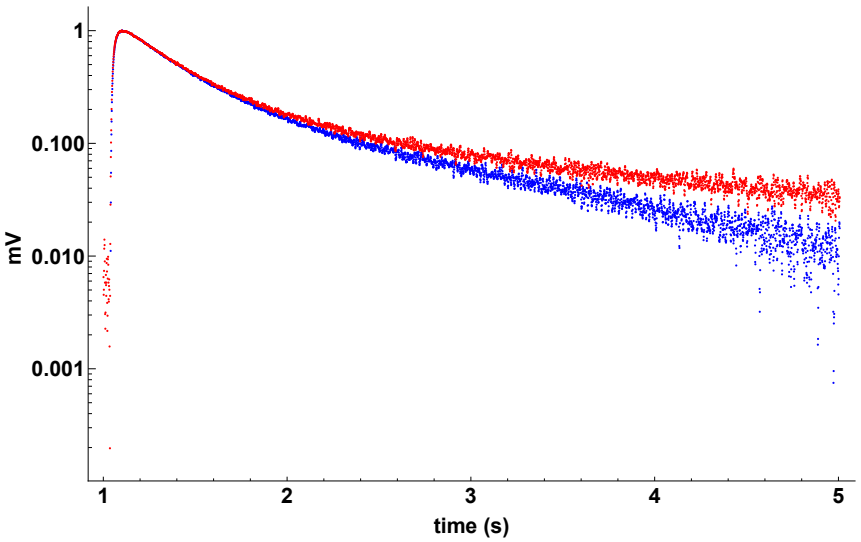

Figure 6.9: Two examples of individual pulse for the same channel. They have different long decay time.

6.5.2 Individual pulse response

Since the average pulse showed not to be a good pulse sample, the modeling was subsequently done on individual pulses but an additional problem appeared, namely the number of exponentials needed to fit a pulse is different in the LF and in the HF datasets.
The pulses acquired in the LF dataset are better described by a sum of four exponentials, one rise plus three decays. On the other hand the pulses acquired in HF dateset are well described by a sum of three exponentials. The three and four exponentials fit on a single pulse are shown in figures 6.10(a) and 6.10(b) for LF pulse and in figure 6.11(a) and 6.11(b) for HF pulse.
The fit residuals plots (see fig. 6.12 and fig. 6.13) show that the additional time constant improves the fit quality at low Bessel cutoff frequency, while it is not necessary at high Bessel cutoff frequency. The additional time constant is produced by Bessel distortion effects that are more relevant at low Bessel cutoff frequency, as it has been proved by simulation.

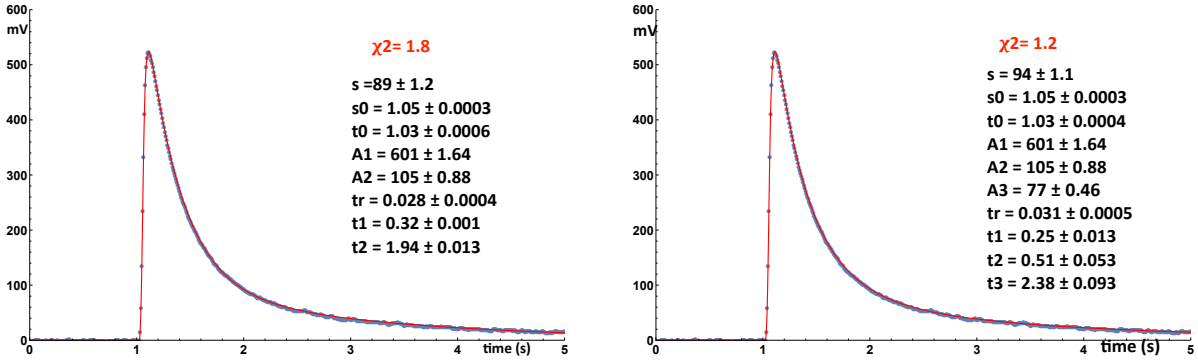

(a) (b)

Figure 6.10: Three (a) and four (b) exponentials fit at low Bessel cutoff frequency.

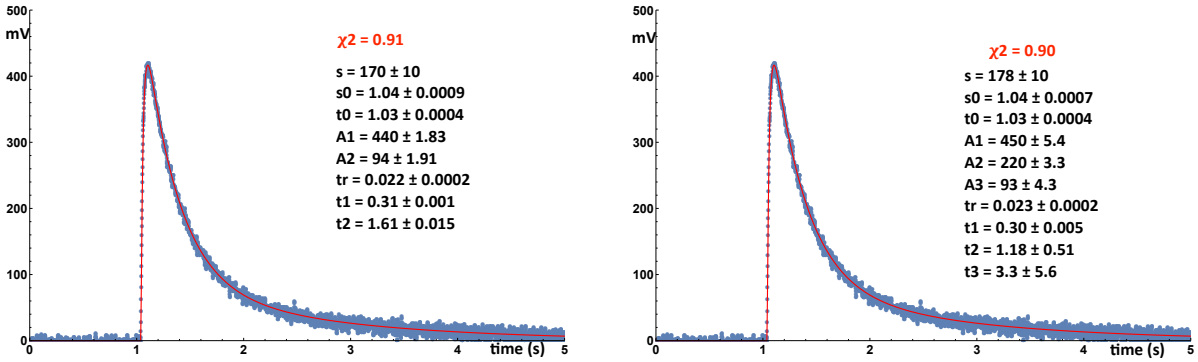

(a) (b)

Figure 6.11: Three (c) and four (d) exponentials fit at high Bessel cutoff frequency.

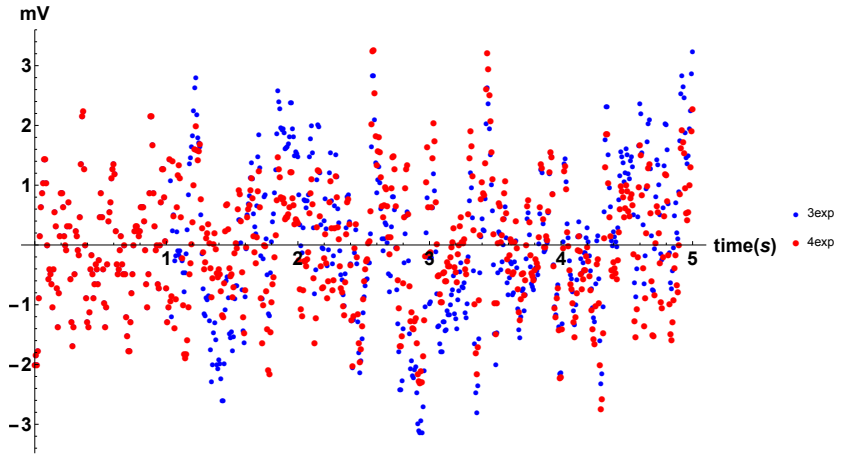

Figure 6.12: Comparision between three and four exponentials fit residuals at low bessel cutoff frequency.

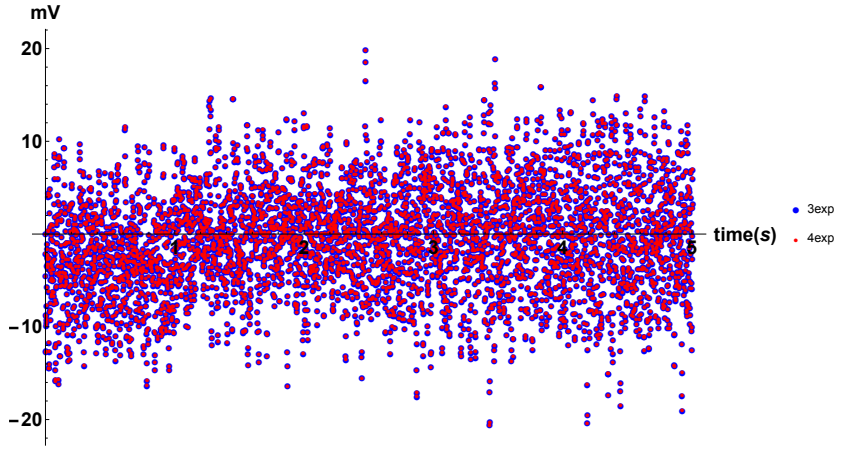

Figure 6.13: Comparision between three and four exponentials fit residuals at high bessel cutoff frequency.

6.5.3 Pulse simulation

A typical CUORE-0 pulse was simulated in order to better understand the additional time constant observed at low Bessel cutoff frequency.
The simulated pulse was constructed by a sum of three exponentials, one rise plus two decays:

$$A_1 exp\left[-\frac{t-t_0}{t_1}\right] + A_2 exp\left[-\frac{t-t_0}{t_2}\right] - (A_1+A_2)\left[-\frac{t-t_0}{t_r}\right]. \qquad (6.22)$$

The parameters are:

- the two pulse amplitudes: $A_1 = 1500$ mV, $A_2 = 900$ mV;
- the trigger time: $t_0 = 1.03$ s;
- the rise time: $t_r = 0.10$ s;
- the two decay time: $t_1 = 0.40$ s, $t_2 = 1.00$ s.

The simulated pulse function was convoluted with discrete 6-poles Bessel function (with sampling frequency of 125 Hz) for both Bessel cutoff frequencies, 12 Hz and 120 Hz. The RC filter effects were neglected in the simulation.
At high Bessel frequency the pulse distortion is reduced (see fig. 6.14(a) and fig. 6.14(b)).

The simulated pulses were fitted using the sigmoid function. An addi-

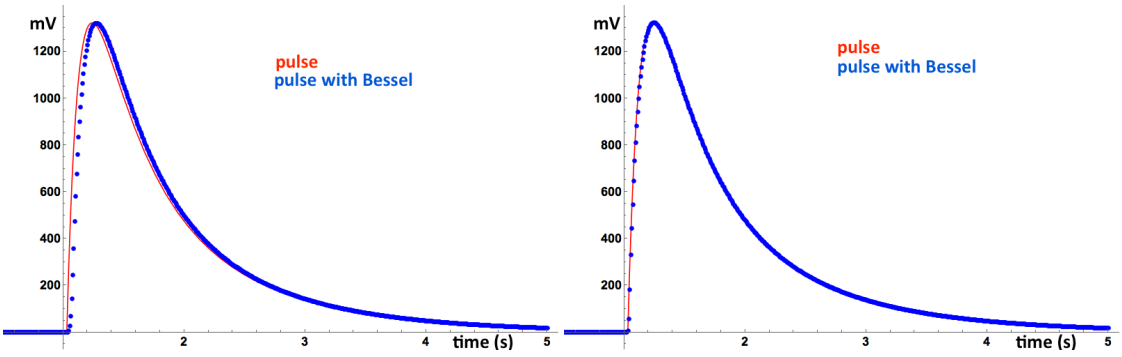

(a) (b)

Figure 6.14: On the left a simulated pulse filtered with low Bessel cutoff frequency. On the right a simulated pulse filtered with high Bessel cutoff frequency.

tional decay time constant was also observed in the pulse simulated at 12 Hz Bessel frequency (see fig. 6.15), as in the individual pulse fit. This time constant improves the fit quality, especially in the first part of the pulse (see

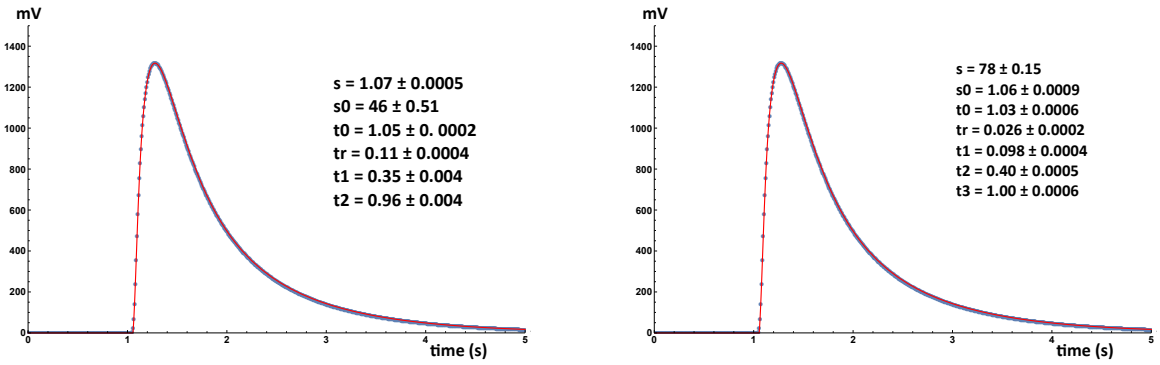

(a) (b)

Figure 6.15: Three (a) and four (b) exponentials fit on simulated pulse at low bessel cutoff frequency.

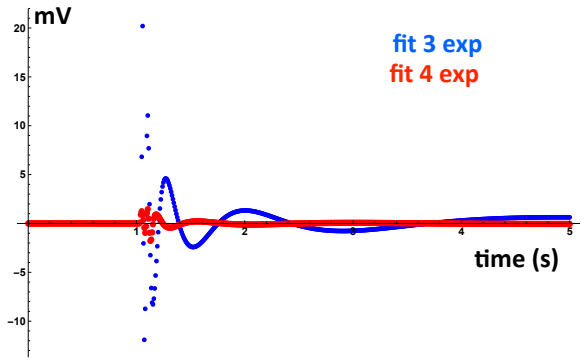

Figure 6.16: Fit residuals for low bessel cutoff frequency: in blue the three exponentials fit residuals and in red the four exponentials fit residuals.

fig. 6.16). On the contrary, the fit on pulse simulated at 120 Hz gives the right number of time constants (see fig. 6.17). Two time constants (t_r and t_1) are equal in the four exponentials fit.

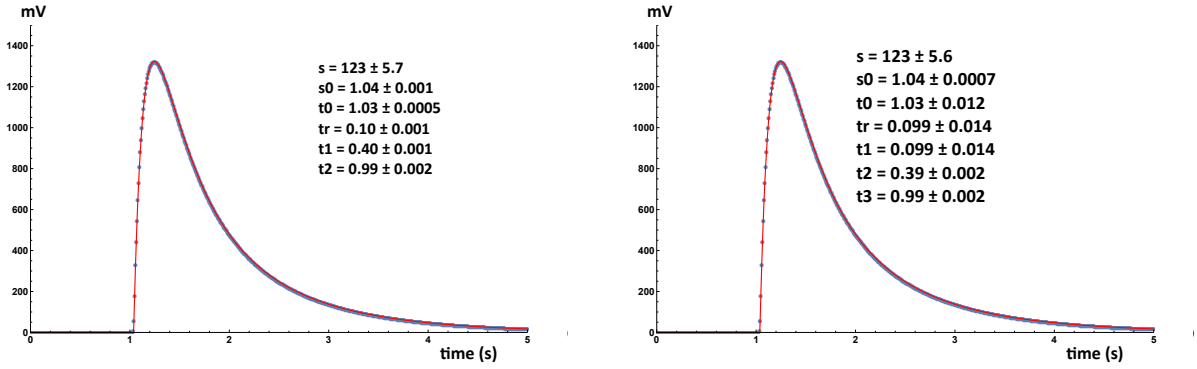

(a) (b)

Figure 6.17: Three (a) and four (b) exponentials fit on simulated pulse at high bessel cutoff frequency.

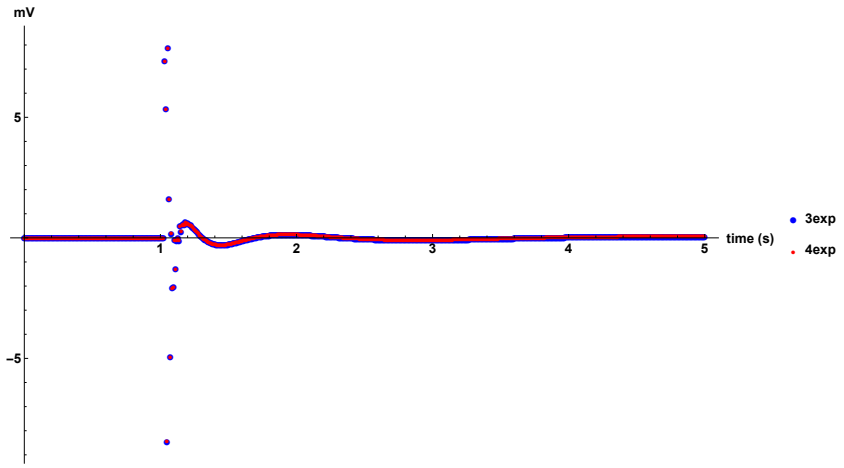

Figure 6.18: Fit residuals for low bessel cutoff frequency: in blue the three exponentials fit residuals and in red the four exponentials fit residuals.

6.6 RC filter effect

The individual pulse shape analysis shows that electronic effects could falsify the identification of the right number of time constants, i.e. the effective number of heat capacities. Therefore we investigated also the effects of the RC filter. The RC effect on the pulse shape is different for each crystal because its cutoff frequency depends on the working point resistance. The value of working points are different for each crystal and each dataset.
In figures 6.19(a) and 6.19(c) the fit for a specific channel (channel 31) with and without RC filter are shown. The pulse shape is described by a sum of three exponentials in both cases. The convolution between the RC filter and the pulse shape function does not improve the fit quality (see fig. 6.19(b) and fig. 6.19(d)) and the estimation of time constant is the same for both fits. This is compatible with the fact that in some channel the RC filter has a negligible effect since their working resistance were low enough (R varies between 10 and 25 $M\Omega$).

6.7 The simplified fit function

The preliminary results of pulse shape analysis of CUORE-0 response have shown:

- a fake time constant produced by pulse distortion at low Bessel cutoff frequency; as a consequence the data acquired in standard conditions are not good for the modeling;
- events on the same crystal have different pulse shapes, so the average pulse is not a good description because the contribution of different pulse shapes could be induce fake time constants;
- the RC filter is a negligible effects for channels in which their NTD sensor have a working point resistance between 10 and 25 $M\Omega$;

Since the aim of pulse shape analysis is the identification of the right number of time constants, a specific channel, Channel 31, characterized by low noise and in which effect due to the RC filter can be neglected for both dataset, was chosen ($R = 19$ $M\Omega$ for LF dataset and $R = 12$ $M\Omega$ for HF dateset).
Therefore a sample of 20 events of Channel 31 was fitted using a simplified fit function:

$$\frac{1}{1+exp[-s(t-s_0)]}\cdot\left[A_1 exp\left[-\frac{t-t_0}{t_1}\right]+A_2 exp\left[-\frac{t-t_0}{t_2}\right]+...-(A_1+A_2+...A_n)\left[-\frac{t-t_0}{t_r}\right]\right] \tag{6.23}$$

In figures 6.20 and 6.21 an example of fit with the simplified fit function on a single pulse of Ch31 is reported. The pulse shape is described by a sum

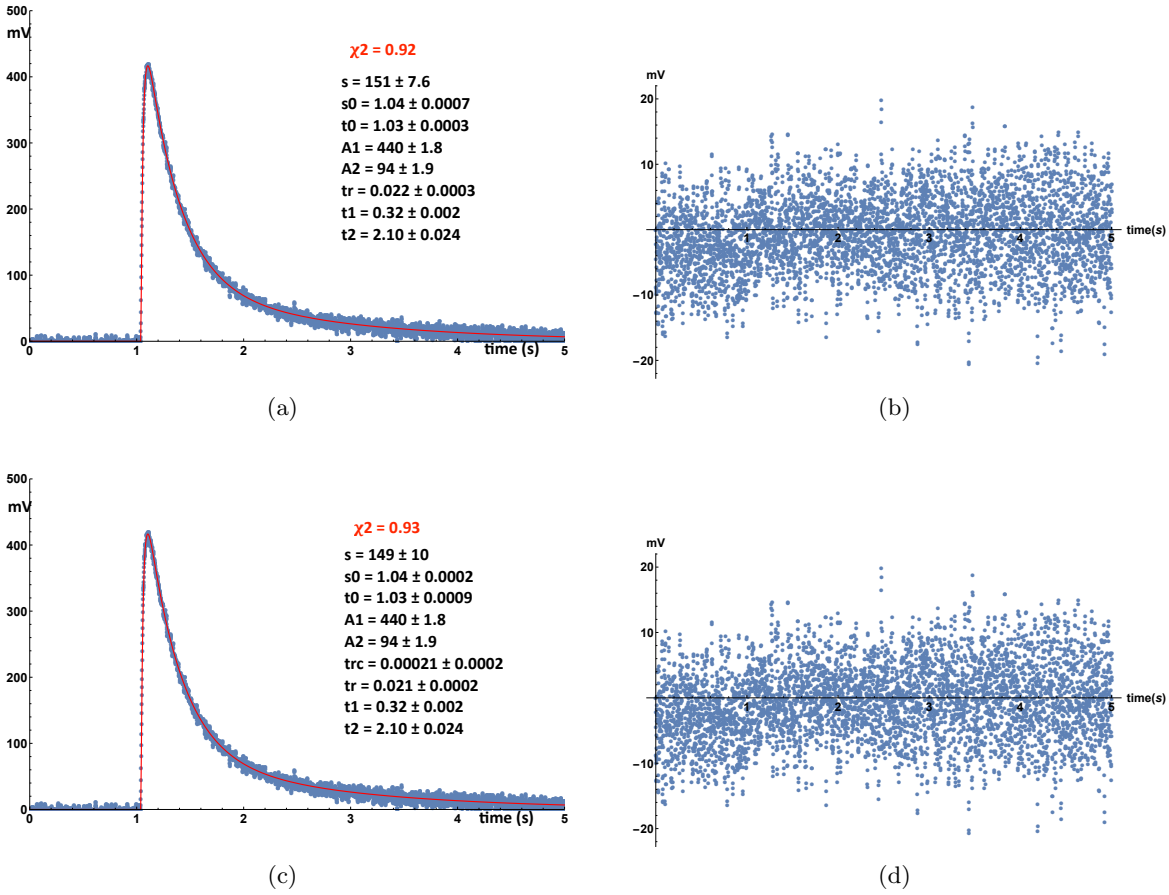

Figure 6.19: Fit without RC filter (a) and fit with RC filter (c). Residuals plot of fit with RC (b) and without RC (d), the convolution between pulse shape function and RC filter function does not improve the fit quality.

of four exponentials at 12 Hz Bessel cutoff frequency, the fake time constant is observed in all pulses of the sample. On the contrary the pulse shape is described by a sum of three exponentials at 120 Hz Bessel cutoff frequency.

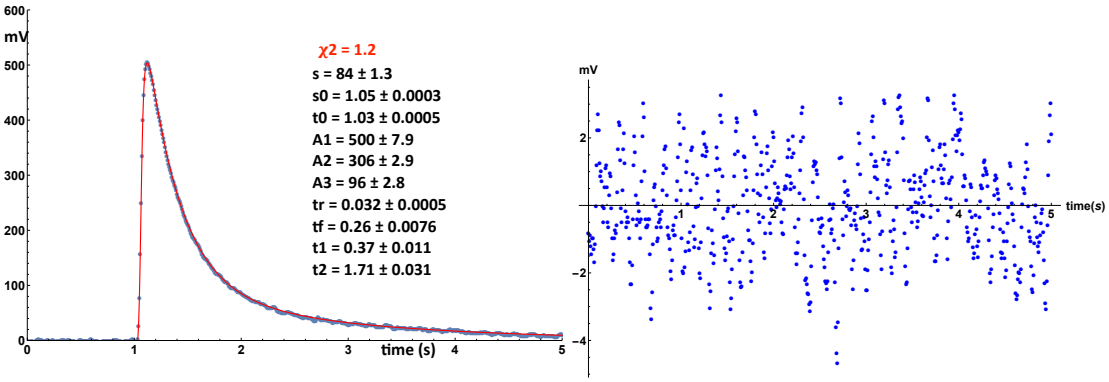

Figure 6.20: Simplified fit at low bessel cutoff frequency.

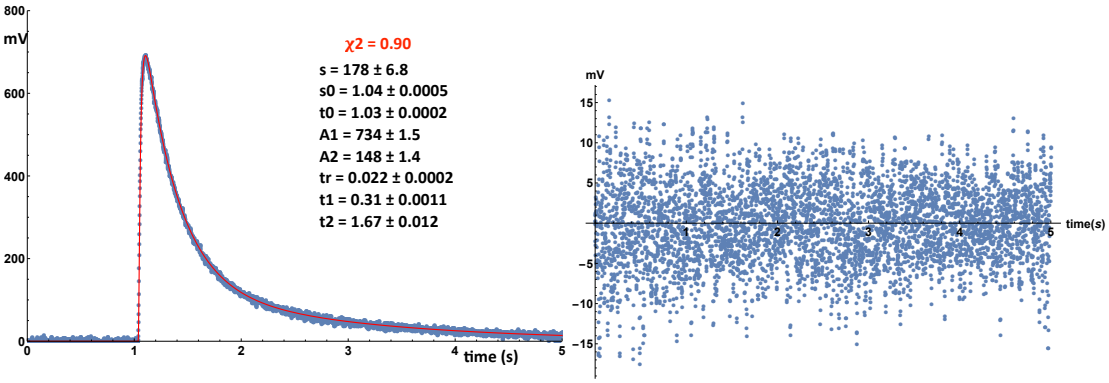

Figure 6.21: Simplified fit at high bessel cutoff frequency.

6.7.1 Time constants distributions

The time constants distributions obtained in the LF sample and in the HF sample are shown in figures 6.22. In yellow the time constant obtained for HF sample and in blue the ones for the LF sample.

In table 6.1 the mean values of time constants obtained for a sample of 20 single pulses sample are reported.

The Bessel cutoff frequency influenced the estimation of rise time, that is 34 ms in one case (LF) and 23 ms in the other case (HF). It is evident that the pulse rise is influenced by the Bessel cutoff frequency (see fig. 6.22(a)).

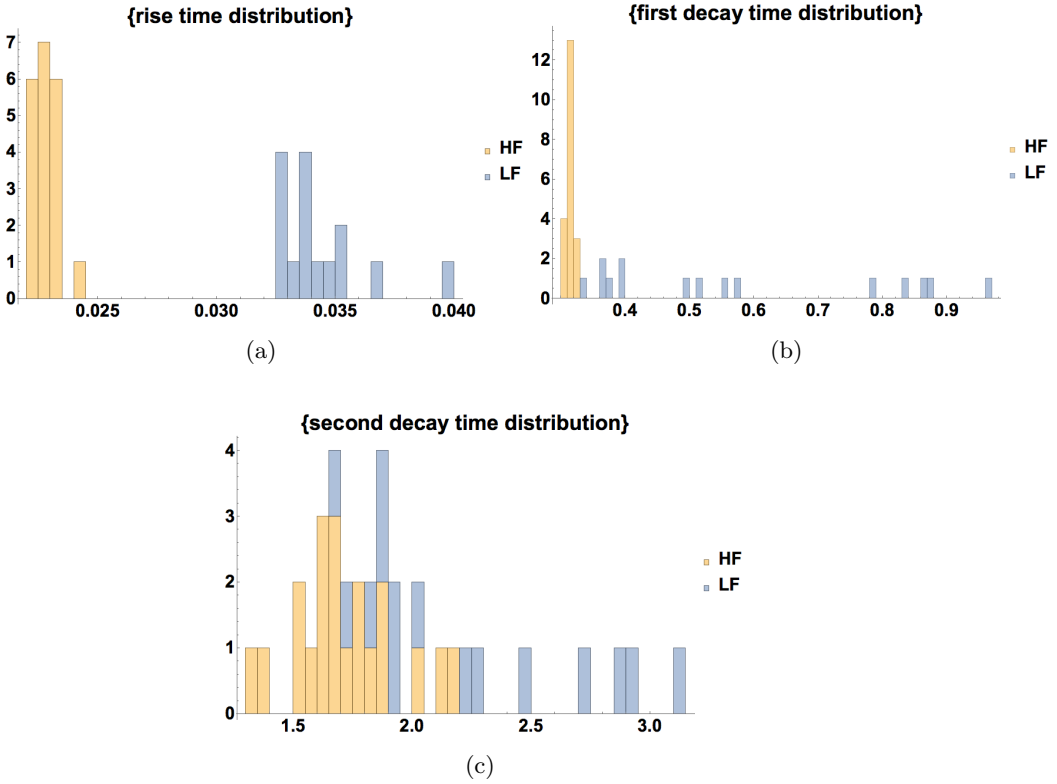

(a) (b) (c)

Figure 6.22: Comparison between rise time, first and second decay time constant for both datasets. In yellow the distribution for data acquired in LF dataset. In blue the distribution for data acquired in HF dataset.

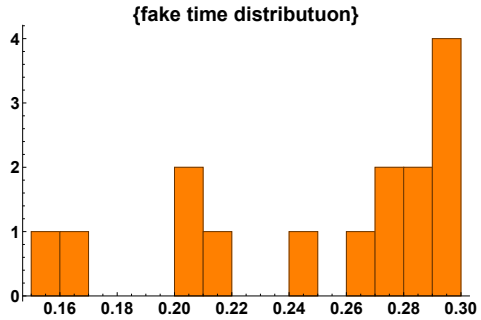

Figure 6.23: Fake time constant distribution.

DS	rise time (s)	t_1(s)	t_2(s)	t_f (s)
LF	0.034 ± 0.002	0.58 ± 0.22	2.22 ± 0.46	0.25 ± 0.05
HF	0.023 ± 0.0005	0.31 ± 0.006	1.71 ± 0.22	

Table 6.1: Mean value of time constants estimated for both datasets (HF/LF)

DS	s (1/s)	delay (s)
LF	93 ± 1.3	0.027 ± 0.002
HF	190 ± 24	0.005 ± 0.002

Table 6.2: Mean values of sigmoid parameter s and the delay, evaluated as $s_0 - t_0$, for both datasets (HF/LF).

The spread in the first decay time distribution is much larger in the LF dataset and this (see fig. 6.22(b)) depends on the presence of the fake time constant, which is distributed in a time interval of [0.15 -0.29] s(see fig. 6.23). The second decay time is distributed in a time interval of [1.3 - 2.2] s in HF acquisition and in [1.7 - 3.5] s in LF acquisition (see fig. 6.22(c)). The narrower time interval observed in HF acquisition depends on better sampling (1 kHz vs 125 Hz).

6.7.2 Sigmoid parameters distribution

The distributions of sigmoid parameters s and $s_0 - t_0$, are shown in figure 6.24. In yellow the result obtained in the LF dataset and in blue the result obtained in the HF dataset.
The mean values of s and the delay are reported in table 6.2.

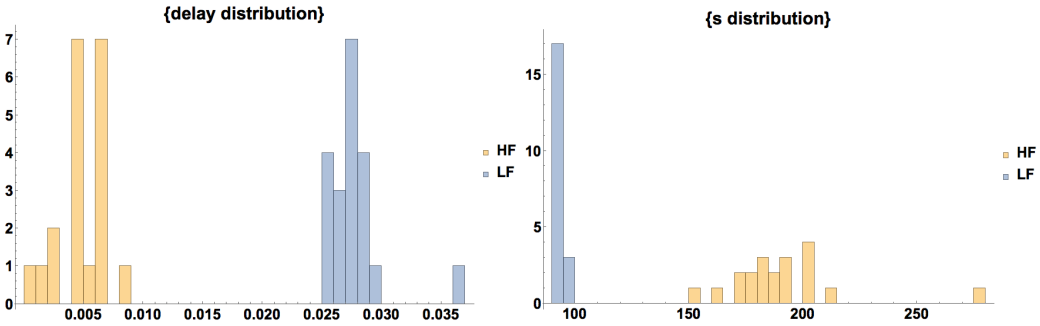

Figure 6.24: On the left the delay distribution obtained by the difference between the sigmoid parameter s_0 and the trigger time t_0. On the right the sigmoid parameter s that simulates the pulse distortion.

A high value of s corresponds to high Bessel cutoff frequency and a low value of s corresponds to low Bessel cutoff frequency.
The value of the delay and the s are in agreement with the simulation; at high Bessel cutoff the delay is of order of few ms and the pulse rise is not highly distorted (this mean a high value of s), as it is shown in figure 6.14.

6.7.3 Conclusion

In the pulse shape analysis of CUORE-0 pulses, the first approach was a full description of the response including the electronic chain effects. However the pulse distortion produced by Bessel filter and the RC effects on pulse rise could falsify the counting of time constants and the correct estimation of their value. Therefore the subsequent characterization was done on a specific CUORE-0 channel (Channel 31), in which the RC filter has a negligible effect and the noise is not dominant, using a simplified fit function in order to find the correct number of time constants.
The preliminary results show that the pulse shape is described by a sum of three exponentials, one rise plus two decays.
Since the Bessel effects are strongly reduced at high cutoff frequency and the RC filter is not negligible for all channel, the following pulse shape analysis was done on HF data using the simplified fit function on a specific subset of channels.

Chapter 7

Pulse shape analysis

7.1 Single pulse analysis

In the HF dataset half of the CUORE-0 channels were acquired with a Bessel cutoff frequency of 120 Hz and a sampling frequency of 1 kHz. The other ones were acquired in standard conditions.
Seven channels were selected to define and optimize the fit function model. The selected channels have been chosen in order to have a good representation of the different pulse shapes (see fig. 7.1) seen in CUORE-0 while keeping the working point resistance of their NTD in the range [10-25] $M\Omega$ to neglect the RC filtering effect (see table 7.1).

Ch	NTD_WP (MΩ)
28	14
30	13
31	12
33	12
41	25
45	14
51	11

Table 7.1: Selected channels in the pulse shape analysis.

The analyzed sample is given by all signal events acquired in a run calibrated by a ^{56}Co source. In figure 7.2 the amplitude spectrum (in ADC counts[1]) of the selected pulses, is shown. The pulse amplitude is estimated as the maximum of the pulse minus the value of the baseline, which is given by the mean value of the noise signal acquired in the pre-trigger time window

[1]The analysis is done on raw data and the pulse amplitude is expressed in ADC counts. The conversion factor from ADC to mV is ~ 0.08 mV/ADC count.

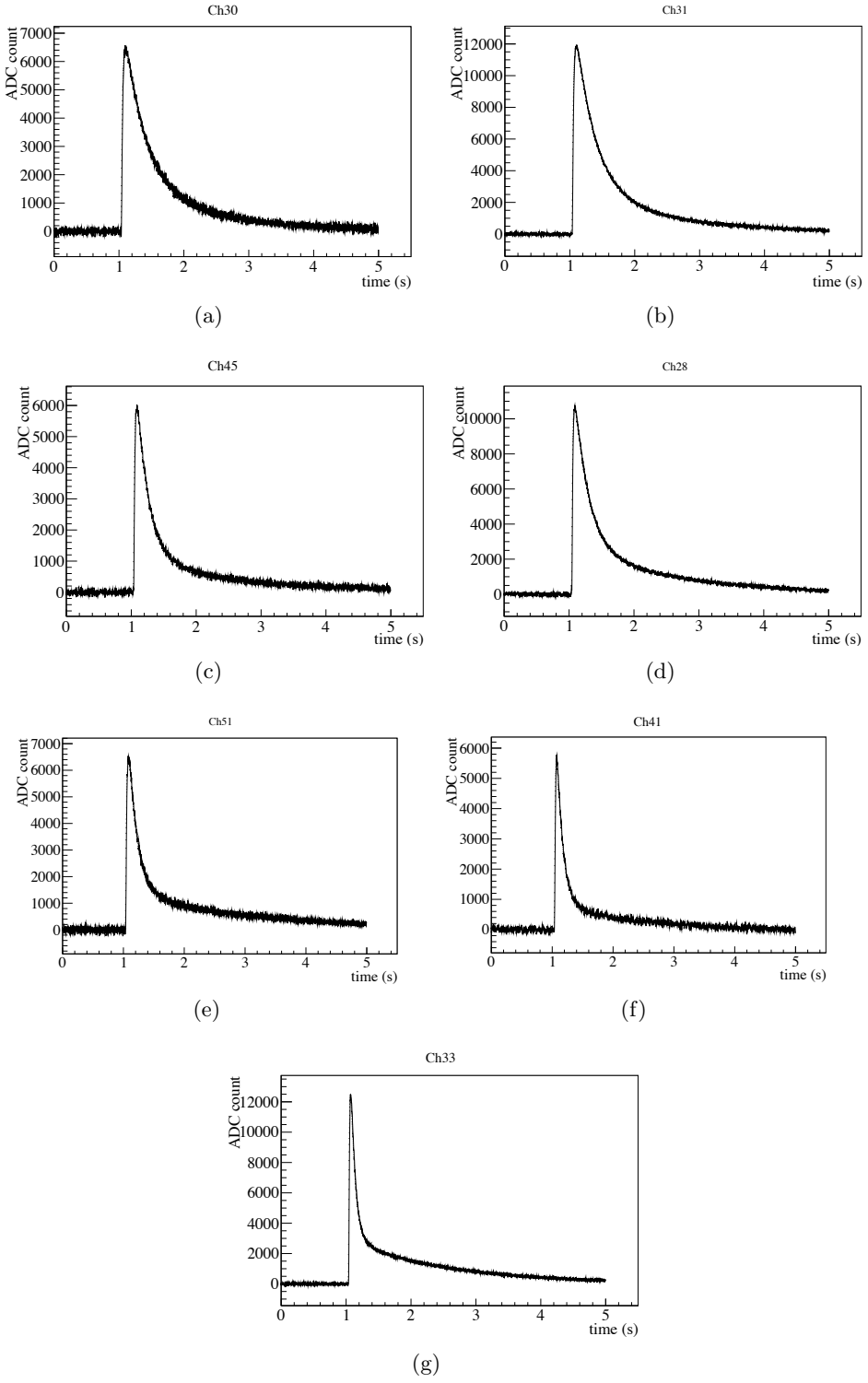

Figure 7.1: Pulse response of seven selected channels acquired in "ad hoc" configuration.

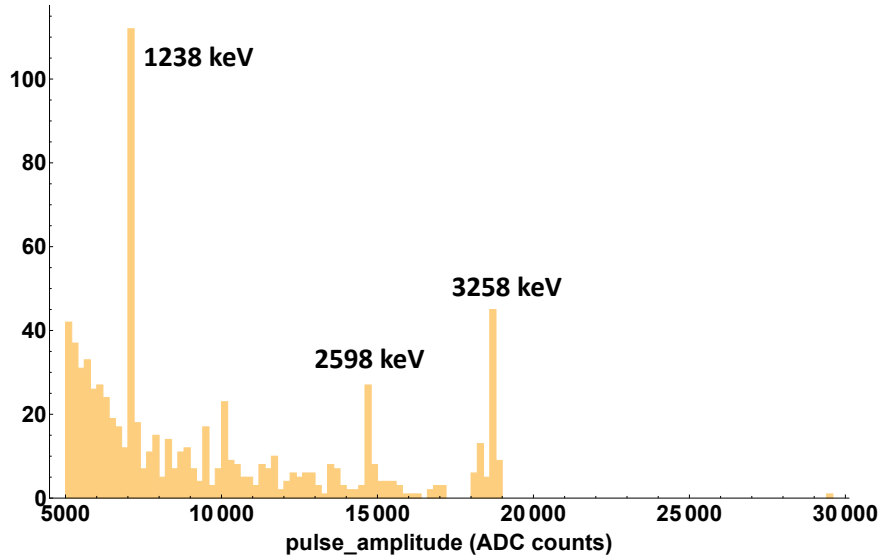

Figure 7.2: Pulse amplitude spectra of the analyzed events (channel 31).

($[0 - 1.0]$ s.).
The amplitude of pulses selected in the analysis is distributed in the range $[5000 - 20000]$ ADC counts and corresponds to a energy interval in the range [1 - 3.5] MeV. The lines at 8000, 15000 and 18000 corresponds to a energy of 1.2, 2.5 and 3.3 MeV, respectively. These lines represent the γs produced by ^{56}Co source. The pulses with amplitude above the 20000 ADC counts are mainly due to αs events with a corresponding energy around $4 - 5$ MeV.

A semi-automatic module was implemented to perform the pulse shape analysis with the following steps:

- get all signal events with amplitude above 5000 ADC counts;
- fit on all selected events;
- eliminate all pile-up events by cuts on the χ^2_{red} estimated by ROOT;
- re-evaluate the χ^2_{red}, introducing the RMS of the baseline, to determinate the fit quality;
- save all fits that have a χ^2_{red} between $[0.75 - 2.0]$.

ROOT estimates the χ^2_{red} setting the default error for each point, so it is not a good estimator for the goodness of the fit. The χ^2_{red} is re-evaluated by the following formula:

$$\chi^2_{red} = \frac{(f_{pulse}(x_i) - y_i)^2}{RMS^2 \cdot n.d.g}, \tag{7.1}$$

where $(f_{pulse}(x_i) - y_i)$ are the fit residuals, the RMS is estimated in the pre-trigger time window and represents the noise of the single channel, the degree of freedom is 5000 (the total pulse points are 5008 and the fit parameters are 8).
However the ROOT χ^2_{red} is a good variable to distinguish the signal events by the pile-up events. Some fits on events of Ch31 are reported, as an example in figure 7.3. Most of them are pile-up events. The ROOT χ^2_{red} is between $[19000 - 4.1 \times 10^6]$ for all pile-up events, while the only good event has a ROOT χ^2_{red} of 4394, which correspond to a re-evaluated χ^2_{red} of 1.1. A cut on the ROOT χ^2_{red} is imposed in the ROOT macro to select only the events containing a single pulse. In the case of Ch31, it imposed that the ROOT χ^2_{red} is under 7000. In figure 7.4 the macro response with the cut is shown. The fit examples in figure 7.4 have a re-evaluated χ^2_{red} of 1.0, 0.9, 1.4, 1.0, 1.5, respectively.

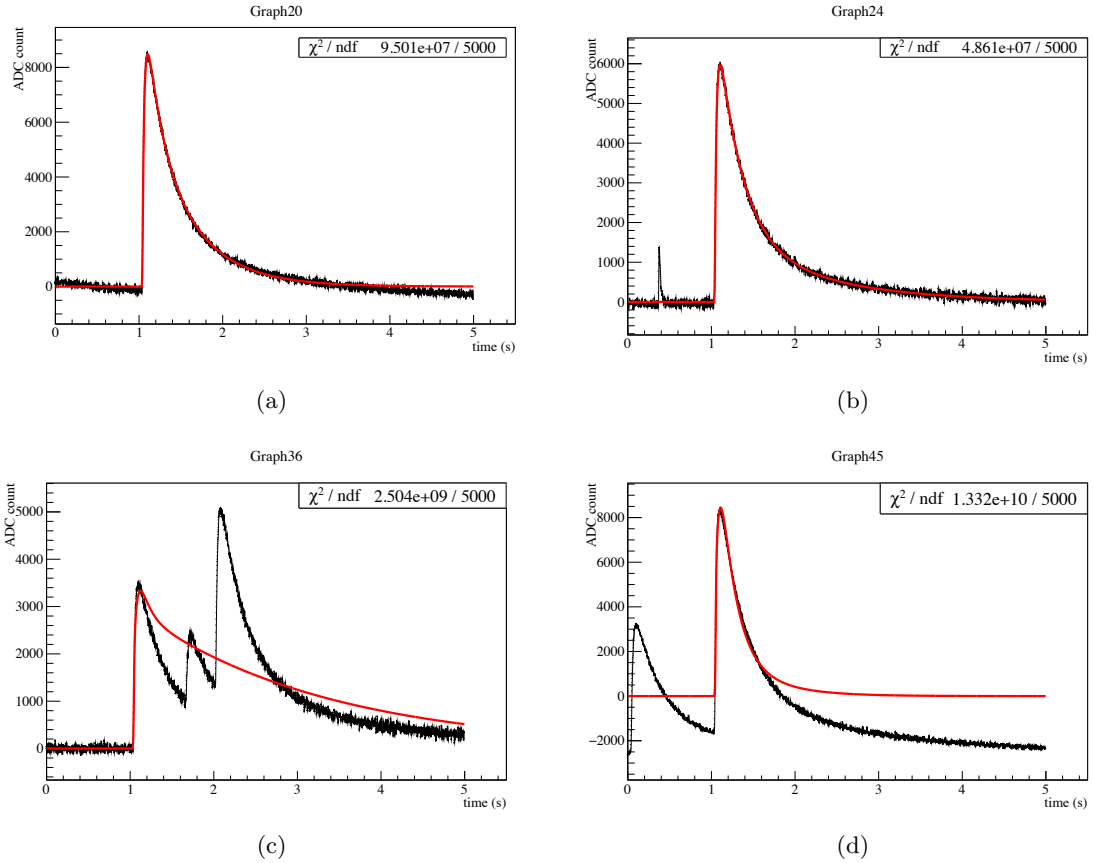

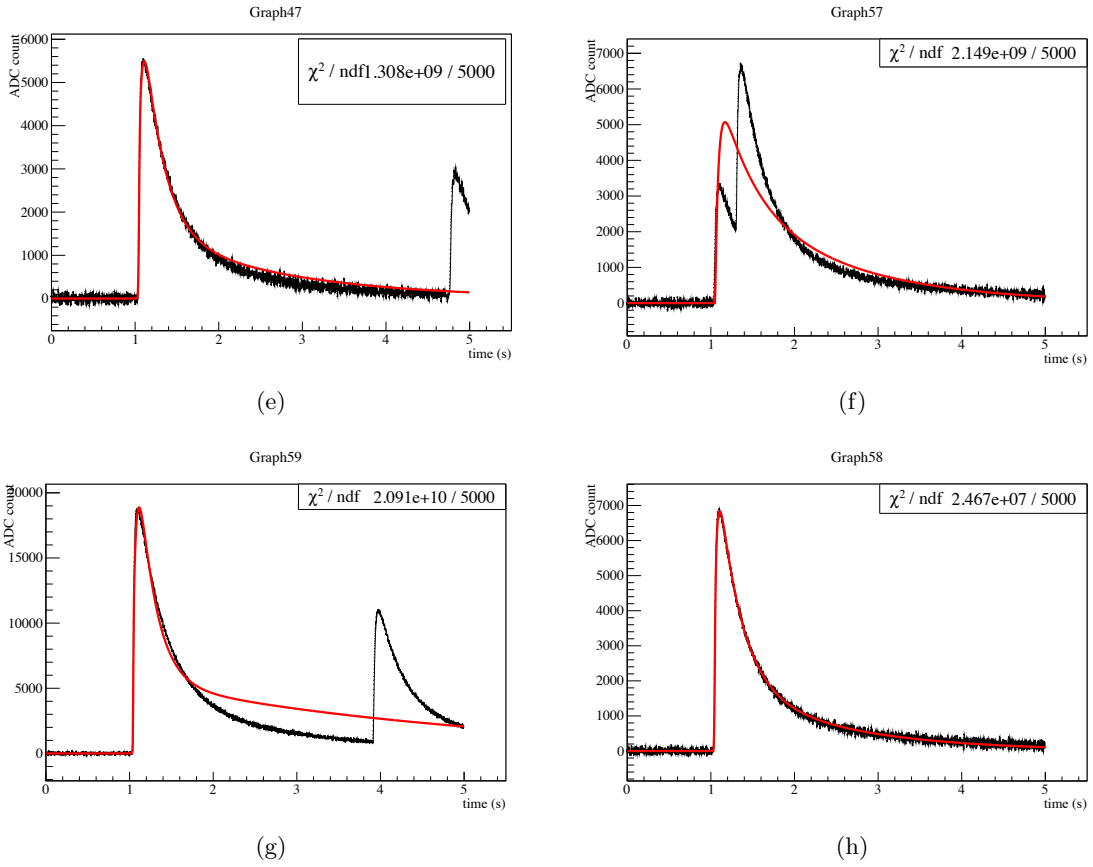

(e) (f)

(g) (h)

Figure 7.3: Examples of fit performed without any cut on the χ^2_{red}.

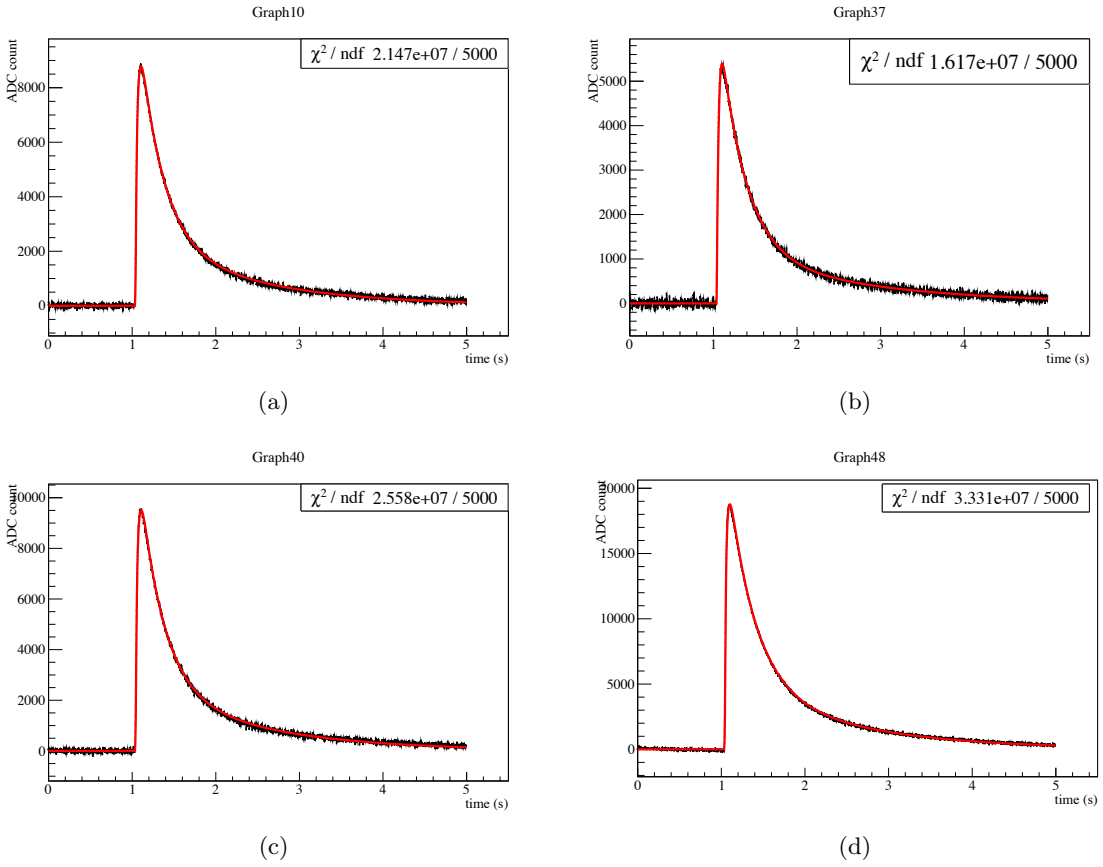

Figure 7.4: Selected fits with cut on the χ^2_{red}.

7.1.1 CUORE-0 bolometer response

In figure 7.5 examples of fits performed on the seven selected channels are shown. The χ^2_{red} is between $[0.93 - 1.5]$. The used fit function is:

$$\frac{1}{1+exp[-s(t-s_0)]} \cdot \left[A_1 exp\left[-\frac{t-t_0}{t_1} \right] + A_2 exp\left[-\frac{t-t_0}{t_2} \right] - (A_1 + A_2)\left[-\frac{t-t_0}{t_r} \right] \right]. \tag{7.2}$$

The three time constants that describe the CUORE-0 pulses correspond to three dominant heat capacities. The next step has been to define the corresponding heat capacity and to understand the different pulse shapes, which seem related to a different first decay time (see fit of Ch30 and Ch33, the first decay time is 0.35 s and 0.071 s, respectively).

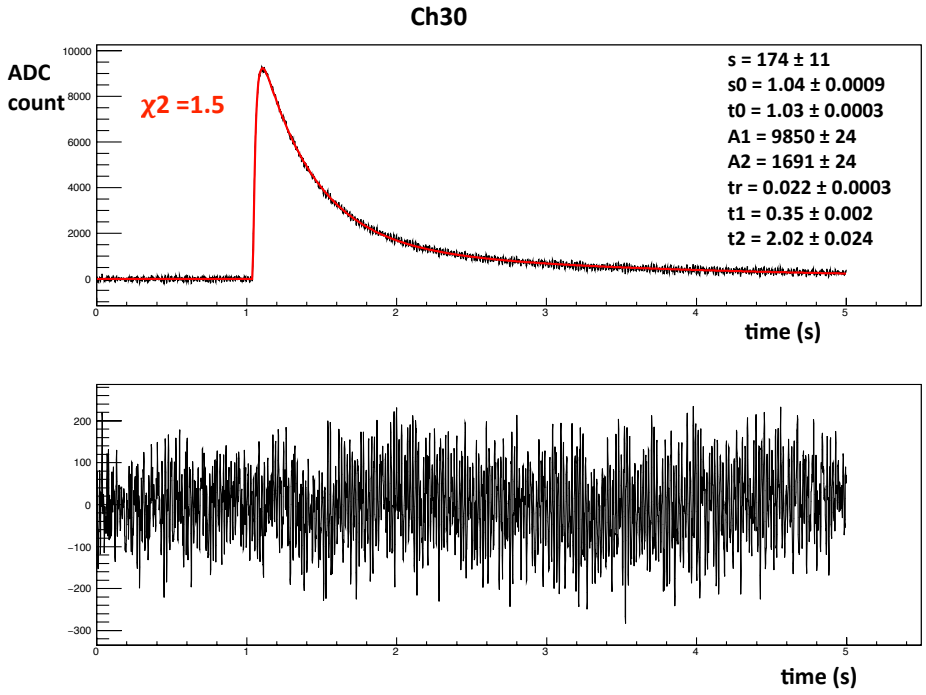

(a)

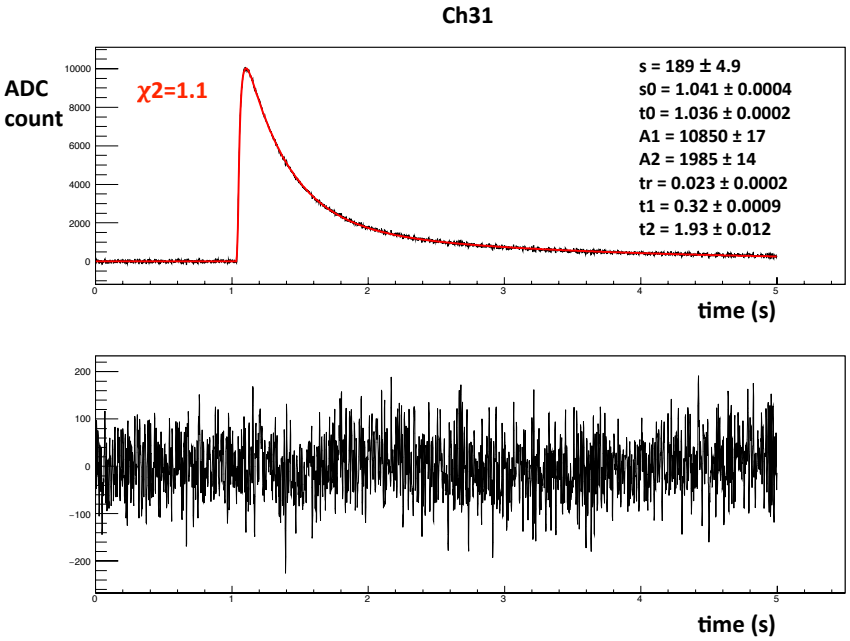
Ch31
ADC count
χ2=1.1
s = 189 ± 4.9
s0 = 1.041 ± 0.0004
t0 = 1.036 ± 0.0002
A1 = 10850 ± 17
A2 = 1985 ± 14
tr = 0.023 ± 0.0002
t1 = 0.32 ± 0.0009
t2 = 1.93 ± 0.012
time (s)
time (s)

(b)

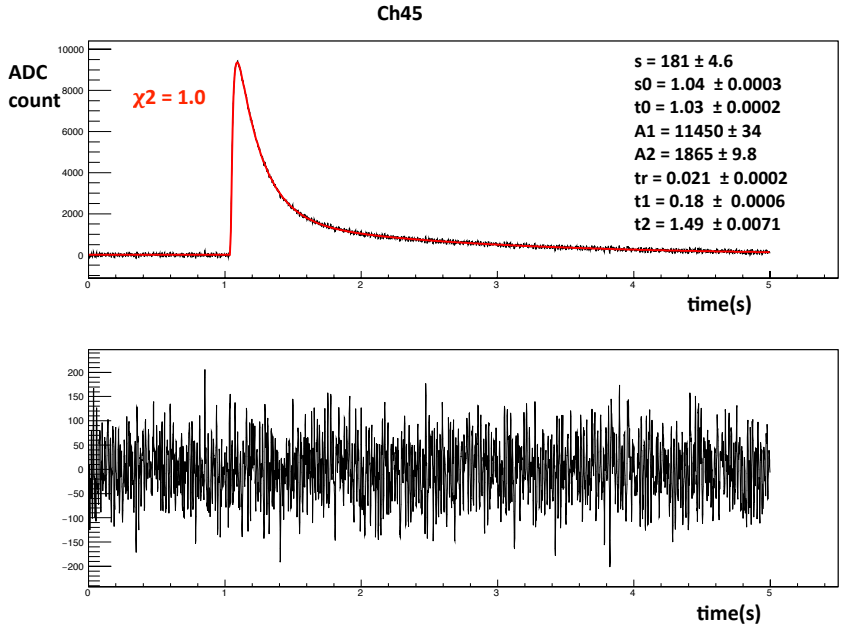
Ch45
ADC count
χ2 = 1.0
s = 181 ± 4.6
s0 = 1.04 ± 0.0003
t0 = 1.03 ± 0.0002
A1 = 11450 ± 34
A2 = 1865 ± 9.8
tr = 0.021 ± 0.0002
t1 = 0.18 ± 0.0006
t2 = 1.49 ± 0.0071
time(s)
time(s)

(c)

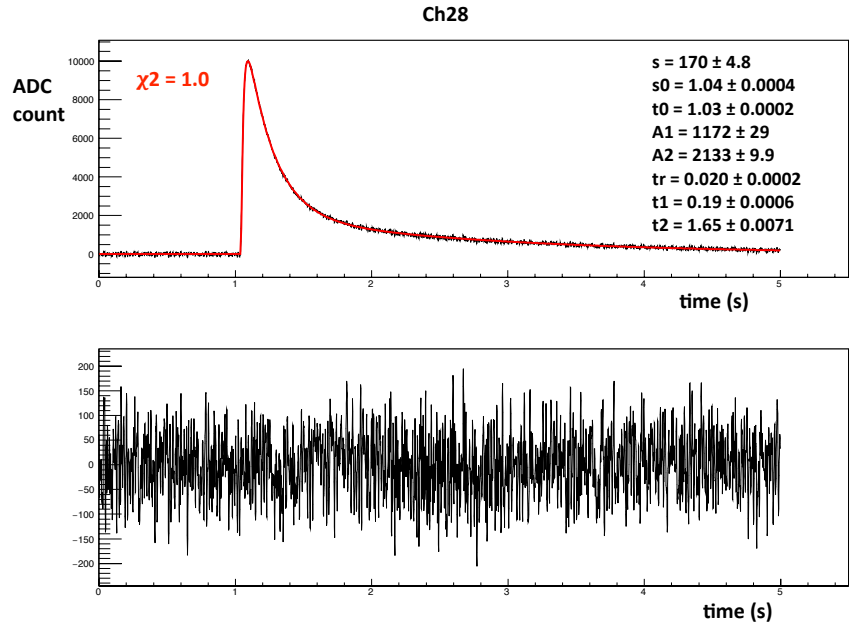
Ch28
ADC count
χ2 = 1.0
s = 170 ± 4.8
s0 = 1.04 ± 0.0004
t0 = 1.03 ± 0.0002
A1 = 1172 ± 29
A2 = 2133 ± 9.9
tr = 0.020 ± 0.0002
t1 = 0.19 ± 0.0006
t2 = 1.65 ± 0.0071
time (s)
time (s)

(d)

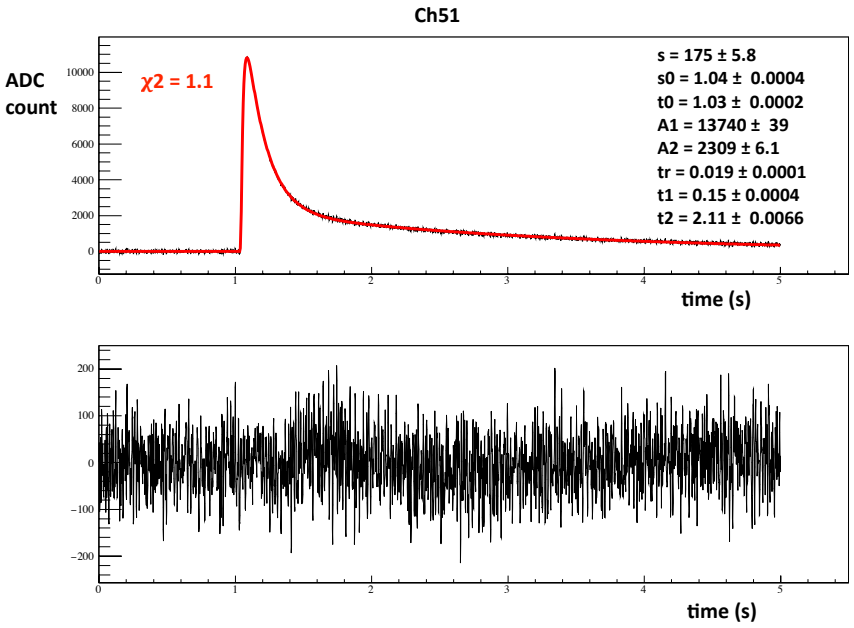
Ch51
ADC count
χ2 = 1.1
s = 175 ± 5.8
s0 = 1.04 ± 0.0004
t0 = 1.03 ± 0.0002
A1 = 13740 ± 39
A2 = 2309 ± 6.1
tr = 0.019 ± 0.0001
t1 = 0.15 ± 0.0004
t2 = 2.11 ± 0.0066
time (s)
time (s)

(e)

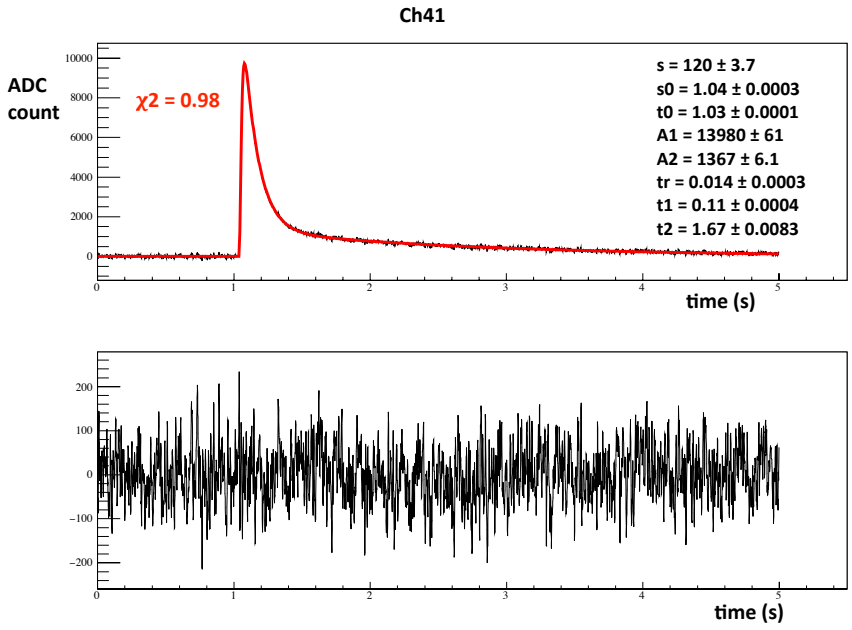

(f)

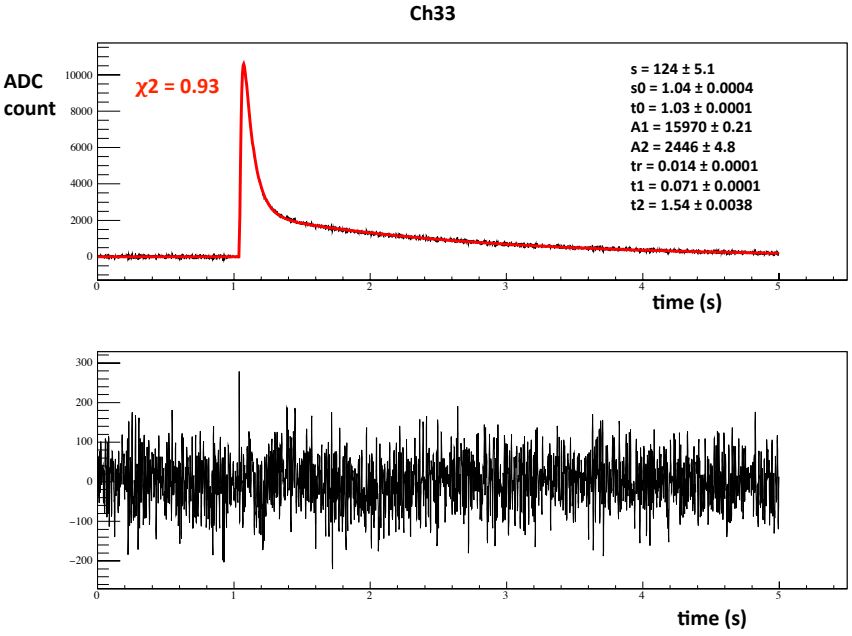

(g)

Figure 7.5: Fit and fit residuals on the selected channels.

7.1.2 Time constants distributions

The time constants distributions are shown in figure 7.6 and the mean values are reported in table 7.2.

Ch	$t_r(ms)$	$t_1(s)$	$t_2(s)$
30	23.3 ± 1.1	0.327 ± 0.019	1.44 ± 0.25
31	23.1 ± 0.8	0.311 ± 0.014	1.69 ± 0.28
45	20.1 ± 0.7	0.185 ± 0.006	1.60 ± 0.22
28	20.1 ± 0.8	0.195 ± 0.006	1.64 ± 0.21
51	19.4 ± 1.4	0.146 ± 0.005	1.98 ± 0.29
41	14.0 ± 1.4	0.105 ± 0.004	1.62 ± 0.27
33	13.5 ± 0.8	0.071 ± 0.001	1.57 ± 0.12

Table 7.2: Mean values and their errors of time constants.

The rise time of all channels is distributed in a time interval range [0.005 - 0.025] s, while the first decay time of all channel in [0.05 - 0.35] s. Each crystal has a different time interval for the rise time and especially for the first decay time.
The second decay time has a uniform distribution in the range [0.8 - 3.0] s for each crystal. Nevertheless it is the time constant which has the major uncertainty in its estimation.
Firstly a possible relation between the time constants and the NTD working point resistance was studied. In figure 7.7 the time constants as function of working point are reported. The time constant values seem to be independent of the NTD working point resistance.

The second hypothesis for the variability of the first time constant was a relation with a known platinum contamination of the TeO_2 crystals. This kind of contamination comes from the crucibles in which the TeO_2 bolometers were grown, as discussed in section 5.1.1.

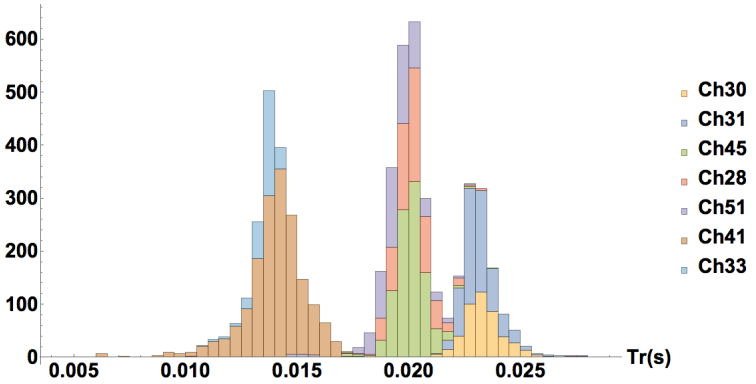

(a)

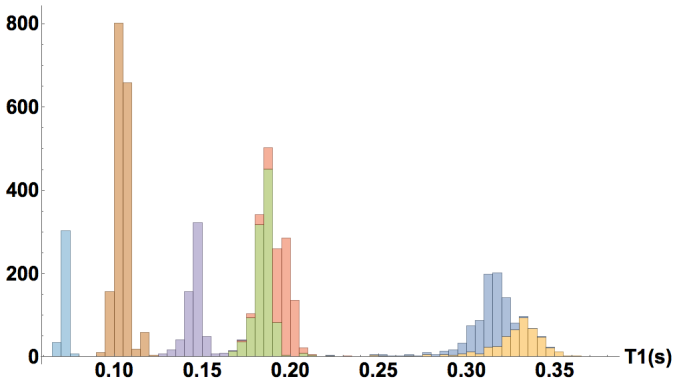

(b)

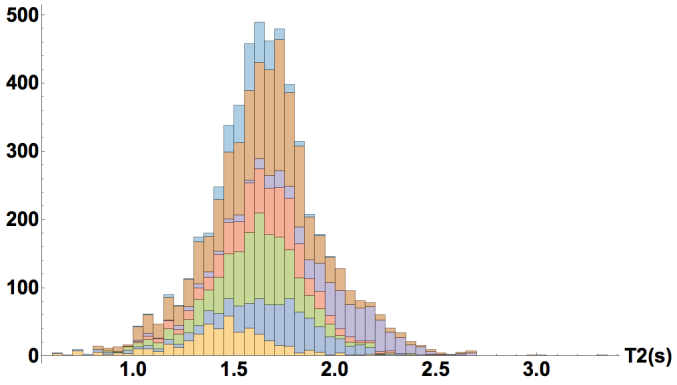

(c)

Figure 7.6: Time constants distributions: (a) rise time, (b) first decay time, (c) second decay time.

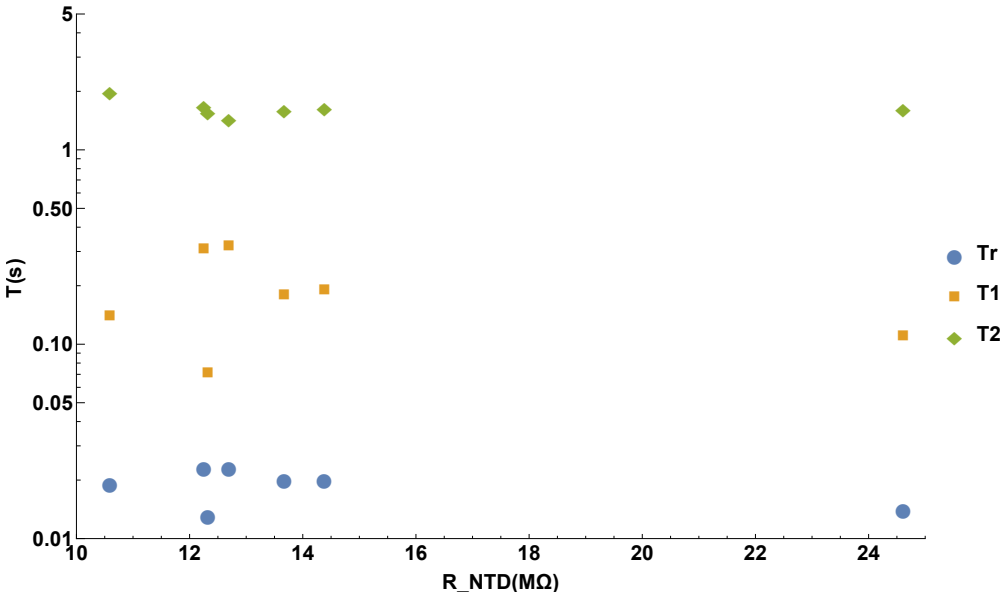

Figure 7.7: Time constants vs working point resistance.

7.2 Platinum contamination effects

Platinum contamination was observed by a peak centered at 3240 keV, which corresponds to the alpha decay of ^{190}Pt. In figure 7.8 the sum background spectra of all CUORE-0 channels in a energy interval of $[3200 - 3400]$ keV is shown. The platinum contamination is not diffused into the crystals, but there are fragments of the platinum crucible in the CUORE bolometers, so this contamination was not observed by ICMPS analysis of crystal samples.

Possibly platinum fragments of the crucible went into the crystal during their production process and the number of the fragments is different for each crystal. The platinum inside the crystal is metallic, so its heat capacity cannot be neglected. The value of platinum heat capacity depends on platinum mass in each crystal. This number is estimated by the counts in the background spectra in an energy interval of $[3200 - 3400]$ keV for each crystal. In figure 7.9 the background spectra in the energy region of $[3200 - 3400]$ keV are shown for some crystals. In the CUORE-0 crystals the number of counts (entries in figure 7.9) ranges between 12 and 135 counts/yr..

The effective platinum contamination present into the crystals is estimated as the difference between the number of ^{190}Pt counts and the total α background counts in an energy interval of $[3200 - 3400]$ keV. The α background measured by CUORE-0 is (0.016 ± 0.001) $counts/(keV \cdot kg \cdot yr)$ in all α region (see section 3.3.1). The corresponding α background counts ($count\_bkg$) around ^{190}Pt peak is given by:

$$count\_bkg = 0.016 \times 200keV \times exposure(kg \cdot yr), \tag{7.3}$$

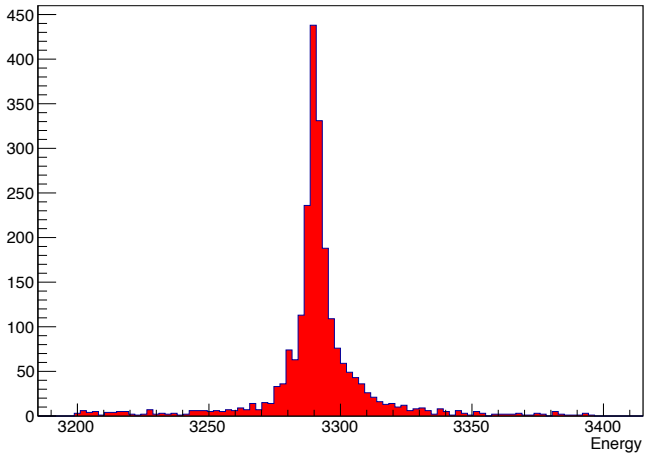

Figure 7.8: Sum background spectra for all CUORE-0 crystal in a energy interval of $[3200 - 3400]$ keV. The peak at 3240 keV is the Q-value of α decay of ^{190}Pt.

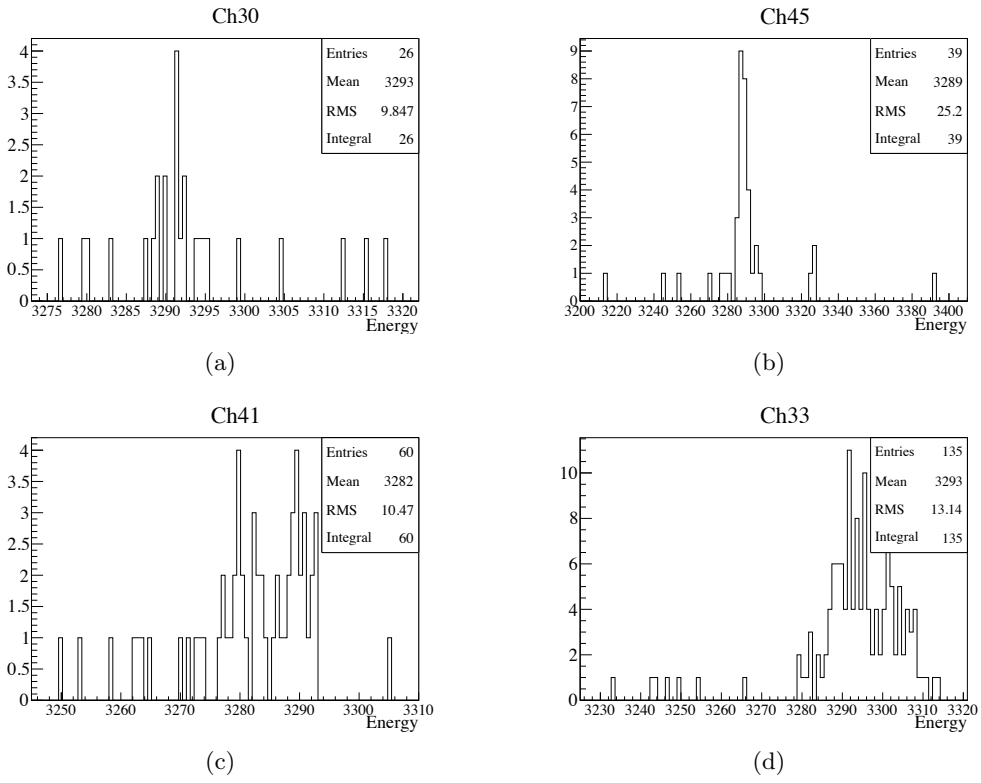

Figure 7.9: Energy spectra for some CUORE-0 channels with different platinum contamination.

where the 200 keV is the energy interval around the ^{190}Pt peak and the exposure is calculated for each crystal during CUORE-0 data-taking.
The effective ^{190}Pt contamination of a single channel is:

$$count\_Pt = count[3200 - 3400] - count\_bkg. \tag{7.4}$$

7.2.1 Platinum heat capacity

The platinum heat capacity of each crystal is given by the following equation:

$$C_{Pt} = n \cdot \gamma \cdot 10 \text{ mK} \tag{7.5}$$

where n is the number of moles of natural platinum and the γ coefficient is the molar specific heat of platinum at low temperature, $\gamma = 6.5 \times 10^{-3}$ $J/(mol \cdot K^2)$ [124].
The number of moles of natural platinum can be estimated from the ^{190}Pt contamination present in each crystal. The number of the decays is given by the following equation:

$$count\_Pt = N_0 \left(1 - exp\left[-\frac{t}{\tau}\right]\right), \tag{7.6}$$

where N_0 is the initial number of the ^{190}Pt atoms, t is the measurement live time, τ is the ^{190}Pt decay time.
The half-life of ^{190}Pt is $t_{1/2} = 6.5 \times 10^{11}$ yr [123] and since $t << \tau$, the number of decays can be expressed as:

$$count\_Pt = \frac{N_0 t}{t_{1/2}} ln2. \tag{7.7}$$

The number of initial ^{190}Pt atoms N_0 is therefore:

$$N_0 = \frac{count\_Pt}{t} \cdot \frac{t_{1/2}}{ln2}. \tag{7.8}$$

The value of t is calculated for each crystal.
The corresponding number of moles of natural platinum is given by:

$$n = \frac{count\_Pt \cdot t_{1/2}}{t \cdot ln2 \cdot \eta \cdot N_A} \tag{7.9}$$

where η is the isotopic abundance of ^{190}Pt, which is 0.014%, and N_A is the Avogadro number.
The platinum heat capacity of selected CUORE-0 crystals is reported in table 7.3. The value of the ^{190}Pt counts in the energy interval of [3200−3400], the measurement live time value, the background counts, *count_bkg*, the effective counts produced by platinum contamination, *count_Pt*, the number of moles of natural platinum, n, are also reported in the table. The platinum

Ch	count	t [yr]	*count_bkg*	*count_Pt*	$n \times 10^{-8}$	C_{Pt} $\times 10^{-11}$ [J/K]
30	26 ± 5	0.92	2.2 ± 0.1	23.8 ± 5.1	28.8 ± 5.4	1.86 ± 0.25
31	29 ± 5	0.88	2.1 ± 0.1	26.9 ± 5.4	34.1 ± 5.5	2.20 ± 0.25
45	39 ± 6	0.94	2.3 ± 0.1	36.7 ± 6.3	43.1 ± 6.9	2.79 ± 0.32
28	41 ± 6	0.92	2.2 ± 0.1	38.8 ± 6.4	46.9 ± 6.8	3.04 ± 0.32
51	52 ± 7	0.92	2.2 ± 0.1	49.8 ± 7.2	60.2 ± 7.8	3.89 ± 0.36
41	60 ± 7	0.94	2.3 ± 0.1	57.7 ± 7.7	67.8 ± 8.7	4.39 ± 0.40
33	135 ± 11	0.94	2.3 ± 0.1	132.7 ± 11.6	155.9 ± 14.1	10.09 ± 0.63

Table 7.3: The value of the ^{190}Pt counts, the measured live time, the flat background counts, the number of moles of natural platinum and the calculated platinum capacity for each crystal.

heat capacity is of the order of 10^{-11} J/K, roughly two orders of magnitude below the TeO_2 crystal one, which is 2.3×10^{-9} J/K. In few cases, a platinum contamination (Ch33) produces a heat capacity of platinum that is just an order of magnitude below the TeO_2 one ($C_{Pt} \sim 10^{-10}$). It is evident that the platinum heat capacity is not negligible, so its contribution must be taken into account in the CUORE thermal model.

7.2.2 Platinum capacity effects

It is possible to suppose that each crystal has a different pulse shape because the platinum heat capacity (and possibly its conductance to the TeO_2) is different for each of them. This means that one time constant is related to the platinum heat capacity.
Indeed a strong correlation between the platinum heat capacity and the first decay time is observed (see fig. 7.10). At high platinum contamination the first decay time is faster.

The platinum heat capacity also influences the rise time, as shown in

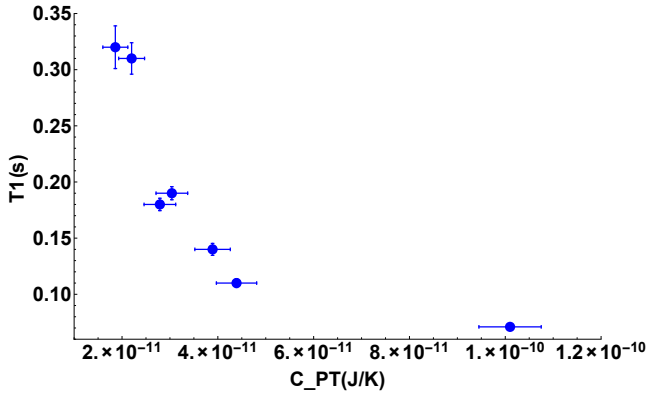

Figure 7.10: First decay time as function of platinum heat capacity.

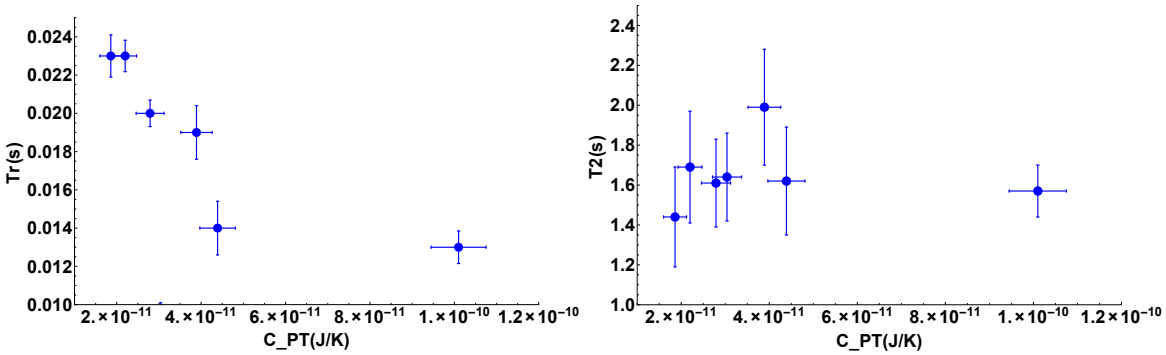

(a) (b)

Figure 7.11: Rise time (a) and the second decay time (b) as function of platinum heat capacity.

figure 7.11(a). On the contrary, the second decay time seems independent from the platinum heat capacity (see fig. 7.11(b)).

7.3 Fit parameters correlation

Different pulse shape observed for a given crystal represent another important aspect of the CUORE bolometer response. This aspect is proved by the wide time constants distribution, specially the long decay time (see fig. 7.12). This means that there is a possible relation between the time constants and some physical parameters or a possible relation between the fit parameters.

The different pulse shape could depend on the different energy released into the crystal (that can induce a different variation on the heat capacities or thermal conductances because of the different temperature increase) or could depend on a temperature drift of the detector. In figure 7.13 the three time constants as function of the pulse amplitude, i.e. the energy released in the crystal, are shown. In figure 7.14 the three time constants as function of the baseline value, i.e. the temperature, are shown. The example shown in figure 7.13 and 7.14 correspond to Ch31. The same result was obtained for all selected channels. The three time constants seem independent on the energy and on the temperature variation.

The wide time constants distribution could depend on the observed relation between the two decay times (see fig. 7.15). The origin of this relation is unclear, but explains the different pulse shape observed for a given crystal in the average pulse modeling (see fig.6.9 in section 6.5.1)

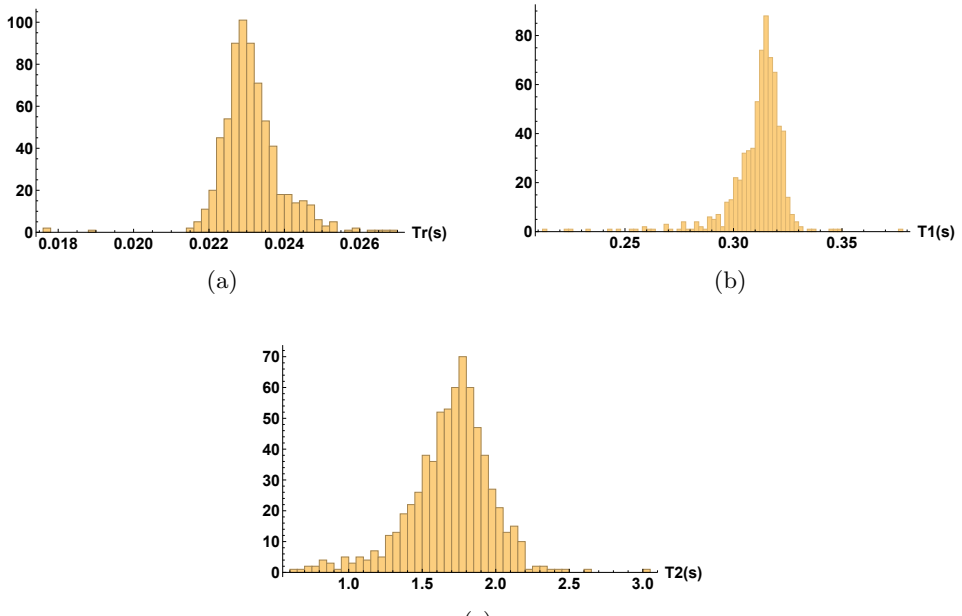

(a) (b) (c)

Figure 7.12: Time constant distribution for Ch31.

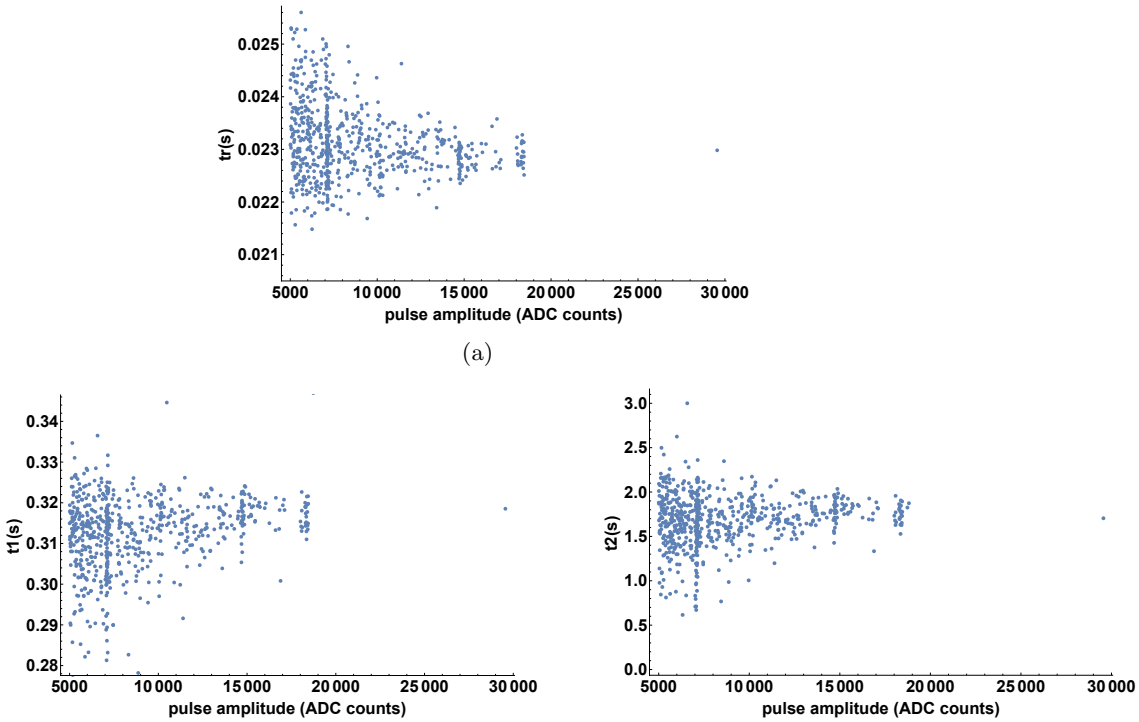

(a) (b) (c)

Figure 7.13: Time constants as function of pulse amplitude for channel 31.

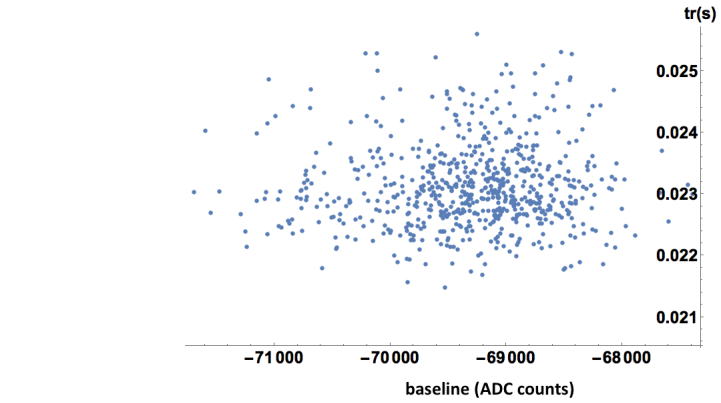

(a)

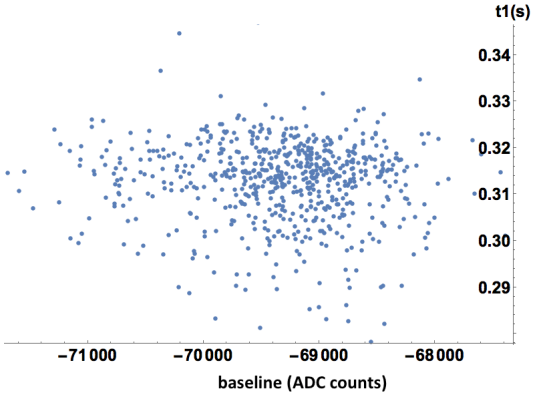

(b)

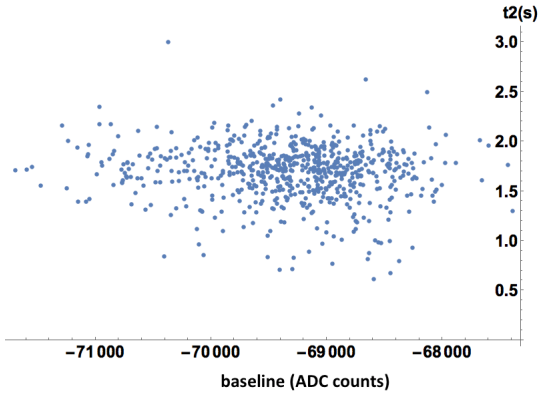

(c)

Figure 7.14: Time constants as function of baseline value for channel 31.

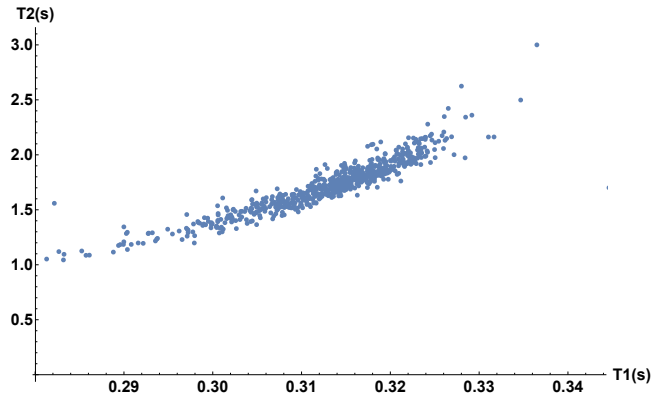

Figure 7.15: Relation between the two decay time constant for one channel.

7.3.1 Time constants relation

The relation between t_1 and t_2 was observed in all selected channel (see figure 7.16). The relation is different for each crystal and probably it is connected to the platinum capacitance. At low platinum contamination it has a quadratic law (Ch30/Ch31), while it is linear at high platinum contamination (Ch41/Ch33).

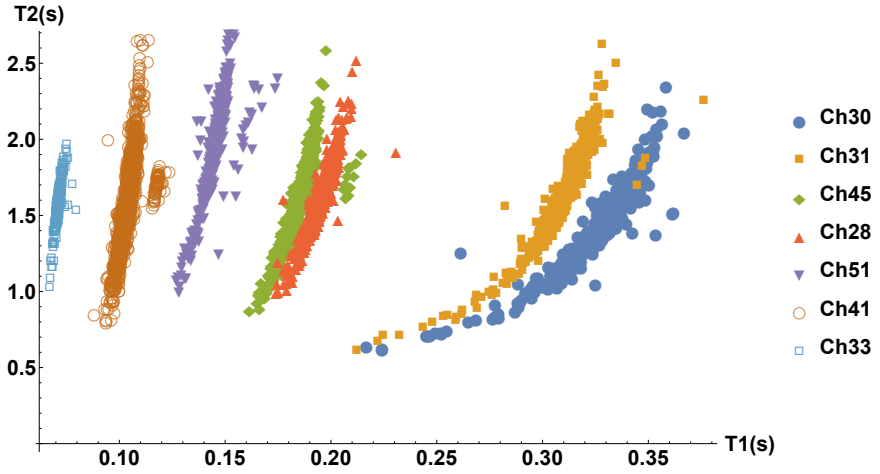

Figure 7.16: Relation between the two decay time t_1 and t_2.

On the contrary the two decay times are not strongly related to the rise time, as shown in figure 7.17.

The relation between the two decay times explains the difficulty to model

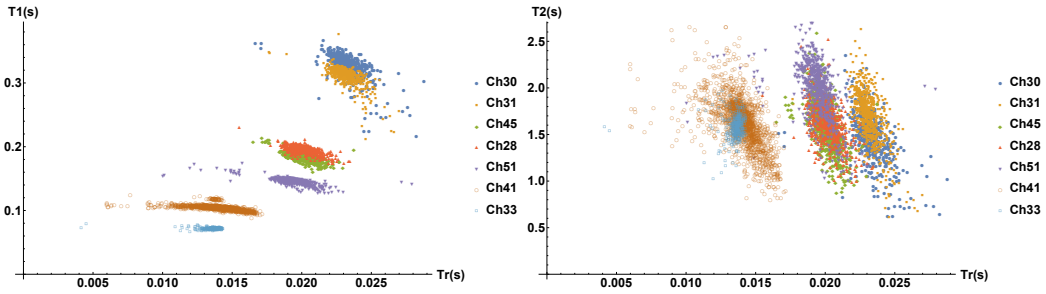

(a) (b)

Figure 7.17: Relation between the rise time and the two decays time.

the average pulse. Since t_1 and t_2 are related, fake time constant could be produced in the building process of average pulse. This could explain the four time constant found in the average pulse modeling.

7.3.2 Amplitudes relation

Another relation between the fit parameters is present between the two exponential amplitudes, A_1 and A_2 (see fig. 7.18). The two amplitudes follow the distribution of the pulse amplitude, i.e. the energy, because its definition in the fit function is given by:

$$A_1 + A_2 = A_r, \tag{7.10}$$

where A_r is the pulse amplitude: this implies a correlation between the two coefficients.
In figure 7.18 the A_2 vs A_1 distributions for all the seven channels are shown.

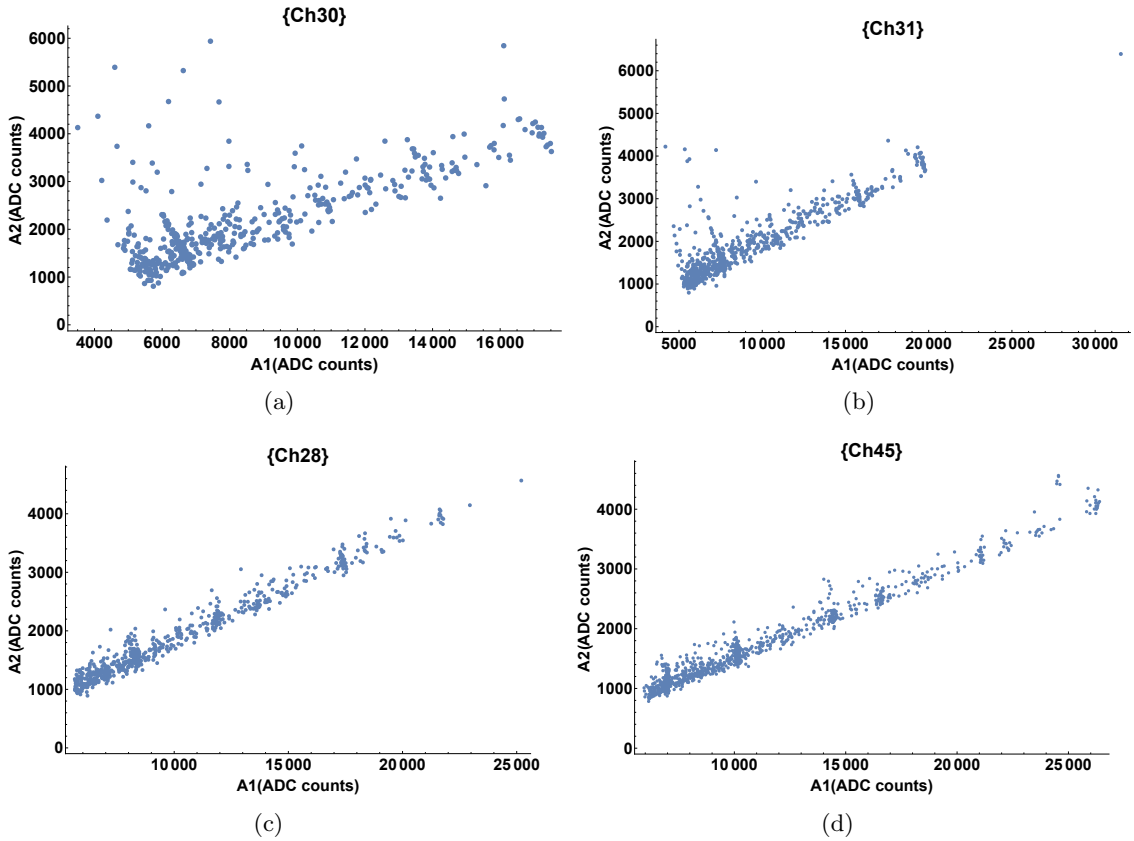

(a) (b)

(c) (d)

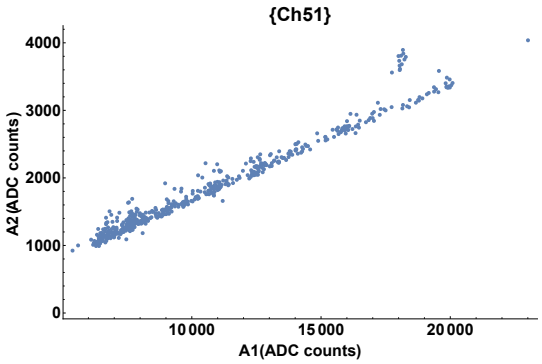

(e)

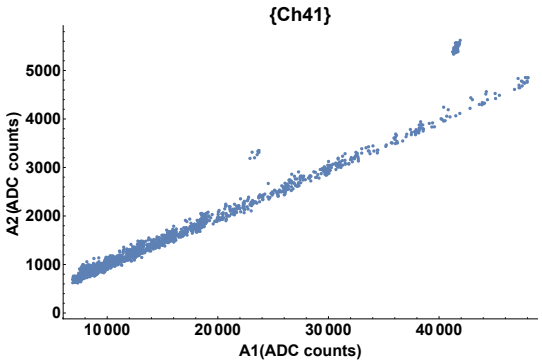

(f)

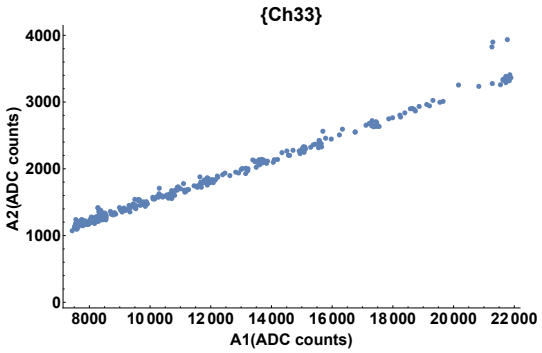

(g)

Figure 7.18: Correlation between t_1 vs t_2.

7.4 Results

The CUORE bolometer response was successfully described by the following fit function model:

$$F_{pulse} = A_1 exp\left[-\frac{t}{t_1}\right] + A_2 exp\left[-\frac{t}{t_2}\right] - (A_1 + A_2) exp\left[-\frac{t}{t_r}\right]. \quad (7.11)$$

The corresponding transfer function is described by the following equation (see section 6.3):

$$F(s) = \frac{(s - z_0)}{(s - p_2)(s - p_1)(s - p_r)}, \quad (7.12)$$

with $p_r < p_1 < z_0 < p_2$.
The poles p_1 and p_2 correspond to the two decay times (t_1 and t_2), respectively. Since they correspond to decay time constants, the transfer function has one zero and its value is in the middle of the values of two poles. The pole p_r corresponds to the rise time.
The response can be expressed in term of poles and zeros by the following equation:

$$\begin{aligned} f(t) = & \frac{p_1 - z_0}{(p_1 - p_2)(p_1 - p_r)} exp[p_1 t] + \frac{p_2 - z_0}{(p_2 - p_1)(p_2 - p_r)} exp[p_2 t] + \\ & \frac{p_r - z_0}{(p_r - p_1)(p_r - p_2)} exp[p_r t]. \end{aligned} \quad (7.13)$$

The three poles correspond to three independent and effective heat capacities, among the ones listed in section 6.2.
It was observed a strong correlation between platinum heat capacity and t_1, while t_2 is uniformly distribute for each channel. It reasonable to suppose that the decay time constants are generated by platinum and TeO_2 heat capacity.
The third thermal capacitance could be induced by another CUORE bolometer components, the most probable is the electrons thermal capacitance of the NTD sensor.

Conclusion

The main topic of this Ph.D. work has been the study of the response of the CUORE TeO_2 bolometers for a better comprehension of the detector and for a possible future improvement of the experimental sensitivity.
CUORE is a tonne-scale starting bolometric experiment that will search for $0\nu\beta\beta$ of ^{130}Te. CUORE-0, the most recent CUORE prototype and demonstrator, has been a test of TeO_2 bolometer performances. Beside proving some of the crucial goals for the CUORE sensitivity, such as resolution and background index, CUORE-0 provided a large amount of data that have been used in this work.
The first evidence arising from the CUORE-0 data is that there is a large spread in the bolometric response parameters (such as rise and decay time constants, pulse amplitude, etc.). This spread is not explained by the spread of dimensions or interface surfaces of the main detector components. Moreover a clear correlation between the variation of the different detector components (e.g. TeO_2 heat capacity) and the pulse shape parameters was never established. Over the years many different models have been developed to try to account for all these effects, but none of them has been able to reproduce the full dynamical behavior of the detectors. In addition, the large number of free parameters in these models makes very difficult to establish strict correlations with physical variables.
The idea of this work is to approach the problem from the opposite side, starting not from the model but from the fit of the pulses to establish correlations with physical variables and then use these results as hints to develop a model. The goal was to define a set of parameters that describe the pulse shape and then study possible correlations among the fit parameters and physical ones.
A bolometer response, described by the Laplace solution of a thermal circuit, is a sum of n exponentials, in which each time constant corresponds to an independent heat capacity in the circuit. As a first step I fitted the CUORE-0 pulses varying the number of exponentials, in order to find the minimum number of time constants that describe each pulse shape. A first evidence of this analysis has been that the electronic chain filtering of the pulse (Bessel filter and RC intrinsic filtering effect) can introduce extra time constants that could be erroneously interpreted as heat capacities in the

circuit. To avoid these effects I focused the analysis on a "ad hoc" subset of data in which the electronics effects were minimized. The pulse were acquired with a Bessel cutoff of 120 Hz (instead of the usual 12 Hz) and the NTD working point resistance was chosen to be low enough to neglect the RC filter effects ($10 < R < 25\ M\Omega$).
This study provided, for the first time, a fit function that describes the CUORE bolometer response and made possible to identify the dominant heat capacities. One of these heat capacities depends on the presence of platinum inside the TeO_2. The platinum contamination, coming from the crucible in which the TeO_2 crystals are grown, is not in the form of diffuse atoms but in small metallic pieces. The platinum heat capacity was measured by the rate of alpha decay of the isotope ^{190}Pt, for each crystal. The value of platinum heat capacity, $10^{-10} - 10^{-11}$ J/K at 10 mK, is competing with the expected dominant one from TeO_2. A strong correlation between the platinum heat capacity and the first decay constant of the pulses was observed: the first decay time is faster for high platinum contamination producing quite different pulse shapes for different crystals.
I was then able to describe the CUORE bolometer response as a sum of three exponentials, one rise plus two decay time constants. The two decay time constants are generated by platinum heat capacity (as is visible by the correlation between platinum abundance and t_1) and by the TeO_2 heat capacity (corresponding to the fact that t_2 is almost crystal independent). The rise time is not yet clearly correlated but could be generated by the electron heat capacity of the NTD.
These results open the way for the first time to a full thermal model of the TeO_2 bolometers, which are currently a leading technology in $0\nu\beta\beta$ search. Moreover the observed spreads on some fitting parameters may results in an optimization of the detector resolution via the improved fitting tools.
Many deeper studies should start from these results. A next step can be the identification of the origin of the spread in the pulse shape parameters, testing possible effects of the fit. A second relevant study will be a clearer identification of the rise time correlation with a specific physics parameter. The last step will be the development of a full CUORE thermal model. Further improvements will come from the analysis of the much larger amount of data coming from the starting CUORE experiment.

Bibliography

[1] J. Chadwick, *Possible existence of Neutron.* Nature, 1932

[2] E. Fermi, *Tentativo di una teoria dell' emissione dei raggi beta.* Ricerca Scientifica, 1933

[3] F. Reins, G. Cowan, *The neutrino.* Nature, 1946

[4] M.Goldhaber, L.Grodzins, W.Sunyar, *Helicity of Neutrinos.* Physical Letter Review, 1957

[5] LEP COLLABORATION, *Precision electroweak measurements on the Z resonce.* Physics Reports, 2006

[6] M.Schwartz, L.M.Lederman, *Observation of high-energy neutrino reactions and the existence of two kinds of neutrinos.* Physical Letter Review, 1957

[7] K.Kodoma *et.al*, *Observation of tau neutrino interaction.* Physical Review, 2001

[8] B.T. Clevalend *et al.*, *Measurement of the solar electron neutrino flux with the Homestake chlorine detector.* Astrophysics Journal, 1998

[9] G.Shaw, F.Mandl, *Quantum field theory.* Wiley, 1984

[10] B. Pontecorvo, V. Gribov, *Neutrino astronomy and the lepton charge.* Physical Letter Review, 1969

[11] C.Giunti, C.W.Kim, *Fundamentals of neutrino physics and astrophysics.* Oxford University, 2007

[12] J.L. Hewett *et al.*, *Fundamental Physics at the Intensity Frontier.* arXiv:1205.2671

[13] E. Majorana, *Teoria simmetrica dell'elettrone e del positrone.* Il Nuovo Cimento, 1937

[14] Q. Ahmad *et al.*, *Direct evidence for neutrino flavor transformation from neutral current interactions in the Sudbury Neutrino Observatory.* Physical Letter Review, Vol.89, 2002

[15] S.Abe *et al.*, *Precision Measurement of Neutrino Oscillation Parameters with KamLAND.* Physical Letter Review, Vol.100, 2008

[16] Alain Bellerive, *New Results on Solar Neutrinos*, PoS ICHEP2010 (2010) 529

[17] J. Hosaka *et al.*, *Three flavor neutrino oscillation analysis of atmospheric neutrinos in Super-KAMIOKANDE.* Physical Review, 2006

[18] K. Abe *et al.*, *Observation of electron neutrino appearance in a muon neutrino beam.* Phys.Rew.Lett. 112,061802, 2014

[19] Louise Suter *et al.*, *Extrapolation technique and systematic uncertainties in the NOνA muon neutrino disappearance analysis.* arXiv:1512.03371

[20] David M. Webber*et al.*, *An improved measurement of electron antineutrino disappearance at DAYA BAY.* Nuclear Physics B Proceedings Supplement 00 (2012)

[21] F. Capozzi *et al.*, *Neutrino masses and mixings: Status of know and unknown 3ν parameters.* Nuclear Physic B 00,2016

[22] G. Drexlin *et al.*, *Current Direct Neutrino Mass Experiments.* Advances in High Energy Physics, 2013

[23] V. N. Aseev *et al.*, *Upper limit on the electron antineutrino mass from the Troitsk experiment.* Physical Review D 84, 2011

[24] Ch. Kraus *et al.*, *Final result from phase II of the Mainz neutrino mass search in tritium β decay.* The European Physical Journal C, 2005

[25] KATRIN Collaboration, KATRIN Report 2004

[26] P.J.Doe *et al.*, *Project 8: Determining neutrino mass from tritium beta decay using a frequency-based method.* arXiv:1309.7093

[27] L.Gastaldo *et al.*, *Characterization of low temperature metallic magnetic calorimeters having gold absorbers with implanted ^{163}Ho ions.* Nucl. Inst. Meth. A, 711, 150-159 (2013)

[28] B.Alpert *et al.*, *HOLMES - The Electron Capture Decay of ^{163}Ho to Measure the Electron Neutrino Mass with sub-eV sensitivity.* Eur. Phys. J. C (2015) 75:112

[29] M. Croce *et al.*, *Development of holmium-163 electron-capture spectroscopy with transition-edge sensors.* arXiv:1510.03874

[30] S. Eliseev *et al.*, *Direct Measurement of the Mass Difference of* ^{163}*Ho and* ^{163}*Dy Solves the Q-Value Puzzle for the Neutrino Mass Determination.* Phys. Rev. Lett. 115, 062501 (2015)

[31] Loredana Gastaldo, Presentation at NOW 2016

[32] J. Lesgourgues *et al.*, *Neutrino cosmology and PLANK.* arXiv:1404.1740

[33] A. Melchiorri, *Neutrino Cosmology.* Presentation at "The universe of neutrino" (SSI2015)

[34] Dell'Oro *et al.*, *The contribution of light Majorana neutrinos to neutrinoless double beta decay and cosmology.* Journal of Cosmology and Astroparticle Physics (2015)

[35] PLANK Collaboration, *PLANK 2015 results. XIII. Cosmological parameters.* arXiv:1502.01589v2

[36] S.Elliot *et al.*, *Direct evidence for two-neutrino double beta decay in* ^{82}*Se.* Phys. Rev. Lett.59,2020 (1987)

[37] A.S. Barabash, *Double beta decay experiment: present status and prospects for the future.* Fundamental Research in Particle Physic and Cosmophysic, Vol.74,2015

[38] I.Avignone, Frank T., S.R. Elliot and J.Engel, *Double beta decay, Majorana neutrinos and neutrino mass.* Rev. Mod. Phys, vol.80, 2008

[39] R.Saakyan, *Two neutrino double beta decay.* Ann.Rev.Nucl.Part.Sci (2013)

[40] H.V.Klapdor-Kleingrothaus *et.al.*, Modern Physic Letter A 16, p.2049 (2001)

[41] A. Gando *et al.*, *Measurement of the double-β decay half-life of* ^{136}*Xe with the KamLAND-Zen experiment.* Phys. Rev. C 85, 045504 (2012)

[42] T. Bernatowicz *et al.*, *Precise determination of relative and absolute $\beta\beta$-decay rate of* ^{128}*Te and* ^{130}*Te.* Phys. Rev.C 47:806 (1993)

[43] A.L. Turkevich, Phys.Rev. Lett. 67:3211 (1991)

[44] I.Ogawa *et al.*, *Search for neutrino-less double beta decay of* ^{48}*Ca by* CaF_2 *scintillator.* Nuclear Physic A, Vol.730 (2004)

[45] M. Agostini *et al.*, *Results on neutrinoless double-β decay of* ^{76}*Ge from Phase-I of the GERDA Experiment.* Phys.Rev.Lett. 111, 1225503 (2013)

[46] R.Arnold *et al.*, *First results of the search for neutrinoless double beta decay with the NEMO-3 detector.* Phys.Rev.Lett. 95, 182302 (2005)

[47] R.Arnold *et al.*, *Search for neutrinoless double-beta decay of* ^{100}*Mo with the NEMO-3 detector.* Phys.Rev.D, 89, 11101 (2014)

[48] K.Alfonso *et al.*, *Search of neutrinoless double-beta decay of* ^{130}*Te with CUORE-0.* Phys.Rev.Lett.115, 102502 (2015)

[49] J. Albert *et al.*, *Search for Majorana neutrinos with the first two years of EX0-200 data.* Nature 510, 229-234 (2014)

[50] J. Argyriades *et al.*, *Measurement of the double-β decay half-life of* ^{150}*Nd and search for neutrinoless decay modes with the NEMO-3 detector.* Phys.Rev.C 80, 032501 (2009)

[51] S. Dell'Oro, S. Marcocci, V. Vissani, *New expectations and uncertainties on neutrinoless double beta decay.* Phys. Rev. D 90, 033005 (2014)

[52] J.Kotila, F. Iachello, *Phase space factors for double-β decay.* Phys.Rev.C85, 034316 (2012)

[53] J. Menendez, A. Poves, E. Caurier, F. Nowacki, *Disassembling the nuclear matrix elements of the neutrinoless double beta decay.* Nucl.Phys.A 818, 139-151 (2009)

[54] E. Caurier, G. Martinez-Pinedo, F. Nowacki, A.Poves, A.P.Zuker, *The shell model as unified view of nuclear structure.* Rev.Mod.Phys. 77, 427-488 (2005)

[55] F.Simkovic, V.Rodin, A.Faessler, P.Vogel, *$0\nu\beta\beta$ and $2\nu\beta\beta$ nuclear matrix elements, quasiparticle random-phase approximation, and isospin symmetry restoration.* Phys. Rev. C 87, 045501 (2013)

[56] J. Hyvarinen, J. Suhonen, *Nuclear matrix elements for $0\nu\beta\beta$ decays with light or heavy Majorana-neutrino exchange.* Phys.Rev.C 88, 024613 (2015)

[57] J. Barea, J. Kotila, F. Iachello, *$0\nu\beta\beta$ and $2\nu\beta\beta$ nuclear matrix elements in the interacting boson model with isospin restoration.* Phys.Rev.C 91, 034304 (2015)

[58] Planck Collaboration *Planck 2013 results.* arXiv:1303.5057

[59] A.D. Sakharov, *Violation of CP invariance,C asymmetry, and Baryon asymmetry of the universe.* Pisma Zh. Eksp. Teor. Fiz (1967)

[60] C.S.Fonga, E.Nardi, A. Riotto, *Leptogenis in the Universe* arXiv:1301.3062

[61] F.T.Avignone *et al.*, *Double beta decay, Majorana neutrino, and neutrino mass.* Rev.Mod.Phys., vol.80, pp.481-516 (2008)

[62] F.T.Avignone *et al.*, *Next generation double-beta decay experiments: metrics for their evaluation.* New J. Phys, vol.7 (2005)

[63] G.Douysset *et. al.*, *Determination of the ^{76}Ge double beta decay Q value.* Phys. Rev. Lett. 86, 4259 (2001)

[64] N. D. Scielzo *et al.*, *Double beta decay Q value of ^{130}Te, ^{128}Te and ^{120}Te.* arXiv:0902.2376

[65] M. Redshaw, E. Wingfield, J. McDaniel, E.G. Myers, *Mass and double beta decay Q-value of Xe-136.* Phys.Rev.Lett. 98,053003 (2007)

[66] Canberra Semiconductor, NV, Lammerdries 25, B-2250, Olen, Belgium.

[67] GERDA Collaboration, *Production, characterization and operation of ^{76}Ge enriched BEGe detectors in GERDA.* Eur. Phys. J. C (2015)

[68] M. Agostini, *First results from GERDA phase-II.* Presentation at Neutrino 2016

[69] A. Gando *et al.*, *Search for Majorana Neutrinos near the Inverted Mass Hierarchy Region with KamLAND-Zen.* arXiv:1605:02889

[70] EX0-Collaboration, *Search for Majorana neutrinos with the first two years of EXO-200 data.* Nature (2014)

[71] S. dell'Oro, *Review on theoretical and experimental prospects on Neutrinoless Double Beta Decay.* Presentation at NuFact 2016

[72] G. Benato, *Effective Majorana mass and neutrinoless double beta decay.* Eur.Phys.J.C. (2015)

[73] N. Abgrall *et al.*, *The Majorana Demonstrator Radioassay Program.* arXiv:1601.03779

[74] Liang Yang, *Status and Prospects for the EXO-200 and nEXO Experiments.* Presentation at Neutrino 2016

[75] J. Cadenas *et al.*, *Present Status and Future Perspectives of the NEXT Experiment.* Advances in High Energy Physics (2014)

[76] S. Andringa *et.al.*, *Current Status and Future Prospects of the SNO+ Experiment.* Advances in High Energy Physics (2016)

[77] R. Brugnera and A. Garfagnini, *Status of the GERDA Experiment at the Laboratori Nazionali del Gran Sasso.* Adv. High En. Phys. 2013, 506186 (2013)

[78] S. Elliott, Presentation at Neutrino 2016

[79] L. Pattavina, Presentation at TAUP 2015

[80] R. Arnold *et al.*, *Results of the search for neutrinoless double-β decay in Mo-100 with the NEMO-3 experiment.* Phys. Rev. D 92, 072011 (2015)

[81] V. Alenkov *et al.*, *Technical Design Report for the AMoRE $0\nu\beta\beta$ Decay Search Experiment.* arXiv:1512.05957

[82] D. R. Artusa *et al.*, *Searching for Neutrinoless Double-Beta Decay of ^{130}Te with CUORE.* Advances in High Energy Physics (2015)

[83] A. Wright, Presentation at Neutrino 2016

[84] C. Licciardi, Presentation at Neutrino 2016

[85] NEXT-Collaboration, *Sensitivity of NEXT-100 to neutrinoless double beta decay.* Journal of High Energy Physics (2016)

[86] A. Wright, Presentation at Neutrino 2016

[87] S.Simon, *Application of low temperature calorimeter to radioactive measurements.* Nature 135, 763 (1935)

[88] D. H. Andrews *et al.*, Physics Review Letters 513A, 82 (1999)

[89] E.Fiorini and T. O. Niinikoski, Nucl. Instr. Meth. A224, 83 (1984).

[90] C. Arnaldoldi *et al.*, *CUORE: a Cryogenic Underground Observatory for Rare Events.* Nucl.Instr.Meth., 2004.

[91] J. Barea, J. Kotila, F. Iachello, *$0\nu\beta\beta$ and $2\nu\beta\beta$ nuclear matrix elements in the interaction boson with isospin restoration.* Phys. Rev. C 91, 034304 (2015).

[92] A. Nucciotti, *Design of the Cryogenic-Free Cryogenic System for the CUORE experiment.* J. Low Temp. Phys(2008) 151: 662−668

[93] *http : //www.minusk.com*

[94] L. Canonica, *The road to CUORE experiment: research and development for an extremely low background bolometer array.* Ph.D. thesis

[95] J.S. Cushman *et al.*, *The detector calibration system for the CUORE cryogenic bolometer array.* Nuclear Instruments and Methods A 844, 32-44 (2017)

[96] V. Singh *et al.*, *The CUORE cryostat: commissioning and performance.* Journal of Physics: Conference Series 718 (2016) 062054

[97] CUORE collaboration, *CUORE-0 detector: design, construction and operation.* JINST 11 (2016) no.07, P07009

[98] E. Andreotti *et al.*, ^{130}*Te neutrinoless double beta decay with CUORICINO.* nucl-ex/1012.3266v1, 2010.

[99] CUORE Collaboration, *The projected background for the CUORE experiment.* arXiv:1704.08970

[100] CUORE Collaboration, *Search for neutrinoless double beta decay of* ^{130}*Te with CUORE-0.* Phys.Rev.Lett.115 no.10, 102502 (2015)

[101] IBM-2 Phys. Rev. C 91, 034304 (2015)

[102] QRPA-TU Phys. Rev. C 87, 045501 (2013)

[103] QRPA Phys. Rev. C 91, 024613 (2015)

[104] ISM Nucl. Phys. A 818, 139 (2009)

[105] EDF Phys. Rev. Lett. 105, 252503 (2010)

[106] CUORE collabaration, *Searching for neutrinoless double beta decay of* ^{130}*Te with CUORE.* Phys. Rev. Lett. 115, 102502 (2015)

[107] K. Petzl, *Cryogenic calorimeters in astro and particle physics.* Nuclear Instruments and Mhetods in Physics Reserch, 2000.

[108] Y. B. Levinson, *Phonon propagation with frequency down-conversion, in Nonequilibrium Phonons in Nonmettalic Crystals.* edited by W. Eisenmenger and A. Kaplyanskii, chap. 3, pp. 91−143, Elsevier Science Publisher B.V., Amsterdam, 1986

[109] Gerald Burns, *Solide State Physic.*, chap 11−12, Accademic Press, 1985

[110] *Superconducting multiplexer for array of transition edge sensor.* Appl. Phys. Lett. 74, 4043 (1999)

[111] D.Mc Common *Semiconductor thermistors.* arXiv.org/0503086,2005.

[112] N.F.Mott, J.H.Davies, *Metal insulator transition in doped semiconductors.* Phylosophical Magazine B, 1980.

[113] A. Miller and E. Abrahams, *Impurity Conduction at Low Concentrations.* Physical Review, vol. 120, pp. 745−755, Nov. 1960.

[114] N.F.Mott *Conduction in non-crystalline materials.* Philosophical Magazine, Volume 39, 1969

[115] A L Efros, Nguyen Van Lien and B I Shklovskii, *Impurity band structure in lightly doped semiconductors.* Journal of Physics C: Solid State Physics, Volume 12, Number 10, 1975

[116] M. Baracci *et al.*, *Measurement of low temperature specific heat of cristalline TeO_2 for the optimitation of bolometric detector.* Journal of Low Temperature Physics.

[117] C. Arnaboldi *et al.*, *Production of high purity TeO_2 single crystals for the study of neutrinoless double beta decay.* J. Cryst. Growth 312 (2010), no. 20 2999.

[118] F. Alessandria*et al.*, *CUORE crystal validation run: results on radioactive contamination and extrapolation to CUORE background.* Astropart. Phys. 35 (2012) 839

[119] CUORE collaboration, *Analysis techniques for the evaluation of the neutrinoless double$-\beta$ decay lifetime in ^{130}Te with the CUORE-0 detector.* Phys. Rev. C93 (2015), no. 4045503

[120] F. Alessandria *et al.*, *Validation of techniques to mitigate copper surface contamination in CUORE.* Astropart. Phys. 45 (2013) 13.

[121] M. Pedretti, *Measurement of thermal properties for modeling and optimization of large mass bolometers.* Physca B. 329 (2003) 1614

[122] M. Pedretti, *The single module for CUORICINO and CUORE detectors: test, construction and modelling..* Ph.D. thesis

[123] G. Audi, O. Bersillon, J. Blachot, A.H. Wapstra, *The NUBASE evaluation of nuclear and decay properties.* Nucl. Phys. A, 729 (2003).

[124] Douglas L. Martin, *Specific heat of platinum below 30 K.* Phys. Rev. B 17, 1670.